Quantum Dynamics of Strongly-Interacting Bosons in Optical Lattices with Disorder

Mi Yan

Dissertation submitted to the Faculty of the
Virginia Polytechnic Institute and State University
in partial fulfillment of the requirements for the degree of

Doctor of Philosophy
in
Physics

Vito W. Scarola, Chair
Eric Sharpe
Jean Heremans
Kyungwha Park

November 29, 2018
Blacksburg, Virginia

Keywords: Quantum dynamics, Optical lattices, Bose-Hubbard model, Disordered system.

Quantum Dynamics of Strongly-Interacting Bosons in Optical Lattices with Disorder

Mi Yan

(ABSTRACT)

Ultracold atoms in optical lattices offer an important tool for studying dynamics in many-body interacting systems in a pristine environment. This thesis focuses on three theoretical works motivated by recent optical lattice experiments. In the first, we theoretically study the center of mass dynamics of states derived from the disordered Bose-Hubbard model in a trapping potential. We find that the edge states in the trap allow center of mass motion even with insulating states in the center. We identify short and long-time mechanisms for edge state transport in insulating phases. We also argue that the center of mass velocity can aid in identifying a Bose-glass phase. Our zero temperature results offer important insights into mechanisms of transport of atoms in trapped optical lattices while putting bounds on center of mass dynamics expected at non-zero temperature.

In the second work, we study the domain wall expansion dynamics of strongly interacting bosons in 2D optical lattices with disorder in a recent experiment [J.-y. Choi et al., Science **352**, 1547 (2016)]. We show that Gutzwiller mean-field theory (GMFT) captures the main experimental observations, which are a result of the competition between disorder and interactions. Our findings highlight the difficulty in distinguishing glassy dynamics, which can be captured by GMFT, and many-body localization, which cannot be captured by GMFT, and indicate the need for further experimental studies of this system.

The last work features our study of phase diagrams of the 2D Bose-Hubbard model in an optical lattice with synthetic spin-orbit coupling. We investigate the transitions between superfluids with different phase patterns, which may be detected by measuring the spin-dependent momentum distribution.

Quantum Dynamics of Strongly-Interacting Bosons in Optical Lattices with Disorder

Mi Yan

(GENERAL AUDIENCE ABSTRACT)

Ultracold atoms in optical lattices, a periodic potential generated by laser beams, offer an important tool for quantum simulations in a pristine environment. Motivated by recent optical lattice experiments with the implementation of disorder and synthetic spin-orbit coupling, we utilize Gutzwiller mean-field theory (GMFT) to study the dynamics of disordered state in an optical lattice under the sudden shift of the harmonic trap, the domain wall expansion of strongly interacting bosons in 2D lattices with disorder, and spin-orbit-driven transitions in the Bose-Hubbard model. We argue that the center of mass velocity can aid in identifying a Bose-glass phase. Our findings show that evidence for many-body localization claimed in experiments [J.-y. Choi et al., Science **352**, 1547 (2016)] must lie in the differences between GMFT and experiments. We also find that strong spin-orbit coupling alone can generate superfluids with finite momentum and staggered phase patterns.

Dedication

To my Mother.

Acknowledgments

Professor Vito Scarola is an outstanding advisor. I am extremely grateful for his support and guidance of my research, without which this work would have never been possible. I am constantly inspired by his enthusiasm for physics and his breadth of interests. Vito has provided valuable advice. I will always remember his patience in teaching me to how to debug my code, derive equations and improve communication skills when I first came to the group.

I have benefited a lot from collaboration with many brilliant researchers including Dr. Hoi-Yin Hui who is the former postdoctoral associate in our research group, Professor Marcos Rigol from The Pennsylvania State University and Professor Chuanwei Zhang form University of Texas at Dallas. I would like to express my gratitude for their patience and kindness.

I have enjoyed discussion with and courses offered by other faculty members in physics department at Virginia Tech, including but not limited to Professor Eric Sharpe, Professor Jean Heremans, Professor Kyungwha Park and Professor Uwe Tauber. I would also like to thank my graduate committee. The time and effort they spent into commenting on my prelim and predefense has greatly improved the quality of this thesis.

I am fortunate to work with incredible people from our research group like Dr. Fei Lin, Mengsu Chen and Peter Raum. The stimulating discussions with them had greatly broadened my horizons. It has also been a great pleasure to study with other graduate students including Yanfei Tang, Xiangwen Wang, Chengyuan Wen, Hadi Parsian, Junkai Zeng and

Juntao Wang. I would like to particularly thank Yanxi Li for discussions regarding condensed matter experiments and helpful advice in life. I owe much to George Barron for teaching me so many fancy techniques in Mathematica.

I am indebted to many wonderful friends I met in New River Valley during my PhD study including Josh Coble, Stephen Duraiswamy, Nate Bullard, Jamey Tucker and Doug Short who have always encouraged me to persevere when trials and difficulties are strong.

I want to acknowledge generous support from Virginia Tech, AFOSR, ARO, and DARPA.

Finally, I would like to express my heartfelt thanks to my beloved family for all the love through the years.

Contents

List of Figures xi

List of Tables xiv

1 Introduction 1

1.1 Motivation 1

1.2 Outline 3

1.3 Publication List 5

2 Ultracold Atoms in Optical Lattices 6

2.1 Optical Lattices 6

2.2 Non-interacting Particles in An Optical Lattice 9

2.3 Adding Onsite Interactions: The Bose-Hubbard Hamiltonian 12

3 Bose-Hubbard Models 16

3.1 Superfluid to Mott Insulator Phase Transition 16

3.2 Gutzwiller Mean-Field Theory 20

3.2.1 Static Gutzwiller method 20

3.2.2 Time-Dependent Gutzwiller method 22

3.2.3 Finite-Temperature Gutzwiller method 24

3.3 Disordered Bose-Hubbard Model 25

3.3.1 Disordered Optical Lattice 25

3.3.2 Bose Glass Phase 26

3.3.3 Dynamics of Disordered Optical Lattices 28

3.4 Spin-Orbit Coupled Bose-Hubbard Model 31

4 Dynamics of Disordered States in Bose-Hubbard Model with Harmonic Confinement 35

4.1 Introduction 35

4.2 Model 38

4.3 Static Properties 44

4.4 Center of Mass Dynamics 45

4.4.1 Superfluid Dynamics 45

4.4.2 Short-Time Insulator Dynamics 46

4.4.3 Long-Time Insulator Dynamics 49

4.5 Two-site Tunneling Time 51

4.6 Summary 52

5 Equilibration Dynamics of Strongly Interacting Bosons in 2D Lattices with Disorder 57

5.1 Introduction . . . 57
5.2 Model . . . 60
5.3 Methods . . . 60
5.4 Quenched Dynamics . . . 62
5.5 Phenomenological Parameter . . . 66
5.6 Checkerboard Case . . . 69
5.7 Non-quenched Dynamics for Uniformly Distributed Disorder . . . 69
5.8 Summary . . . 72

6 Phase Transitions of Spin-Orbit Coupled Bose-Hubbard Model in Optical Lattices 73

6.1 Introduction . . . 74
6.2 Model and Methods . . . 77
6.3 Quantum Phases in Finite Lattices with Periodic Boundaries . . . 82
6.4 Quantum Phases in a Trapping Potential . . . 86
6.5 Quantum Phases in Infinite Lattices . . . 88
6.6 Summary . . . 90

7 Conclusions and Outlook 91

Bibliography 94

List of Figures

2.1 Schematic illustration of 1D optical lattice 7

2.2 Schematic illustration of 2D and 3D optical lattices 8

2.3 Band structures for a 1D optical lattice in the first Brillouin zone. 11

2.4 Wannier functions at the central site in a 1D optical lattice plotted together with a schematic lattice potential for two different lattice depths. 11

2.5 Schematic illustration of parameters in the Bose-Hubbard model 13

2.6 Hubbard parameters as a function of lattice depth 14

3.1 Schematic of the density distribution in a lattice for superfluid and Mott insulator. 17

3.2 Level crossings between states with different densities for Mott insulator . . 18

3.3 Experimental demonstration of the SF-MI transition 19

3.4 Zero-temperature mean-field phase diagram of the uniform Bose-Hubbard model 22

3.5 Schematic illustration of the finite-temperature phase diagram of Bose-Hubbard model 23

3.6 Illustration of laser configuration producing a disordered optical lattice . . . 26

3.7 Distribution of Hubbard parameters in a disordered lattice 27

3.8 Schematic phase diagram of the disordered Bose-Hubbard model 28

3.9 Illustration of quantum phases for different disorder strength 29

3.10 Experiments of center-of-mass dynamics in a disordered lattice 30

3.11 Experiments of domain wall expansion dynamics in a 2D lattice with disorder 31

3.12 Schematic illustration of spin-orbit coupling in ultracold atoms 32

3.13 Experimental demonstration of Laser coupling schemes 33

4.1 Schematic showing two distinct mechanisms for center of mass dynamics after an initial shift of the trapping potential to the left 37

4.2 Schematic mean field phase diagram of the disordered Bose-Hubbard model 40

4.3 The disorder averaged correlation fucntion of for the initial states 41

4.4 The disorder averaged center of mass position along the x-direction plotted as function of time for various interaction strengths 42

4.5 The disorder averaged local density deviation from the initial state 43

4.6 The disorder averaged local density deviation from the initial state and local current flow 46

4.7 The disordered averaged center of mass velocity at short times 47

4.8 The disorder averaged center of mass position plotted as a function of time . 54

4.9 The disorder averaged center of mass velocity at long times as a function of interaction strength 55

4.10 Schematic two-site tunneling model 55

4.11 The comparison of the center of mass velocity at long times between the estimate of the two-site model and numerical simulations for various interaction strength 56

5.1 The site occupations for quenched dynamics at zero temperature 63

5.2 Time evolution of the imbalance compared with experiments 64

5.3 Normalized imbalance with the right half of the trap being initialized to a checkerboard pattern 67

5.4 Time evolution of the imbalance for various uniformly distributed disorder strengths with zero and finite temperature 70

6.1 Comparison of SOC strengths in solids and cold atoms 75

6.2 Schematic of spin independent tunneling and spin-dependent tunneling induced by SOC 78

6.3 Phase diagrams of SOC Bose-Hubbard model obtained from Gutzwiller simulations 80

6.4 The order parameters as a function of the hopping amplitude 83

6.5 Spin-dependent momentum distribution 84

6.6 Correlation functions of finite momentum superfluids on a 32×32 lattice with a confining potential 87

6.7 The kinetic energy as a function of the hopping amplitude 89

List of Tables

3.1 List of phases and related order parameters: superfluid stiffness ρ_s and compressibility κ. 27

List of Abbreviations

BEC Bose-Einstein condensation

BG Bose glass

COM Center-of-mass

FFLO Fulde-Ferrell-Larkin-Ovchinnikov

GMFT Gtuzwiller mean-field theory

MBL Many-body localization

MI Mott insulator

SF Superfluid

SOC Spin-orbit coupling

TOF Time-of-flight

Chapter 1

Introduction

1.1 Motivation

Quantum degenerate atomic gases have provided an ideal platform for simulating many-body interacting systems in condensed matter physics. The precise controllability and wide tunability of parameters in ultracold quantum gases allow us to engineer a wide range of effective Hamiltonians to explore. Different from condensed matter materials, the Hamiltonian describing cold atomic gas systems can be known to very high accuracy. The flexibility of changing parameters in the Hamiltonian such as the hopping amplitude, the interaction energy and disorder strength offers a valuable tool to study non-equilibrium dynamics in ultracold atomic systems.

Bose-Einstein condensation (BEC), a macroscopic quantum behavior, was first realized in experiments in the Cornell group [1] and Ketterle group [2] independently in 1995. In the first BEC experiments, weakly-interacting atoms in a harmonic trap were cooled to μK temperatures. Alongside uses in quantum simulations, cold atoms with macroscopic quantum behavior have been employed for timekeeping in atomic clocks [3, 4] and precision measurements of fundamental parameters [5].

Ultracold atoms loaded into an optical lattice, a periodic potential generated by interfering laser beams, open a new realm of possibility to study strongly correlated systems. In 2002,

the experiments [6] of Geriner et al., showed that cold atoms in a simple cubic optical lattice can exhibit the superfluid to Mott insulator phase transition predicted in the Bose-Hubbard model [7, 8]. After the observation of this phase transition, the development of new techniques for engineering atoms such as Feshbach resonances [9] for controlling the inter-atomic interaction strength, adding artificial gauge fields [10] and long-range interactions [11–13], Bragg spectroscopy [14, 15] and noise spectroscopy [16–18] stimulated a wide range of interest in using cold atoms to study novel quantum phases such as the fractional quantum Hall effect [19, 20], supersolids [21, 22] and even remarkable phenomena without counterpart elsewhere in condensed matter physics.

Recent experimental progress demonstrates that disorder can be implemented in optical lattices [23–41] to further probe phase transitions to glassy states induced by the competition between interactions and strong disorder. The experimental study of center of mass transport in a disordered lattice in Ref. [37] argued that the suppression of center of mass velocity in strong disorder indicated the presence of a Bose-glass predicted by the disordered Bose-Hubbard model [7].

Adding disorder in optical lattices also allows us to study localizaiton [42, 43]. In the non-interacting limit, fermionic band insulators [44] can lead to Anderson localizaiton [29, 30, 45–48] in the presence of disorder. The interplay of disorder and interaction in a bosonic system can lead to a Bose glass phase [7]. At high energy densities above the ground state, the interplay between disorder and inter-atomic interactions can generate a remarkable new phenomenon called many-body localization [49–51], in which eigenstate thermalization [52–54] is broken [55]. In the experiments of Ref. [56], it was argued that the density imbalance appearing to saturate to a nonzero value indicated the presence of many-body localization [49–51].

More recently, synthetic spin-orbit coupling with ultracold atomic gases has been realized

[57–63]. These experiments demonstrate that two-photon Raman processes can be used to engineer cold atoms with spin and momentum entangled eigenstates. Spin-orbit coupling in cold atoms [64, 65] is tunable by laser beams to extremes that are not possible in solids. Synthetic spin-orbit coupling opens the possibility to study non-trivial quantum phases, such as flat bands [66–69], exotic superfluidity [70, 71], and intriguing vortex structures [65, 72–74].

1.2 Outline

In this thesis, we first revisit the fundamental theories and experiments of ultracold atoms, optical lattices, and Bose-Hubbard models in Chapters 2-3. In Chapters 4-5, we discuss our theoretical work on two experiments focusing on non-equilibrium dynamics in optical lattice in the presence of disorder. Then in Chapter 6 we investigate the phase diagram of the 2D Bose-Hubbard with synthetic spin-orbit coupling.

Chapter 2 presents an overview of ultracold atoms in optical lattices. In an optical lattice, the non-interacting particles form a Bloch band structure and the wavefunctions are localized at each lattice site. Adding the inter-atomic interactions in the system we arrive at the Bose-Hubbard model which is the simplest model to capture the physics of many-body interacting atoms in an optical lattice.

Chapter 3 provides details about the zero-temperature phase diagrams of Bose-Hubbard models. We discuss the properties of the ground states of the Bose-Hubbard model. Static and time-dependent Gutzwiller mean-filed theories can be applied to study the phase transitions and non-equilibrium dynamics in the Bose-Hubbard model. Tunable disorder added to the optical lattice can lead to the disordered Bose-Hubbard model which hosts the exotic Bose glass phase. The realization of spin-orbit coupling with cold atoms paves the way to

study new spin-orbit coupled physics in the Bose-Hubbard model.

Chapter 4 presents the center-of-mass dynamics of the disordered Bose-Hubbard model in an optical lattice under a sudden shift of the harmonic trap center. Observations of center of mass dynamics offer a straightforward method to identify strongly interacting quantum phases of atoms placed in optical lattices. We theoretically study the dynamics of states derived from the disordered Bose-Hubbard model in a harmonic trapping potential with the time-dependent Gutzwiller method. Our findings show that the edge states in the trap allow center of mass motion even with insulating states in the center. We also find two different mechanisms for short and long-time scale dynamics of edge state transport in insulating phases. The center of mass velocity might aid in probing a Bose glass phase in cold atom experiments. The work in this chapter has led to the publication of Ref. [75].

Chapter 5 features our theoretical work on exploring localized states in strongly interacting bosons loaded into 2D optical lattices with disorder. We study the dynamics of the domain wall expansion of strongly interacting bosons in 2D optical lattices with disorder in a recent experiment [56]. We apply Gutzwiller mean-field theory (GMFT) to show that our simulation qualitatively describes the main experimental observations at zero temperature, which are a result of the competition between inter-particle interactions and disorder. By including a single phenomenological parameter and temperature, GMFT becomes quantitatively closer to experiments. Our results highlight the difficulty in unambiguously distinguishing Bose glass dynamics, which can be captured by GMFT, and many-body localization, which cannot be captured by GMFT. Further experimental study will be needed to identify many-body localization. The work in this chapter has led to the publication of Ref. [76].

Chapter 6 investigates the interplay of Rashba spin-orbit coupling and strong interaction in a 2D Hubbard model of two-component bosons in an optical lattice. Synthetic spin-orbit coupling with cold atoms can be taken to extremes rarely found in solids. We study a 2D

Bose-Hubbard model with strong spin-orbit coupling which can drive cause the transition from a Mott insulating state to a superfluid state. Our results show that spin-orbit coupling alone can generate phase-modulated superfluids with finite momentum. We investigate transitions between superfluids with two different phase patterns which have different spin-dependent momentum distributions. With the aid of time-of-flight measurements in cold atoms, superfluids with different phase pattern may be probed. The work in this chapter has led to the publication of Ref. [77].

Chapter 7 summarizes our main findings in this thesis and discuss possible future research directions.

1.3 Publication List

[1] **Mi Yan**, Hoi-Yin Hui, M. Rigol, and V. W. Scarola, "Equilibration Dynamics of Strongly Interacting Bosons in 2D Lattices with Disorder," *Phys. Rev. Lett.*, **119**, 073002 (2017)

[2] **Mi Yan**, Yinyin Qian, Hoi-Yin Hui, Ming Gong, Chuanwei Zhang, and V. W. Scarola, "Spin-orbit-driven transitions between Mott insulators and finite-momentum superfluids of bosons in optical lattices," *Phys. Rev. A*, **96**, 053619 (2017).

[3] **Mi Yan**, Hoi-Yin Hui, and V. W. Scarola, "Dynamics of Disordered States in the Bose-Hubbard Model with Confinement," *Phys. Rev. A*, **95**, 053624 (2017).

[4] M. Gong, Y. Qian, **Mi Yan**, V. W. Scarola, and C. Zhang, "Dzyaloshinskii-Moriya Interaction and Spiral Order in Spin-orbit Coupled Optical Lattices," *Nature: Scientific Reports*, **5**, 10050 (2015).

Chapter 2

Ultracold Atoms in Optical Lattices

In this chapter, we briefly review the theories and experiments of ultracold atoms in an optical lattice. We discuss the band structures of non-interacting atoms in an optical lattice. We use Wannier fucntions in the lowest band to construct the Bose-Hubbard Hamiltonian which describes the essential physics of many-body interacting systems in an optical lattice.

2.1 Optical Lattices

Neutral atoms are considered "ultracold" when temperatures are sufficiently low (typically $T < 0.1\mu K$) that the de Broglie wavelength is comparable to the distance between atoms. A neutral atom in a laser field with frequency ω gains an induced dipole moment [78]

$$\mathbf{d} = \alpha(\omega)\mathbf{E}, \tag{2.1}$$

where $\alpha(\omega)$ denotes the polarizability of the neutral atom. The external field interacts with the induced dipole to create a trapping potential [78]

$$V_{dip} = -\mathbf{d} \cdot \mathbf{E} \propto -\alpha(\omega)|\mathbf{E}|^2. \tag{2.2}$$

The trapping potential is proportional to the laser beam intensity.

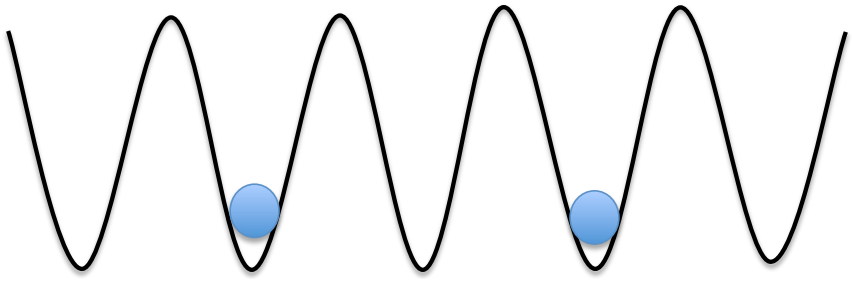

Figure 2.1: Schematic illustration of the interference pattern between two orthogonal optical standing waves creating a 1D periodic potential in which the atoms can tunnel between neighboring sites.

When we superimpose two identical and linearly polarized counter-propagating laser beams, we can get the electric field

$$E_x = E_0 \cos(kx - \omega t) + E_0 \cos(-kx - \omega t), \tag{2.3}$$

where $k = 2\pi/\lambda$ and λ is the laser wavelength. After time averaging for a cycle we have

$$\bar{E_x^2} = 2E_0^2 \cos^2(kx), \tag{2.4}$$

which gives a periodic trapping potential. This is a 1D optical lattice (see Figure 2.1). Addition of counter-propagating laser beams with orthogonal polarizations in y and z directons can lead to a 3D simple cubic lattice with potential

$$V(\mathbf{r})_{lat} = -V_0\big[\cos^2(kx) + \cos^2(ky) + \cos^2(kz)\big], \tag{2.5}$$

where V_0 measures the lattice potential depth. V_0 is normally described in units of the recoil energy

$$E_R = \frac{\hbar^2 k^2}{2m}, \tag{2.6}$$

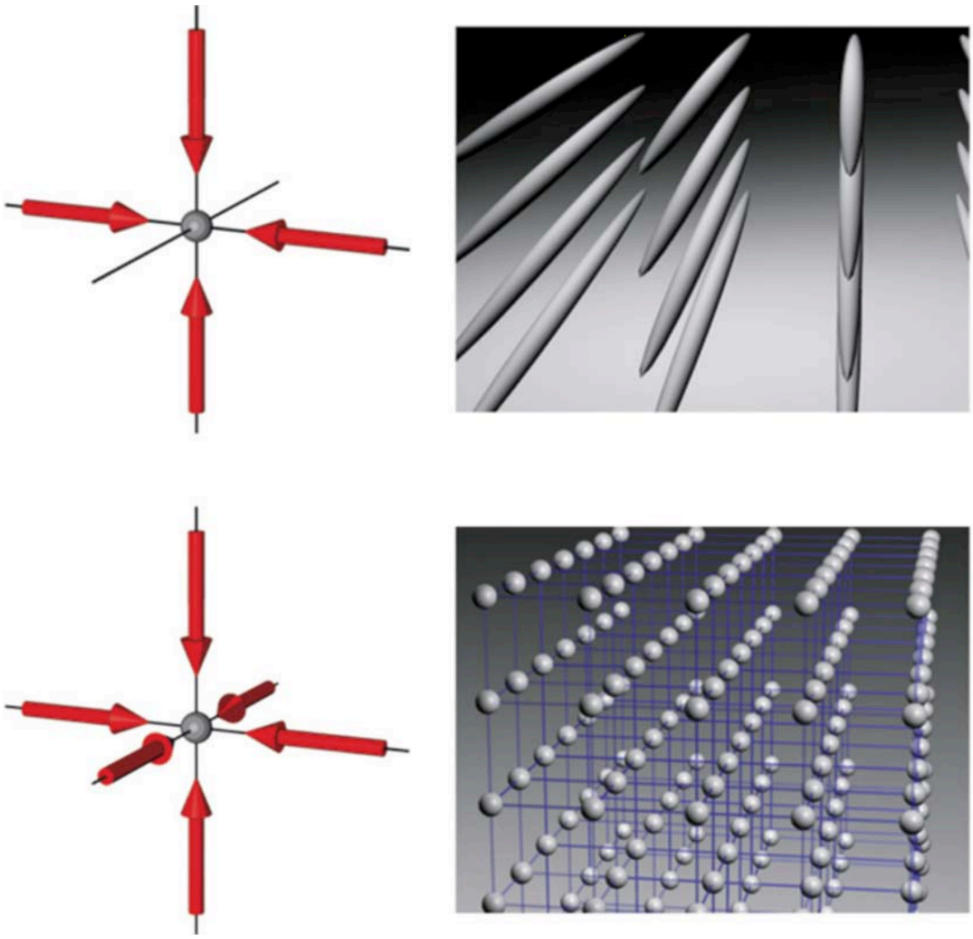

Figure 2.2: Schematic of 2D and 3D optical lattice potentials constructed by two or three pairs of interfering lasers. Adapted from Ref. [78].

where m is the mass of the neutral atom.

The geometry of the lattice can be conveniently changed by modifying the angles between the optical standing waves. Thus one can realize more complicated lattice configurations, such as triangular lattices [79], Kagomé [80, 81] lattices and honeycomb lattices [82, 83]. The precise controllability of all parameters is one important advantage of optical lattices, which provide an ideal platform for quantum simulations.

2.2 Non-interacting Particles in An Optical Lattice

Non-interacting particles in a homogeneous 3D simple cubic lattice can be described by the Hamiltonian

$$H = -\frac{\hbar^2}{2m}\nabla^2 - V_0\big[\cos^2(kx) + \cos^2(ky) + \cos^2(kz)\big], \tag{2.7}$$

where $k = \pi/a$ (a is the lattice spacing). Since the Hamiltonian Eq. (2.7) can be decoupled into independent identical differential equations along each direction, we can just consider the 1D case. The Schrödinger equation of atoms in a 1D periodic potential reads

$$\big[-\frac{\hbar^2}{2m}\frac{d^2}{dx^2} - s\cos^2(kx)\big]\phi(x) = E\phi(x), \tag{2.8}$$

where $s = V_0/E_R$ is a dimensionless parameter measuring the lattice depth. According to Bloch's theorem, we can write the energy eigenstates as the product of a plane wave e^{iqx} and a periodic function $u_q^{(n)}(x)$ possessing the same periodicity of the lattice potential as

$$\phi_q^{(n)}(x) = e^{iqx}u_q^{(n)}(x), \tag{2.9}$$

where n denotes band index and $\hbar q$ is the quasimomentum, a good quantum number in the lattice. The Fourier transform of $u_q^{(n)}(x)$ is

$$u_q^{(n)}(x) = \sum_j b_j^n(q)e^{i2kjx}. \tag{2.10}$$

Plugging Eq. (2.10) and Eq. (2.9) into Eq. (2.8), we can decompose the Schrödinger equation into a set of linear equations

$$\big[\frac{\hbar^2}{2m}(q+2kj)^2 - E_q^{(n)}\big]b_j^{(n)}(q) - \frac{s}{4}\big[b_{j-1}^{(n)}(q) + b_{j+1}^{(n)}(q)\big] = 0. \tag{2.11}$$

We can truncate at $|j|$ at large value to obtain the Bloch wave functions and the corresponding energy eigenvalues. Figure 2.3 shows Bloch bands for different lattice potentials. For $s = 0$, the particles are free and spetrum is quadratic in q. For a finite lattice depth, band structures appear. As the lattice depth increases, the bands become flatter. At $s = 10$, the lowest band has flattened considerably. In the absence of an optical lattice, the eigenstates of the free particles are plane waves. In the presence of a lattice potential, plane waves map into Bloch waves. Bloch waves spread over the entire lattice, so they are not the optimal basis set in a deep lattice. Since Bloch wavefunctions are periodic in quasimomentum space, they can be expressed in a basis of the maximally localized states as

$$\phi_q^{(n)}(x) = \frac{1}{\sqrt{N}}\sum_i e^{iqx}\omega^{(n)}(x - x_i), \tag{2.12}$$

where N is the number of lattice sites and

$$\omega^{(n)}(x - x_i) = \frac{1}{\sqrt{N}}\sum_q e^{iq(x_i - x)}u_q^{(n)}(x) \tag{2.13}$$

is called a Wannier function which is localized around the lattice site i. Wannier functions form a set of orthonormal basis states which can be used to describe atoms in an optical lattice. Figure 2.4 shows Wannier functions in a periodic potential with different lattice depths. For a shallow lattice $s = 4$, the visible side lobes of the Wannier function indicate a finite probability to find a particle at neighboring sites as well. For a deep lattice, $s = 20$, the side lobes become small and the Wanner function can be approximated by a Gaussian

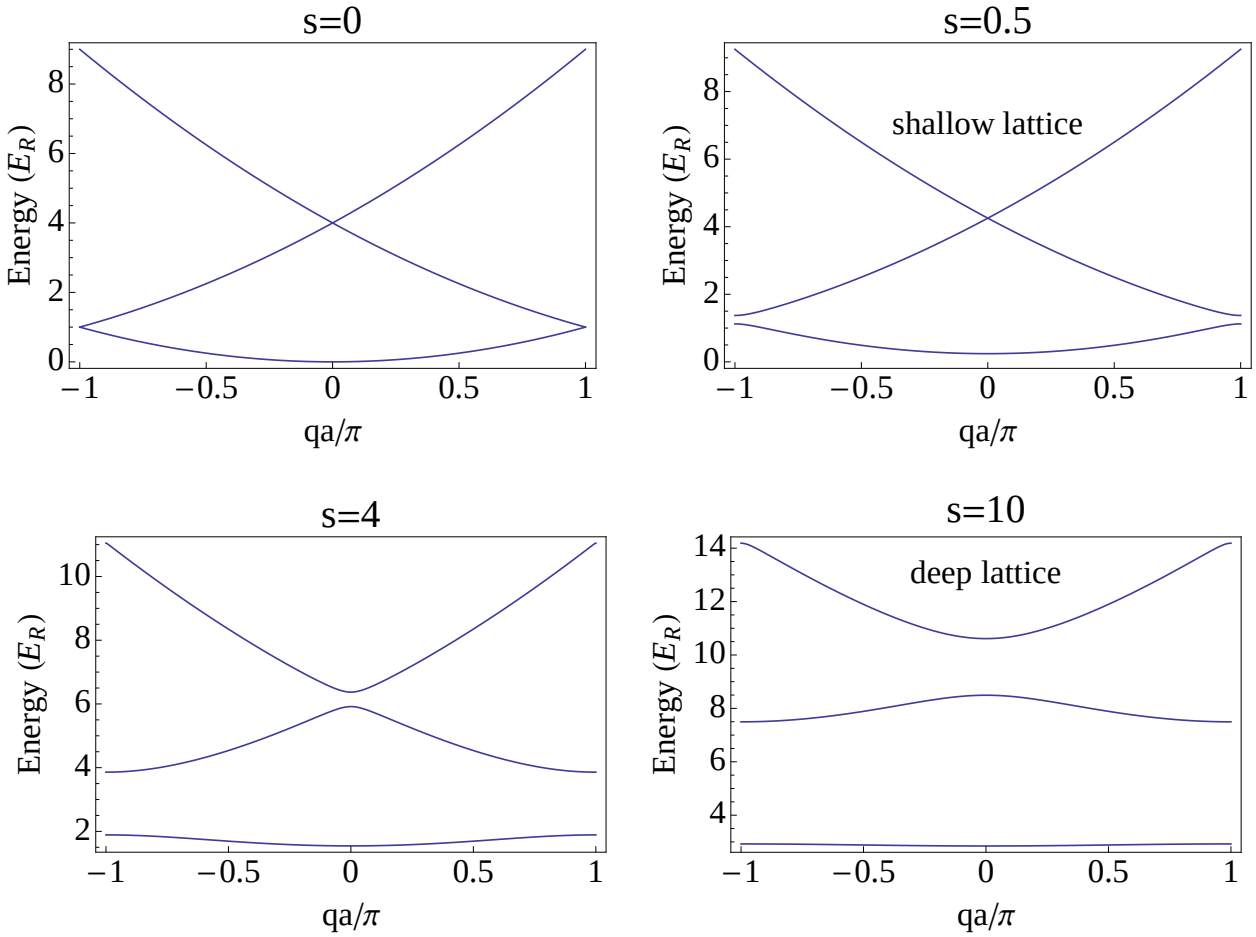

Figure 2.3: Band structures for a 1D optical lattice in the first Brillouin zone.

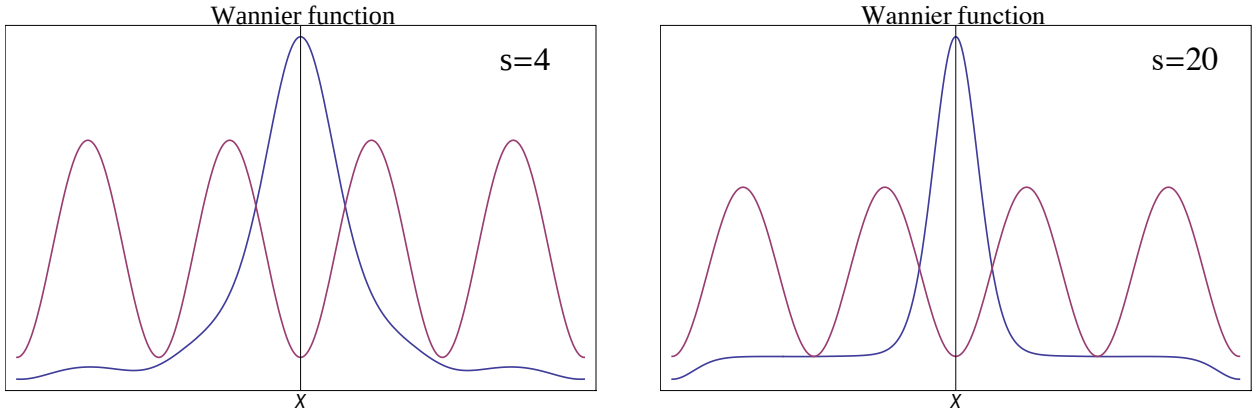

Figure 2.4: Wannier functions at the central site in a 1D optical lattice plotted together with a schematic lattice potential for two different lattice depths.

which decays exponentially away from the localized center. In an infinitely deep lattice, the Wannier states become the exact energy eigenstates.

2.3 Adding Onsite Interactions: The Bose-Hubbard Hamiltonian

In the previous section, we considered the non-interacting system and left out the interatomic interactions. Now we add the two-particle interaction term in the Hamiltonian for N bosons in an optical lattice,

$$H = \sum_{i=1}^{N} \left(-\frac{\hbar^2}{2m}\nabla_i^2 + V(\mathbf{r_i}) \right) + \frac{U_0}{2} \sum_{i,j} \delta(\mathbf{r_i} - \mathbf{r_j}), \tag{2.14}$$

where the effective interaction energy $U_0 = 4\pi a_s \hbar^2/m$ and a_s denotes the s-wave scattering length. The external potential

$$V(\mathbf{r_i}) = V_0(\mathbf{r}) + V_T(\mathbf{r}) \tag{2.15}$$

consists of two parts, where V_0 is the rapidly varying lattice potential, and V_T is normally a slowly varying harmonic trapping potential. The many-body Hamiltonian in Eq. (2.14) can be written in terms of field operators as

$$\begin{aligned} H &= \int d^3r \psi^\dagger(\mathbf{r}) \left[-\frac{\hbar^2}{2m}\nabla^2 + V(\mathbf{r}) + V_T(\mathbf{r}) \right] \psi(\mathbf{r}) \\ &\quad + \frac{U_0}{2} \int d^3r \psi^\dagger(\mathbf{r}) \psi^\dagger(\mathbf{r}) \psi(\mathbf{r}) \psi(\mathbf{r}). \end{aligned} \tag{2.16}$$

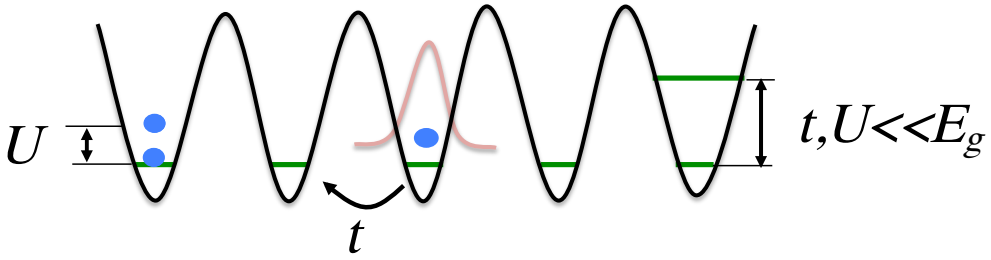

Figure 2.5: Schematic illustration of parameters in Bose-Hubbard model. The energy scale of the hopping amplitude t and interaction U are much smaller than the gap to the lowest excited band so the physics is focused only on the lowest band.

At low temperature $k_BT \leq E_g$, where k_B is the Boltzmann constant and E_g is the gap to the lowest excited band, the atoms cannot hop to the higher bands, so we can focus on the physics in the lowest band. We can expand the field operator in lowest band Wannier basis as

$$\psi(\mathbf{r}) = \sum_i b_i \omega(\mathbf{r} - \mathbf{r}_i), \tag{2.17}$$

where b_i destroys a particle at lattice site i.

Substituting Eq. (2.17) into the Eq. (2.16) and making the tight-binding approximation by considering only the onsite interaction and nearest neighboring hopping terms, we arrive at the Bose-Hubbard Hamiltonian [8],

$$H = -t \sum_{\langle ij \rangle} b_i^\dagger b_j + h.c. + \frac{U}{2} \sum_i n_i(n_i - 1) + \sum_i (\epsilon_i - \mu) n_i, \tag{2.18}$$

where $b_i^\dagger$ and b_i o are the annihilation and creation operators obeying the bosonic commutation relationship $[b_i, b_j^\dagger] = \delta_{ij}$, and $n_i = b_i^\dagger b_i$ denotes the particle number operator at lattice site i. In the grand canonical ensemble, we introduce the chemical potential μ to tune the number of particles.

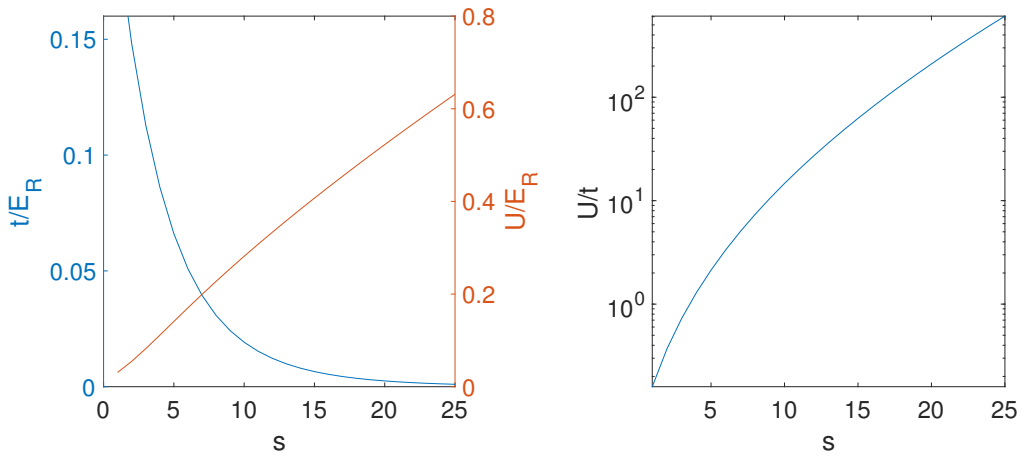

Figure 2.6: Hubbard parameters as a function of lattice depth. (a) Hopping amplitude t and interaction energy U in units of E_R for ^{87}Rb with lattice spacing $d = 406$nm and $a_s = 100a_0$ as a function of lattice depth. (b) The ratio of U/t versus lattice depth.

The hopping amplitude (see Figure 2.5) between nearest neighboring sites i and j reads

$$t = \int d^3r w(\mathbf{r} - \mathbf{r}_i) \left[-\frac{\hbar^2}{2m}\nabla^2 + V_0(\mathbf{r}) \right] w(\mathbf{r} - \mathbf{r}_j). \tag{2.19}$$

The onsite repulsion (see Figure 2.5) of two bosonic atoms at the same site is

$$U = U_0 \int d^3r |w(\mathbf{r})|^4. \tag{2.20}$$

The energy offset at lattice site i due to the harmonic trap reads

$$\epsilon_i = \int d^3r V_T(\mathbf{r}) |w(\mathbf{r} - \mathbf{r}_i)|^2 = V_T(\mathbf{r}_i). \tag{2.21}$$

We plot the Hubbard model parameters t and U as a function of the lattice depth in Figure 2.6(a). As the lattice depth increases, the overlap of the Wannier functions between neighboring sites decrease exponentially, so the hopping amplitude t decreases exponentially and interaction energy U increases. Figure 2.6(b) shows that the raito of U/t can be tuned

by the lattice depth in a wide range. This is a key ingredient for using cold atoms to study many-body quantum phase transitions.

Chapter 3

Bose-Hubbard Models

In this chapter, we review the phase diagrams of Bose-Hubbard models in the presence and absence of disorder. We discuss the static and dynamic Gutzwiller mean-field theories at zero temperature and the generalization to the finite temperature. The emergent Bose glass phase appears when disordering potential is added to the Bose-Hubbard model. We review the experimental realizations of disordered optical lattices and spin-orbit coupling with ultracold atoms.

3.1 Superfluid to Mott Insulator Phase Transition

In the previous chapter, we showed that the Bose-Hubbard model captures the essential physics of interacting cold atoms in optical lattices. The Bose-Hubbard Hamiltonian can be written as

$$\begin{aligned} H &= H_{kin} + H_{int} + H_{\mu}, \\ &= -t \sum_{\langle i,j \rangle} b_i^{\dagger} b_j + h.c. + \frac{U}{2} \sum_i n_i(n_i - 1) + \sum_i (\epsilon_i - \mu) n_i. \end{aligned} \tag{3.1}$$

The kinetic energy term H_{kin} which describes the hopping of atoms between the nearest neighboring sites delocalizes atoms over the entire lattice. The interaction energy term H_{int} which describes the repulsion between atoms on the same site localizes each atom on

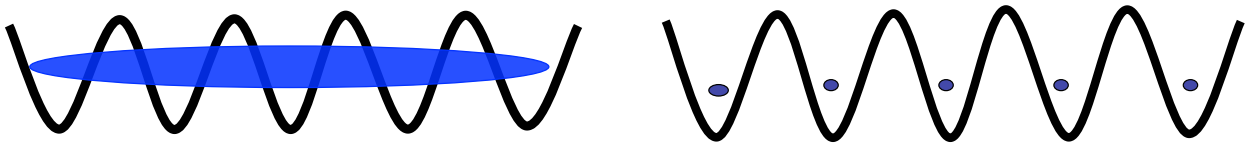

Figure 3.1: Schematic illustration of the density distribution in a lattice for superrluid (left panel) and Mott insulator (right panel) phases.

the lattice. The competition between the kinetic term and the interaction term leads to a quantum phase transition in this model.

In the weakly interacting limit $t \gg U$, the hopping term in the Hamiltonian plays the dominant role. All atoms condense to the zero-momentum state which has the lowest kinetic energy in the ground state,. The many-body wavefunciton can be expressed as

$$|\Psi_{\mathrm{SF}}\rangle_{U/t\approx 0} \propto \left(b^{\dagger}_{\vec{k}=0}\right)^{N} |0\rangle, \tag{3.2}$$

where $|0\rangle$ is the vacuum state with no atoms. A Bose-Einstein condensate in the presence of interactions can lead to a superfluid (SF) state, where each atom is spread out over the system (see Figure 3.1) with a well-defined macroscopic phase over the lattice sites. Due to the long-range phase coherence, if one applies a weak phase twist at one boundary of the system, there will be a response to this perturbation at the other boundary. Therefore the superfluid phase has a finite superfluid stiffness [84]

$$\rho_{\mathrm{s}} = \lim_{\theta\to 0} \frac{E_{\theta} - E_0}{tN\theta^2}, \tag{3.3}$$

where θ denotes the imposed phase twist and $E_{\theta} - E_0$ is the difference of the ground-state energies.

Since the atom number per site has large fluctuations, superfluid phase has finite compress-

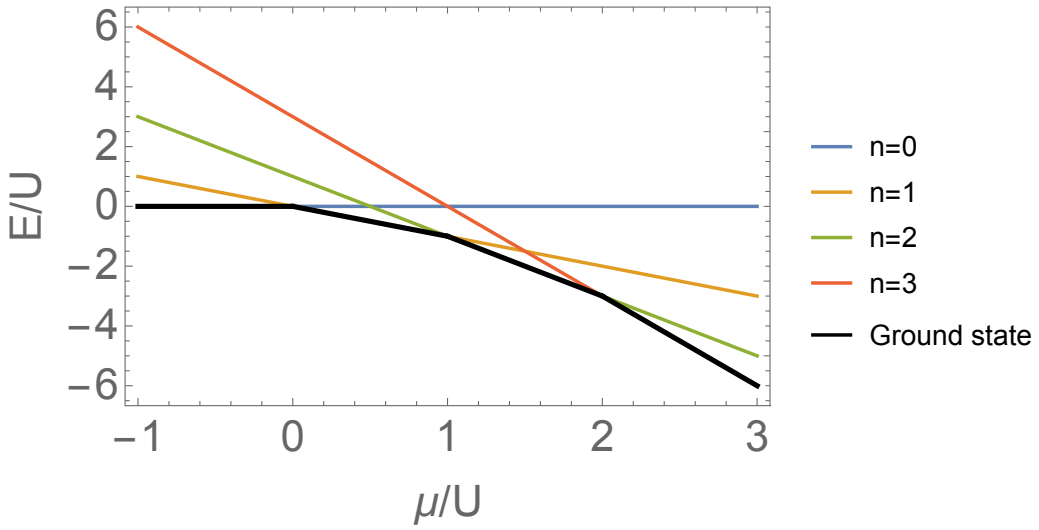

Figure 3.2: Level crossings between states with different occupation numbers for the Bose-Hubbard model in atomic limit $t = 0$. The ground states are highlighted with the thick dark line.

ibility

$$\kappa = \frac{\partial \langle n \rangle}{\partial \mu}. \tag{3.4}$$

In the strongly interacting limit $t \ll U$, the interaction term in the Bose-Hubbard Hamiltonian is dominant. At $t = 0$, the Hamiltonian reads

$$\begin{aligned} H &= H_{int} + H_{\mu}, \\ &= \frac{U}{2} \sum_i n_i(n_i - 1) + \sum_i (\epsilon_i - \mu) n_i. \end{aligned} \tag{3.5}$$

The Hamiltonian is decoupled and the eigenstates on each site have a well-defined atom number. In Figure 3.2, we plot the energy level crossings between states with different atom numbers. When $(n-1)U < \mu < nU$, the ground state has n atoms. Since the states with different integer fillings have a gap away from the level crossings, the states should be robust

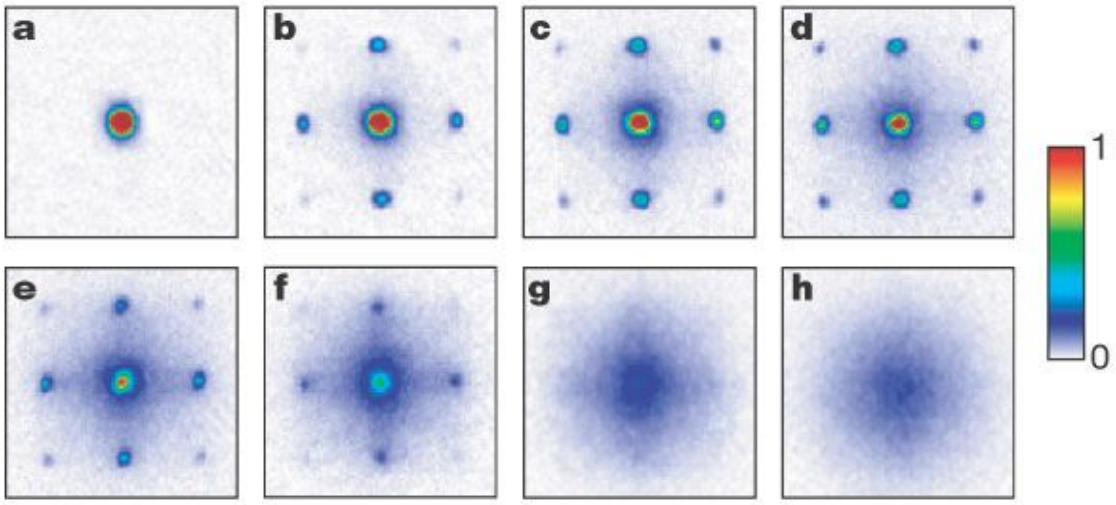

Figure 3.3: Experimental demonstration of the SF-MI transition with bosons in a simple cubic optical lattice. The time-of-flight experiments measure momentum distribution $n_k = b_k^\dagger b_k$ with different lattice depths **a**: $0E_R$; **b**: $3E_R$; **c**: $7E_R$; **d**: $10E_R$; **e**: $13E_R$; **f**: $14E_R$; **g**: $16E_R$; **h**: $20E_R$. In the superfluid regime for a shallow lattice, sharp interference maxima are visible. In the Mott insulator regime for a deep lattice, the interference pattern is washed away. Adapted from Ref. [6].

against small perturbations in the Hamiltonian, such as weak hopping or disorder. These ground states are called Mott insulators (MI).

The many-body wavefunction of Mott insulator can be written as a product state as

$$|\Psi_{\mathrm{MI}}\rangle \propto \prod_i \left(b_i^\dagger\right)^n |0\rangle. \tag{3.6}$$

In the MI ground state, each atom is localized on the lattice site, so the MI phase is incompressible ($\kappa = 0$) with vanishing stiffness ($\rho_s = 0$).

The SF-MI phase transition for cold atoms in an optical lattice was first observed by Greiner et al. [6]. Time-of-flight measurements in Figure 3.3 show the absorption imaging of interference patterns for different lattice depths. For shallow lattices in the supefluid regime, visible peaks in the interference patterns indicate the long range phase coherence across the

system. There is a macroscopic occupation of the lowest kinetic energy state with quasi-momentum equal to zero in the superfluid state. This can explain the satellite peaks which have momenta corresponding to the reciprocal lattice vectors.

In the Mott insulator regime for a deep lattice, all quasimomenta are occupied, so no sharp peaks are visible in the absorption images. Since there is no phase coherence in the Mott insulator, the interference pattern is lost.

3.2 Gutzwiller Mean-Field Theory

3.2.1 Static Gutzwiller method

To describe the phase transitions between the superfluid and Mott insulating states we use Gutzwiller mean-field theory. The Gutzwiller method assumes that the many-body wavefunction can be expressed as a product of localized states on each site. The Gutzwiller ansatz can be writen as

$$|\Psi_{\mathrm{GW}}\rangle = \prod_i \left[\sum_{n=0}^{\infty} f_n^{(i)} |n\rangle_i \right], \tag{3.7}$$

where $f_n^{(i)}$ denotes the probability amplitude to find n atoms at lattice site i.

Applying the ansatz to the Bose-Hubbard Hamiltonian in Eq. (3.1), we can write the expectation value for each terms in the Hamiltonian in terms of $f_n^{(i)}$.

$$\langle H \rangle = \langle H_{kin} \rangle + \langle H_{int} \rangle + \langle H_{\mu} \rangle, \tag{3.8}$$

with

$$\langle H_{kin}\rangle = -t\sum_{\langle i,j\rangle}\left(\langle b_i\rangle^*\langle b_j\rangle + \langle b_i\rangle\langle b_j\rangle^*\right), \tag{3.9}$$

where

$$\langle b_i\rangle = \sum_n f_n^{(i)*} f_{n+1}^{(i)}\sqrt{n+1} \tag{3.10}$$

is the mean-field superfluid order parameter,

$$\langle H_{int}\rangle = \frac{U}{2}\sum_i\sum_n |f_n^{(i)}|^2 n(n-1), \tag{3.11}$$

and

$$\langle H_{\mu}\rangle = \sum_i(\epsilon_i-\mu)\sum_n |f_n^{(i)}|^2 n. \tag{3.12}$$

We can find the ground state by minimizing $\langle H\rangle$ with respect to a set of amplitudes $\{f_n^{(i)}\}$. In the static case, the probability amplitudes $f_n^{(i)}$ are real numbers. The minimization can be done by using the conjugate gradient method [85, 86]. The Gutzwiller method has good agreement with quantum Monte Carlo away from phase boundaries in 2D and 3D [87, 88]. As a mean-field method, Gutzwiller approach is exact in infinite dimensions. Figure 3.4 shows the phase diagram of the homogeneous Bose-Hubbard Hamiltonian calculated by the Gutzwiller method.

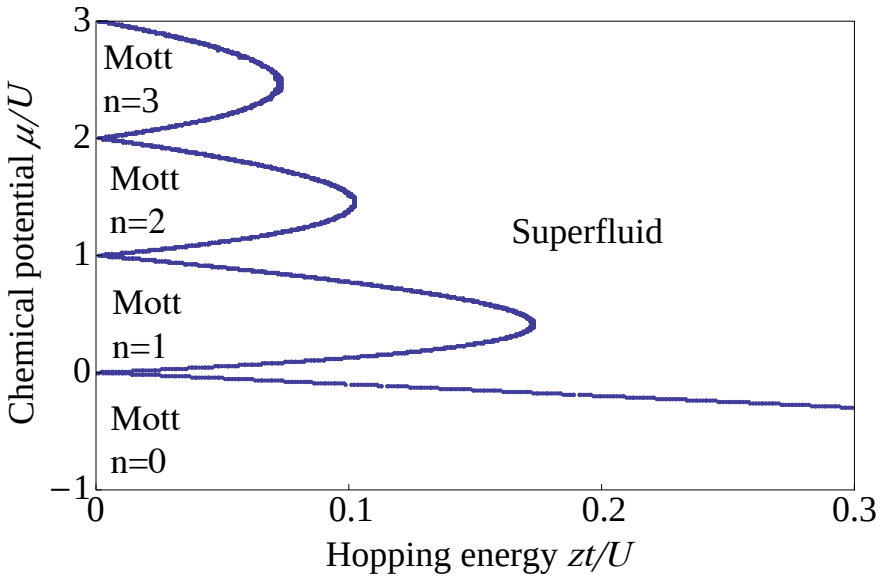

Figure 3.4: Zero-temperature mean-field phase diagram of the uniform Bose-Hubbard model. z is the coordination number. The $n = 0$ through $n = 3$ Mott lobes are labeled.

3.2.2 Time-Dependent Gutzwiller method

The Gutzwiller method can be generalized to time-dependent version to simulate the non-equilibrium dynamics in cold atom experiments. The time-dependent Gutzwiller ansatz is obtained by allowing the probability amplitudes $f_n^{(i)}(\tau)$ to be time dependent as

$$|\Psi_{\mathrm{GW}}\rangle(\tau) = \prod_i \left[\sum_{n=0}^{\infty} f_n^{(i)}(\tau)|n\rangle_i\right], \tag{3.13}$$

where τ denotes time.

According to the time-dependent variational principle, the equations of motion for the variational parameters $f_n^{(i)}(\tau)$ can be derived by minimizing $\langle\Psi_{\mathrm{GW}}(\tau)|i\hbar\frac{\partial}{\partial\tau} - H(\tau)|\Psi_{\mathrm{GW}}(\tau)\rangle$. For

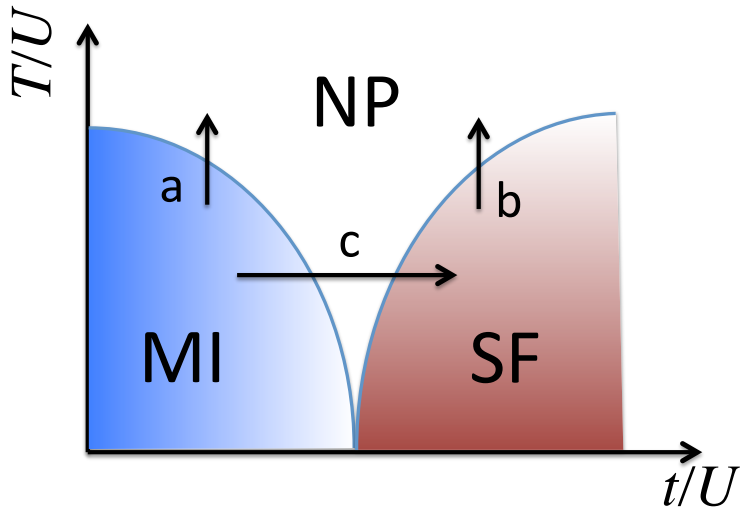

Figure 3.5: Schematic illustration of the finite-temperature phase diagram of the Bose-Hubbard model in a homogeneous system [90]. At finite temperature, a narrow quantum critical regime separates the Mott insulator (MI) and the superfluid (SF) phases. (a) Mott insulator to normal phase (NP) transition. (b) Superfluid to normal phase transition. (c) Mott insulator to Superfluid transition through the quantum critical regime. This is qualitatively different from classic phase transitions, which are normally induced by the competition between entropy and internal energy.

the Bose-Hubbard Hamiltonian in Eq. (3.1), the equations of motions [89] for $f_n^{(i)}$ are

$$\begin{aligned} \mathrm{i}\hbar\partial_\tau f_n^{(i)} &= \left[\frac{U}{2}n(n-1) + n(\epsilon_i - \mu)\right] f_n^{(i)} \\ &- t\sum_{\langle i,j\rangle}\left(\psi_j^*\sqrt{n+1}f_{n+1}^{(i)} + \psi_j\sqrt{n}f_{n-1}^{(i)}\right), \end{aligned} \tag{3.14}$$

where $\psi_j = \langle b_j\rangle = \sum_n \sqrt{n} f_{n-1}^{(j)*} f_n^{(j)}$ is the time-dependent mean-field superfluid order parameter. The set of coupled first order differential equations can be solved in the standard way, for instance by using the Runge-Kutta method. This will allow us to compute all correlation functions as a function of time and explore the dynamics of the system.

3.2.3 Finite-Temperature Gutzwiller method

Temperature plays an important role in cold atom experiments. Finite temperature can lead to decoherence and excitations, so it is necessary to study the thermal effects in the phase transitions and non-equilibrium dynamics of cold atoms in Bose-Hubbard model. At nonzero temperature, the thermal fluctuation leads to a new phase - the normal phase (NP). Figure 3.5 shows the schematic illustration of the finite-temperature phase diagram of the Bose-Hubbard model. Finite temperature effects drive the transition between the superfluid and normal phases by destroying the condensates. Also, thermal fluctuations can cause a crossover between the Mott insulator and normal phases.

The Gutzwiller approach is also readily generalized to finite temperature. The total density matrix of the system within Gutzwiller mean-feild theory factorizes over the lattice as

$$\hat{\rho}\left(\tau\right)=\prod_{\mathbf{i}}\hat{\rho}_{\mathbf{i}}\left(\tau\right)=\prod_{\mathbf{i}}\left[\sum_{m,n=0}^{\infty}\alpha_{mn}^{(\mathbf{i})}\left(\tau\right)\left|m\right\rangle_{\mathbf{ii}}\left\langle n\right|\right], \tag{3.15}$$

where $|n\rangle_{\mathbf{i}}$ is the state with n bosons at site $\mathbf{i}$. We can use this ansatz to decouple the Bose-Hubbard Hamiltonina in Eq. (3.1) into single-site Hamiltonians

$$\hat{H}_{\mathbf{i}}^{\mathrm{MF}}=-J(\phi_{\mathbf{i}}^{*}\hat{b}_{\mathbf{i}}+\phi_{\mathbf{i}}\hat{b}_{\mathbf{i}}^{\dagger})+(U/2)\sum_{\mathbf{i}}\hat{n}_{\mathbf{i}}(\hat{n}_{\mathbf{i}}-1)+(\epsilon_{\mathbf{i}}-\mu)\hat{n}_{\mathbf{i}}, \tag{3.16}$$

where $\phi_{\mathbf{i}}=\sum_{\mathbf{j}\in\mathrm{nn}_{\mathbf{i}}}\mathrm{Tr}(\hat{\rho}_{\mathbf{j}}\hat{b}_{\mathbf{j}})$ sums over neighbor sites to $\mathbf{i}$. Substituting Eq. (3.15) into the von Neumann equation,

$$i\partial_{\tau}\hat{\rho}=[\hat{H},\hat{\rho}], \tag{3.17}$$

we arrive at the equation of motion for $\alpha^{(\mathbf{i})}_{mn}$:

$$\begin{aligned} i\partial_\tau \alpha^{(\mathbf{i})}_{m,n} = &- J\phi^*_{\mathbf{i}} \left[\sqrt{m+1}\alpha^{(\mathbf{i})}_{m+1,n} - \sqrt{n}\alpha^{(\mathbf{i})}_{m,n-1}\right] \\ &- J\phi_{\mathbf{i}} \left[\sqrt{m}\alpha^{(\mathbf{i})}_{m-1,n} - \sqrt{n+1}\alpha^{(\mathbf{i})}_{m,n+1}\right] \\ &+ \frac{U}{2}\left[m\left(m-1\right) - n\left(n-1\right)\right]\alpha^{(\mathbf{i})}_{m,n} \\ &+ \left(\epsilon_{\mathbf{i}} - \mu\right)\left(m-n\right)\alpha^{(\mathbf{i})}_{m,n}. \end{aligned} \tag{3.18}$$

3.3 Disordered Bose-Hubbard Model

3.3.1 Disordered Optical Lattice

The study of the interplay between interaction and disorder has always been an interesting topic in condensed matter physics. In cold atom experiments, a disorder potential can be produced by using a laser speckle pattern. Figure 3.6 shows that the disordered distribution of the laser beam can be projected onto the cold atoms in the optical lattice, generating a random potential proportional to the laser intensity. The disorder strength is fully under control and tunable to a wide range. The disordered Bose-Hubbard model has been realized by the DeMarco group [36]. The Hamiltonian reads

$$H = -\sum_{\langle ij\rangle} t_{ij} b_i^\dagger b_j + h.c. + \sum_i \frac{U_i}{2} n_i(n_i-1) - \sum_i \left(\mu + \delta\mu_i\right) n_i, \tag{3.19}$$

in which Hubbard parameters t, U and ϵ become site-dependent due to the changes in the Wannier functions by the disorder (see Figure 3.7).

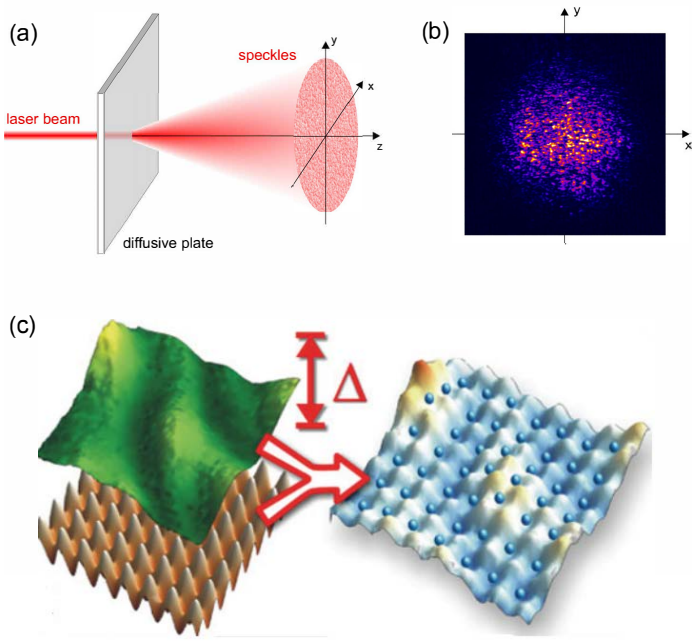

Figure 3.6: Illustration of laser configuration producing a disordered optical lattice. (a) A speckle pattern is generated by shining a light through a diffusive plate with randomly-distributed impurities. (b) The intensity distribution of a typical laser speckle pattern. (c) The speckle pattern is added onto a clean lattice resulting in a disordered optical lattice. (a) and (b) are adapted from Ref. [34], (c) is adapted from Ref. [36].

3.3.2 Bose Glass Phase

In the following consider the effect of the onsite disorder in the disordered Bose-Hubbard Hamiltonian

$$H = -t \sum_{\langle ij \rangle} b_i^\dagger b_j + h.c. + \frac{U}{2} \sum_i n_i(n_i - 1) - \sum_i (\mu + \delta\mu_i)\, n_i, \tag{3.20}$$

where $\delta\mu_i \in [-\Delta/2, \Delta/2]$ is an onsite random potential with uniform distribution.

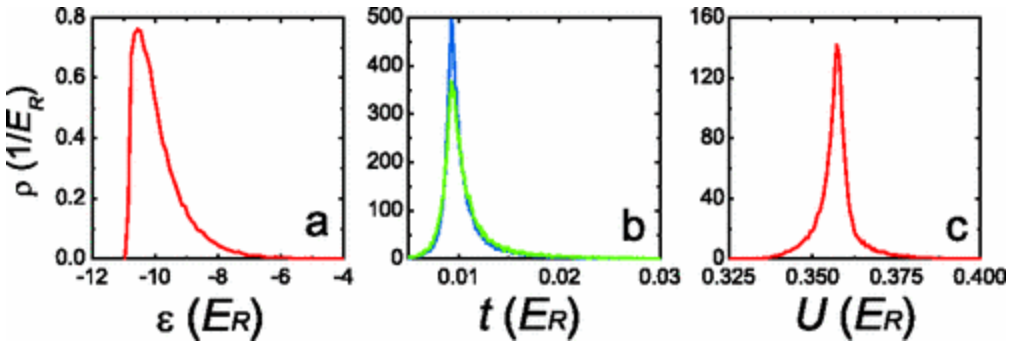

Figure 3.7: Distribution of Hubbard parameters for lattice depth $s = 14E_R$ and disorder strength $\Delta = 1E_R$. Adapted from Ref. [36].

	ρ_s	κ
Superfluid	$\neq 0$	$\neq 0$
Mott insulator	$= 0$	$= 0$
Bose glass	$= 0$	$\neq 0$

Table 3.1: List of phases and related order parameters: superfluid stiffness ρ_s and compressibility κ.

Figure 3.8 demonstrates the schematic phase diagram of the disordered Bose-Hubbard Hamiltonian. In the presence of disorder, a new exotic phase called the Bose glass (BG) emerges in the phase diagram. The Mott lobe gradually shrinks in the as disorder increases. When disorder is strong enough such that $\Delta > U$, the Mott lobe will completely vanish.

The Bose glass is a compressible insulator. In the Bose glass phase, disorder can convert the MI to isolated SF puddles embedded in an insulator background. Particles can hop between neighboring sites in the superfluid puddles without an energy cost so the Bose glass is compressible and gapless. These isolated superfluid puddles cannot percolate from one side of the system to the other, so it remains insulating (see Figure 3.9). The increase of the disorder strength can convert Mott insulators or superfluids into Bose glass [7, 91, 92], and it can also convert Bose glasses into superfluids which are called "re-entrant superfluids" [93].

Table 3.1 shows the different phases and the corresponding order parameters which distinguish them in the disordered Bose-Hubbard model.

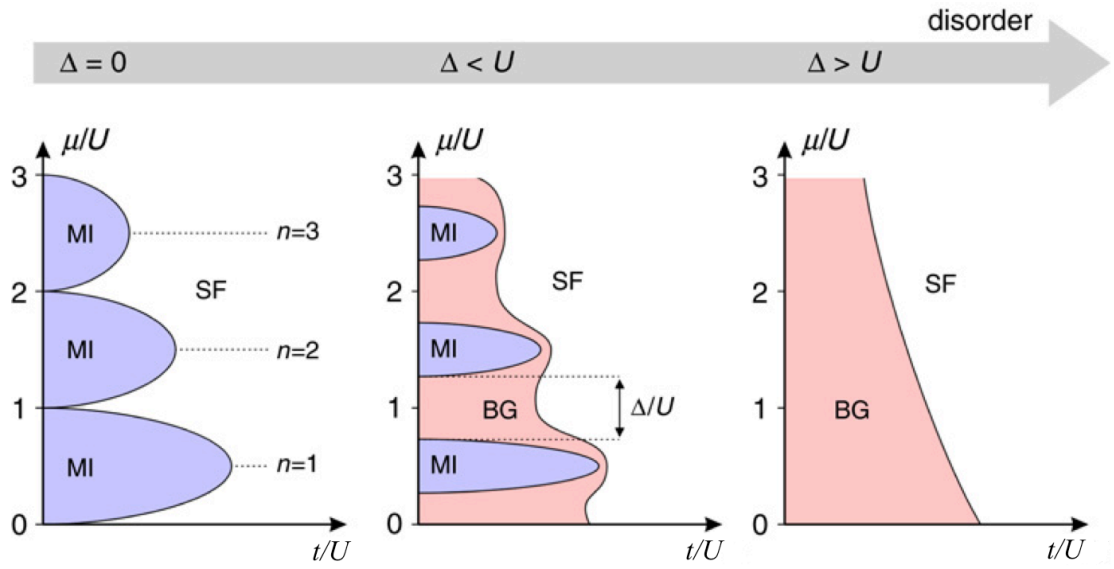

Figure 3.8: Schematic phase diagram of the disordered Bose-Hubbard model adapted from Ref. [34]. The left panel shows the phase diagram in a clean system. The middle panel shows that the Mott lobe progressively shrinks in the presence of weak box disorder. The right panel demonstrates that in the strong disorder $\Delta > U$ case, Mott lobes will be completely washed away.

3.3.3 Dynamics of Disordered Optical Lattices

The study of the dynamics of cold atoms in the disordered Bose-Hubbard model is of particular interest to our group, because it gives us a deeper understanding of the interplay of disorder, many-body strong interactions and non-equilibrium effects which are three important yet difficult topics in condensed matter physics. The study of the dynamics may also help us in identifying the Bose glass phase.

Bose glass, first predicted by Fisher et al. in a seminar paper [7] in 1989, has not been unambiguously identified. Measurements of excitation spectrum and compressibility are very difficult in cold atom experiments. Some schemes have been proposed in optical lattices to probe the Bose glass phase, for example, the DeMarco group [37] measured the center-of-mass (COM) dynamics after applying a rapid impulse to shift the harmonic trap (see Figure 3.10).

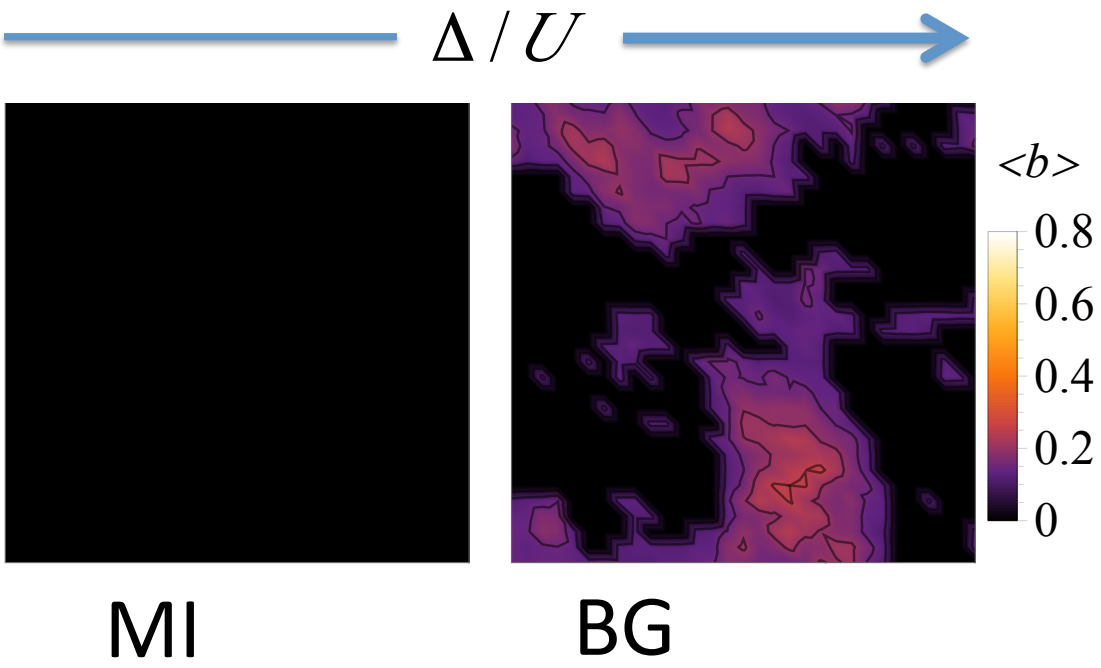

Figure 3.9: Illustration of mean-field superfluid order parameters as a function of increasing disorder strength for the disordered Bose-Hubbard model with strong interactions. Disorder can convert the Mott insulator to isolated SF puddles embedded in an insulating background. In the Bose glass phase, particles can tunnel between neighboring sites within the superfluid puddles without energy cost, but particles cannot percolate from one side of the sample to the other. Therefore Bose glass phase has finite compressibility but vanishing superfluid stiffness.

It is an analogue of measuring the conductivity in solid state physics by applying an external electric field. Figure 3.10 shows that at a fixed lattice depth, the COM velocity is suppressed as the disorder strength is increased. Therefore it suggests that there is a disorder induced insulator in the optical lattice. However we do not have a clear understanding of what kind of insulator it is. It might be Bose glass or another insulator. Motivated by this experiment, we want to use time-dependent Gutzwiller methods to study the COM dynamics in the disordered Bose-Hubbard model to try to find some signatures of Bose glass that can be used in experiments for probing the Bose glass phase. The details of this work will be presented in Chapter 4.

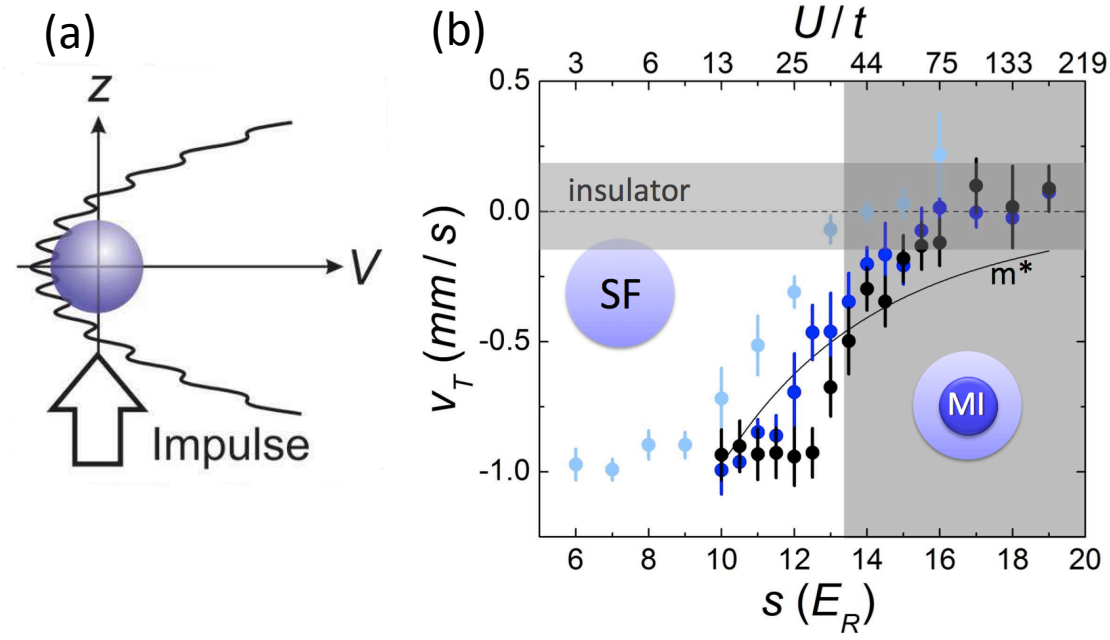

Figure 3.10: (a) Schematic illustrating application of an impulse to the atoms to initialize the dynamics. (b) Measurements of center-of-mass velocity V_T of the atoms as a function of the lattice depth s for three disorder strengths: $\Delta = 0E_R$ (black), $0.75E_R$ (dark blue) and $3.0E_R$ (light blue), after applying an impulse to initialize the dynamics. Adapted from Ref. [37].

The dynamical Gutzwiller method can also be used to explore localization in cold atom experiments with strongly-interacting bosonic systems in the presence of disorder. Many-body localization (MBL) [49–51] is a remarkable quantum phase, in which eigenstate thermalization does not occur. In a recent experiment [56] in the Bloch group, MBL with bosons has been studied in a 2D optical lattice with disorder. A Mott insulator was prepared in a harmonic trap in a deep optical lattice. One half of the bosons in the system was then removed and the remaining half was allowed to evolve by lowering the lattice depth, in the absence or presence of disorder. During the dynamics, the local density was measured to

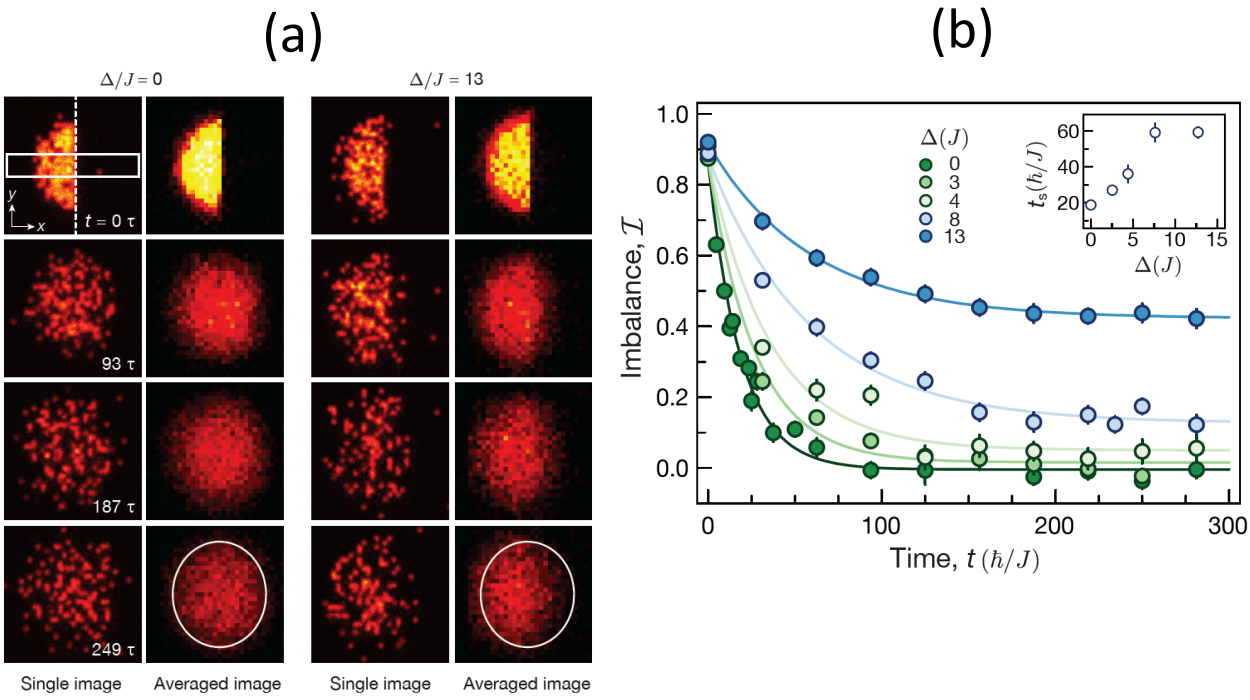

Figure 3.11: (a) The time evolution of the initial density step without disorder (left panel) and with strong disorder (right panel). (b) The time evolution of the density imbalance $\mathcal{I}$ shown for different disorder strengths $\Delta/J = 0$ (dark green), $\Delta/J = 3$ (medium green), $\Delta/J = 4$ (light green), $\Delta/J = 8$ (light blue) and $\Delta/J = 13$ (dark blue). Note that J is the hopping parameter. Adapted from Ref. [56].

study the evolution of the imbalance between the initially occupied and unoccupied halves of the system (see Figure 3.11(a)). In the absence of disorder, or for weak disorder, the density imbalance vanished at long times. But beyond a certain disorder strength, the density imbalance appeared to saturate to a nonzero value (see Figure 3.11(b)). This was taken as evidence for MBL. We will discuss our theoretical study of this experiment in Chapter 5.

3.4 Spin-Orbit Coupled Bose-Hubbard Model

Spin-orbit coupling (SOC), the interaction between a quantum particle's spin and its center-of-mass motion, plays an important role in modern condensed matter physics. The combi-

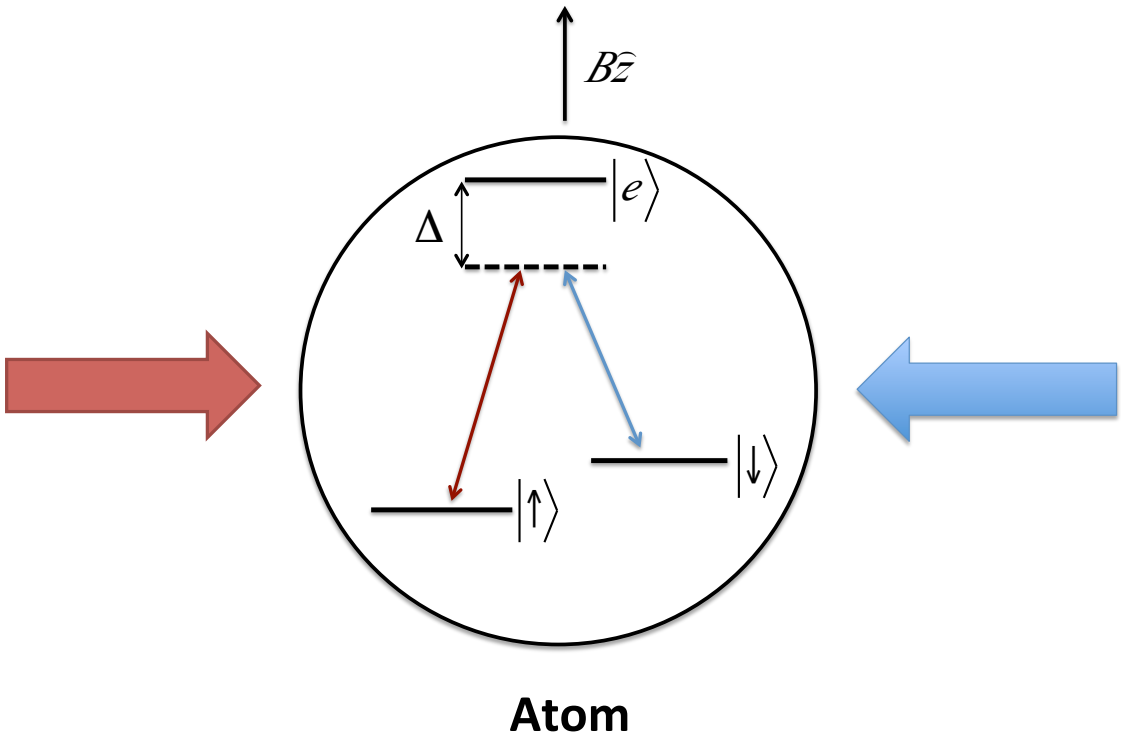

Figure 3.12: Schematic illustration of spin-orbit coupling in ultracold atoms. Two counter-propagating laser beams along $\hat{x}$ couple two spin states of an atom in a a Zeeman field along $\hat{z}$ by a resonant stimulated two-photon Raman transition. An atom in an internal state labeled as $|\uparrow\rangle$ absorbs a photon from the left light and is excited to a virtual level, then immediately flips to the internal state labeled as $|\downarrow\rangle$ by spontaneously emitting another photon into the right light. The lasers are detuned from the excited state by Δ. The stimulated two-photon Raman process results in a momentum transfer to the atom which leads to the coupling of spin and momentum in the single-particle eigenstates [94].

nation of spin-orbit coupling and the periodic lattice potential resulted in recent discoveries of topological insulators [95], topological superconductors [96], and the quantum spin-Hall effect [97]. Many-body strongly correlated systems with spin-orbit coupling pave the way to realize exotic spin models [98, 99] and study corresponding quantum phase transitions.

In cold atoms, spin-orbit coupling can be implemented by two-photon Raman transitions between atomic hyperfine states. Figure 3.12 demonstrates the basic principle of this laser coupling scheme. Two counter propagating laser beams couple two internal hyperfine atomic states through a two-photon process, wherein an atom in state $|\uparrow\rangle$ absorbs a photon from

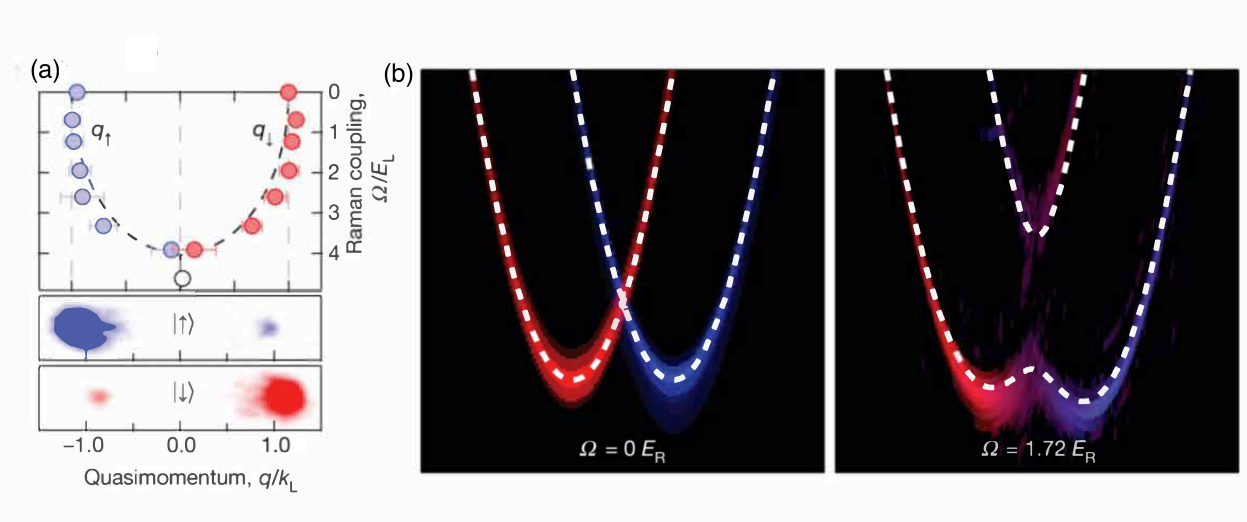

Figure 3.13: Experimental demonstration of laser coupling schemes. The laser beams link the atom's spin to the motion to create a characteristic spin–orbit coupled energy-momentum dispersion relation. (a) Measurements of energy minimum or minima locations as a function of Raman coupling strength. (b) Measurements of dispersion relation in a ^{6}Li atomic gas, before and after Raman coupling compared with the theoretically predicted dispersion (white dashed curves). Adapted from Ref. [100].

the left beam, de-excites by emitting a photon to the right beam and flips to state $|\downarrow\rangle$. The two-photon process gives the atom a momentum kick, resulting in a coupling between the spin and momentum.

Figure 3.13 shows a current experiment which implements the two-photon Raman process to realize the spin-orbit coupling in cold atoms. We can see the energy-momentum dispersion relation is altered due to the coupling between the atom's spin and momentum. The tunability of the Raman coupling parameters in cold atom experiments provides a great platform to explore new physics with spin-orbit coupling [65–74].

Motivated by the recent progress in optical lattice experiments, we can add in the traditional Bose-Hubbard model a Rashba spin-orbit coupling term

$$V_{\mathrm{SO}} = -i\lambda(\hat{\sigma}_x\partial_y - \hat{\sigma}_y\partial_x), \tag{3.21}$$

where λ is the strength of Rashba spin-orbit coupling and $\hat{\sigma}_x$ and $\hat{\sigma}_y$ are Pauli matrices.

The spin-orbit coupled Bose-Hubbard model reads

$$\begin{aligned} H &= -t\sum_{\langle ij\rangle}\Psi_i^\dagger\Psi_j + \frac{U}{2}\sum_{i\sigma} n_{i\sigma}(n_{i\sigma}-1) \\ &+ U_{\uparrow\downarrow}\sum_i n_{i\uparrow}n_{i\downarrow} - \mu\sum_{i\sigma} n_{i\sigma} \\ &+ i\lambda\sum_{\langle ij\rangle}\Psi_i^\dagger\vec{e}_z\cdot(\vec{\sigma}\times\vec{d}_{ij})\Psi_j + H.c., \end{aligned} \tag{3.22}$$

where $\Psi_i = (b_{i\uparrow}, b_{i\downarrow})^T$ denotes a two-component operator destroying a boson the lattice site i, $n_{i\sigma} = b_{i\sigma}^\dagger b_{i\sigma}$ measures the number of atoms at lattice site i with spin σ, $U_{\uparrow\downarrow}$ is the onsite interaction between bosons with different spin species, and $\vec{d}_{ij}$ denotes the unit vector pointing from sites i to j. The last term introduces a spin-dependent hopping with strength λ. The competition between the spin-independent hopping t and spin-dependent hopping λ leads to interesting phase transitions in this model. In Chapter 6 we will explore the rich phase diagram of the spin-orbit coupled Bose-Hubbard model.

Chapter 4

Dynamics of Disordered States in Bose-Hubbard Model with Harmonic Confinement

The work described in this chapter was published as:

Mi Yan, Hoi-Yin Hui, and V. W. Scarola, "Dynamics of Disordered States in the Bose-Hubbard Model with Confinement," *Phys. Rev. A*, **95**, 053624 (2017) [75].

I contributed all the calculations and visualizations in this paper under Professor Vito Scarola's supervision. All authors analyzed and discussed the results and contributed in writing the manuscript.

4.1 Introduction

Ultracold atomic and molecular gases placed in optical lattices realize strongly correlated states of matter captured by Hubbard models [6, 8, 42, 101]. Hubbard models are known to support fundamentally important states that serve as paradigms for understanding quantum

collective behavior in solids. New methods to observe and study these collective phases in optical lattices have been invented to better probe interesting quantum behavior. Example diagnostics include Bragg spectroscopy [14, 15] (applied recently to measure [102] local antiferromagnetic spin correlations [103–105]), noise spectroscopy [16–18], and center of mass transport.

Center of mass transport experiments in optical lattices are often used to probe response in direct analogy to transport in solids. In optical lattice transport the center of mass is shifted and the dynamics is observed using time of flight. Transport studies of bosonic atoms in optical lattices have been used to study superfluid and Mott insulating states, states of the Bose-Hubbard model [27, 36, 37, 106–113]. When the system is in a superfluid state it oscillates within the trapping potential. The Mott insulator shows, by contrast, essentially no dynamics for very strong interactions. More recently, disorder has been implemented [23–40] to further probe glassy states expected from a competition between strong disorder and inter-particle interactions. In the experiments of Ref. [37] it was argued that the suppression of center of mass transport indicated the presence of a Bose-glass, a state of the Bose-Hubbard phase diagram induced by disorder.

Optical lattice transport experiments have fundamental and crucial differences from solid state transport. Particles in optical lattices are, to a good approximation, isolated systems. The absence of a heat bath prevents direct thermalization. Thermalization of initial states occurs via inter-particle interactions [114]. The system can therefore be slow to thermalize during transport because there is no external bath. Furthermore, the absence of lattice phonons avoids conventional assumptions of dephasing often invoked in solids. Other thermal effects are also very different. For example, the absence of a particle number bath prevents transport via variable range hopping. But the most pronounced differences arise from strong trapping. In optical lattice experiments the response of the center of mass must

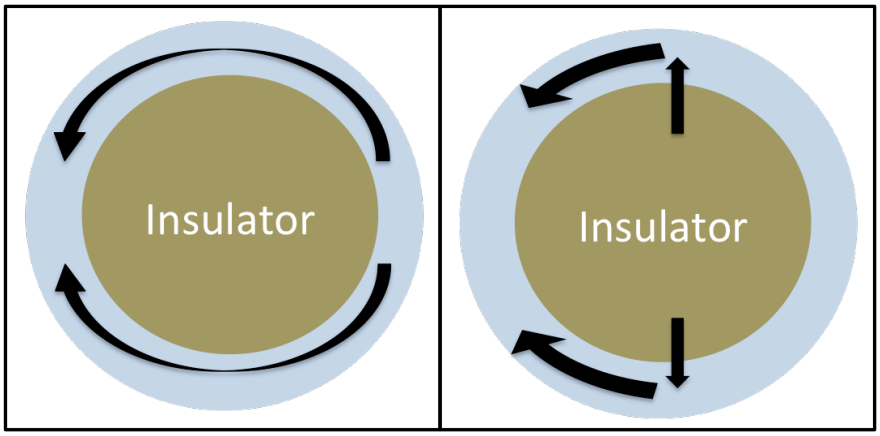

Figure 4.1: Schematic showing two distinct mechanisms for center of mass dynamics after an initial shift of the trapping potential to the left. The center of the system is in an insulating phase (either the Mott insulator or the Bose-glass) but the edges are superfluid. Left Panel: We find that initially (on times scales shorter than the inter-site tunneling) the edge superfluid quickly moves around the insulator to the left to redistribute the total center of mass. Right Panel: We find that (on time scales much larger than the inter-site tunneling) a two stage process shifts the center of mass. First particles slowly tunnel out of the central insulator into the edges (vertical arrows). Then the particles quickly move to the left along the edge to redistribute the center of mass.

be understood in the context of a parabolic trapping potential which mixes phases in the trap and leads to edge states [8, 101, 115].

In this chapter we study the dynamics of bosons in a disordered Bose-Hubbard model in the presence of a trap. We seek to identify the precise mechanisms of transport in a trap and correlate the response with known phases. We will include disorder to study the dynamic response of the following phases to an external field: a disordered superfluid, a Bose-glass, and a disordered Mott insulator (as in Ref. [116] but in the presence of confinement). We will also focus entirely on the zero temperature response to identify purely quantum transport effects that should underpin low temperature experiments.

We find that the insulating states (Bose-glass and Mott insulator) have center of mass motion that is dominated by edge effects. Our simulations show that when the center of the system is in an insulating phase, it remains motionless under a trap shift, while the edge states move,

and therefore, so does the center of mass. Fig. 4.1 shows a schematic depicting distinct mechanisms of transport that we find. The left panel depicts what we find at short times (with respect to the single-particle inter-site tunneling time scale). Here we find that the edge states surrounding an insulator quickly move and dominate the center of mass motion.

But at long times we find that disordered insulating states drift slowly (the center of mass moves only a site or two for times on the order of 100 times the inter-site tunneling). The insulating states reach a terminal velocity that does not change with the applied field. This is contradictory to the conventional Drude-type picture of particle motion. We instead propose a two-stage process in which slow tunneling into edge states (right panel of Fig. 4.1) slowly moves the center of mass while leaving the central insulator motionless.

Our results reveal mechanisms for center of mass transport. The presence of a trap leads to edge states. The edge states are responsible for motion of the center of mass via two distinct mechanisms, one at short times and one at long times. These mechanisms also differ from conventional pictures of bulk transport in solids where an applied field leads to an average drift of all particles. Our results establish a basis for interpreting measurements of center of mass dynamics of atoms trapped in optical lattices.

4.2 Model

Ongoing optical lattice experiments containing bosonic alkali atoms are accurately captured by the Bose-Hubbard model [8]. Controlled disorder, applied through speckle laser light or incommensuration [101], can significantly alter the phase diagram and therefore impact transport. Transport experiments [37] can be understood from an interplay of temperature, disorder, trapping, and interactions [117]. In this work we study zero temperature effects to focus on just disorder, trapping, and interactions.

We study the dynamics of states of the disordered Bose-Hubbard model to assess transport properties in a parabolic trapping potential. The Bose-Hubbard Hamiltonian is given by:

$$H = -t \sum_{\langle i,j \rangle} b_i^\dagger b_j + \frac{U}{2} \sum_i \hat{n}_i(\hat{n}_i - 1) + \sum_i \mu_i \hat{n}_i, \tag{4.1}$$

where $b_i^\dagger$ creates a boson at the site at lattice position $\mathbf{R}_i$ and $\hat{n}_i = b_i^\dagger b_i$ is the number operator. Here $\langle i, j \rangle$ denotes summation over nearest neighbor sites. t is the single-particle nearest neighbor hopping amplitude and U denotes the onsite repulsive interaction energy. The spatially inhomogeneous chemical potential is:

$$\mu_i = -\mu + \Omega |\mathbf{R}_i - \mathbf{R}_0(\tau)|^2 + \epsilon_i, \tag{4.2}$$

where the central chemical potential, μ, tunes the average density. Ω is the strength of the harmonic trapping potential and $|\mathbf{R}_i - \mathbf{R}_0(\tau)|$ defines the distance between a site i and the trap center, $\mathbf{R}_0(\tau)$. We work on a two-dimensional square of side lengths $L = L_x = L_y$. We choose L so that the density for edge sites vanishes for all trap frequencies used. Distances are measured in units of the lattice spacing, a. The trap center is a function of time, τ, and, in what follows, will be immediately shifted along the negative x direction a distance ΔR_0 to induce particle number flow at $\tau > 0$. The total pulse sequence is then: $\mathbf{R}_0(\tau) = 0$ for $\tau \leq 0$ and $\mathbf{R}_0(\tau) = -|\Delta R_0|\hat{x}$ for $\tau > 0$. By expanding the squared term in μ_i we see that the trap shift can be thought of as an applied linear potential: $\sim 2\Omega \mathbf{R}_i \cdot \hat{x}(\Delta R_0)$.

ϵ_i denotes a random energy shift at the ith site. In our study, the disorder is uniformly distributed with $\epsilon_i \in \{-\Delta, \Delta\}$. Specifically, we use the box probability distribution function:

$$P(\epsilon) = \frac{\Theta\left(\Delta - |\epsilon|\right)}{2\Delta}, \tag{4.3}$$

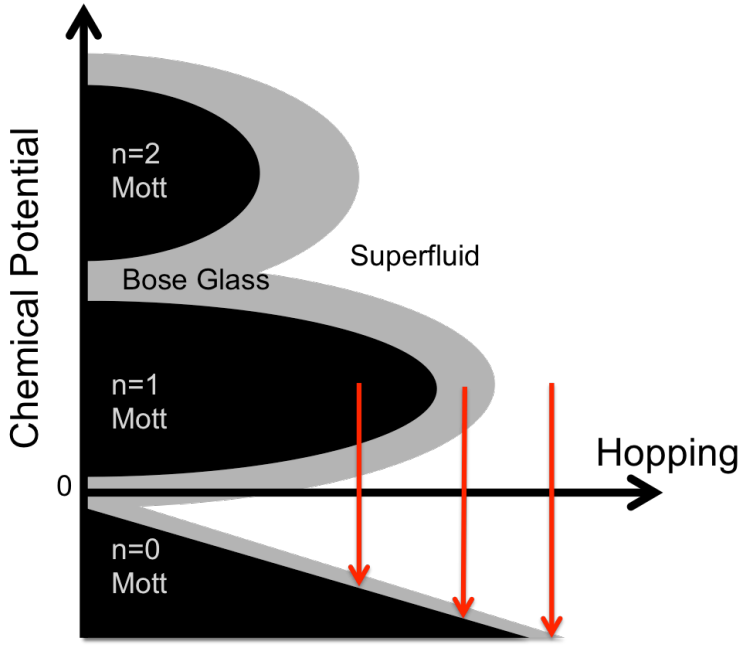

Figure 4.2: Schematic mean field phase diagram of the disordered Bose-Hubbard model [Eq. (4.1)] in the absence of a trap, $\Omega = 0$. The black regions indicate the incompressible Mott insulators found at integer densities. The grey regions indicate the compressible Bose-glass that separates the Mott from the superfluid. The three vertical arrows depict how the trapping potential lowers the local chemical potential as we move from the center of the system (top of the arrow) to the edge (bottom of the arrow). The three arrows represent regimes studied here, where the center of the system contains a: disordered Mott insulator (left), Bose-glass (center), and disordered superfluid (right).

where Δ is the strength of the disorder and Θ is the Heaviside step function.

To study the dynamics we use a stochastic mean field decoupling performed using variational wavefunctions: the time-dependent Gutzwiller ansatz [89, 118, 119]. The ansatz yields wavefunctions whose static expectation values agree very well with quantum Monte Carlo away from phase boundaries in 2D in 3D (see, e.g., Refs. [87] and [88]). The wavefunction at time τ is assumed to be in the product form:

$$|\Psi_{\mathrm{GW}}(\tau)\rangle = \prod_i \left[\sum_{n=0}^{\infty} f_n^{(i)}(\tau) |n\rangle_i \right], \tag{4.4}$$

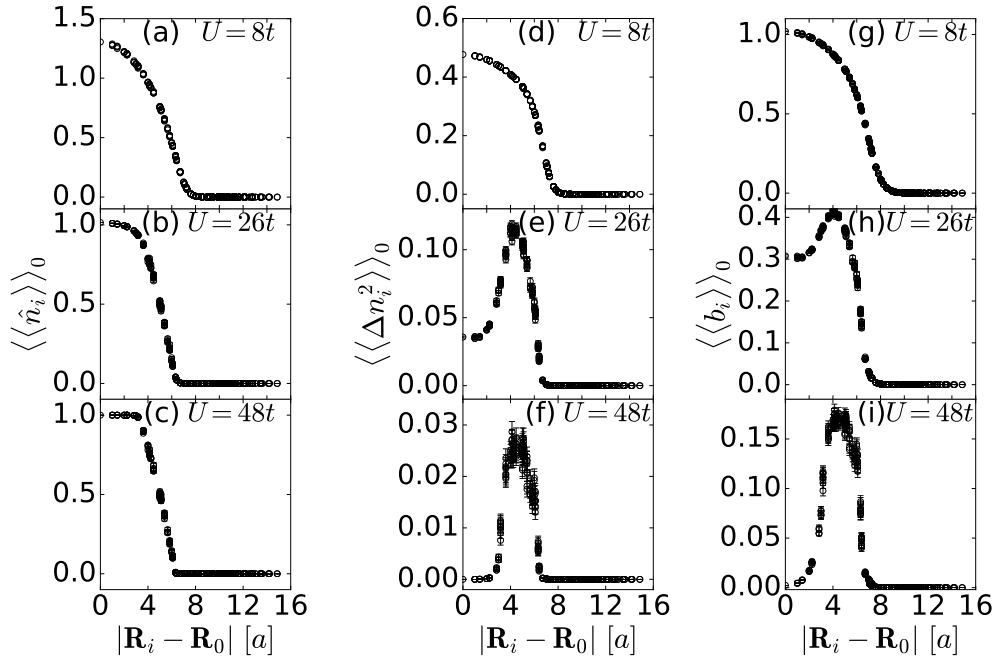

Figure 4.3: Panels (a)-(c) plot the disorder averaged local density in the initial state as a function of distance from the center of the trap. Panels (a) and (c) have a superfluid and Mott insulator in the trap center, respectively. Panel (b) is in an intermediate regime. Model parameters are chosen to be: disorder strength $\Delta = 0.3U$, trap strength $\Omega = 0.02U$, and central chemical potential $\mu = 0.5U$. Panels (d)-(f) plot the same but for the disorder averaged local density fluctuations in the initial state. The density fluctuations in panels (e) and (f) show the edge superfluid. Panels (g)-(i) plot the disorder averaged local superfluid order parameter in the initial state. Error bars result from disorder averaging.

where $f_n^{(i)}(\tau)$ is the complex amplitude to find n atoms on lattice site i at time τ.

The initial state can be found using the variational theorem. We first assume a random initial guess for all of the f's. We then minimize the energy of H by varying all f's using a conjugate gradient method. We find that keeping the parameters f_n for $n \leq 4$ is sufficient for the regime studied here. Once the wavefunction is found, all initial state correlation functions can be computed.

We propagate the initial state wavefunction in time using the equations of motion consistent

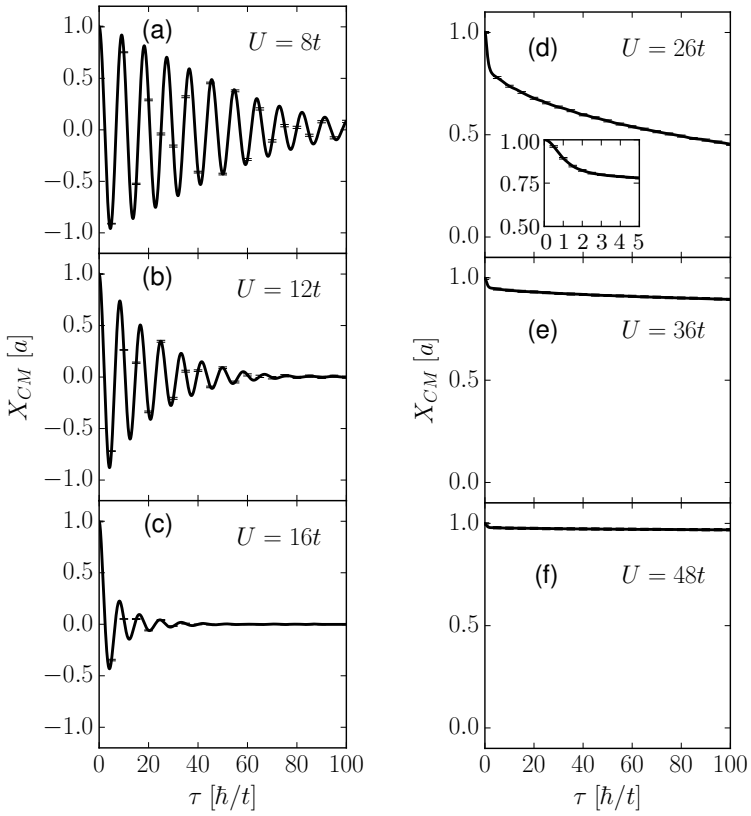

Figure 4.4: The disorder averaged center of mass position along the x-direction plotted as function of time for various interaction strengths, U. The trap shift is chosen to be $\Delta R_0 = a$ and other model parameters are the same as Fig. 4.3. Panels (a)-(c) are initially in the disordered superfluid state. In panel (d) the center of the system is initially in the Bose-glass state whereas panel (f) is initially in the Mott state. The inset to panel (d) shows the short-time behavior. Panel (e) is initially in an intermediate state. In panels (d)-(f), the center of mass has a nearly constant velocity for $\tau \gg \hbar/t$.

with the Gutzwiller ansatz. The equations of motion for $f_n^{(i)}$ are [89]:

$$\begin{aligned} \mathrm{i}\hbar\partial_\tau f_n^{(i)} &= \left[\frac{U}{2}n(n-1) + n\mu_i\right] f_n^{(i)} \\ &- t\sum_{\langle i,j\rangle}\left(\psi_j^*\sqrt{n+1}f_{n+1}^{(i)} + \psi_j\sqrt{n}f_{n-1}^{(i)}\right), \end{aligned} \tag{4.5}$$

where $\psi_j = \langle b_j\rangle = \sum_n \sqrt{n} f_{n-1}^{(j)*} f_n^{(j)}$ is the mean-field superfluid order parameter. We numerically solve this set of coupled first order differential equations using the adaptive step size

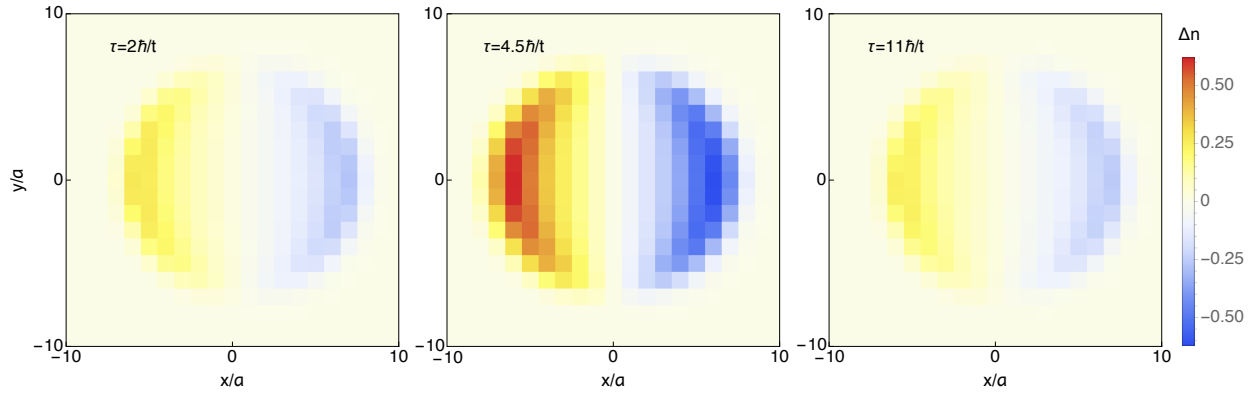

Figure 4.5: The disorder averaged local density deviation from the initial state, $\Delta n_i \equiv \langle\langle n_i\rangle\rangle_\tau - \langle\langle n_i\rangle\rangle_{\tau=0}$, plotted as a function of position in the $x-y$ plane for three different times. All model parameters are the same as Fig. 4.4a where a superfluid occupies nearly the entire trap. These parameters correspond to the right arrow in the phase diagram, Fig. 4.2. Here we see how the superfluid as a whole oscillates in the trap even in the presence of disorder.

Runge-Kutta method. This allows access to all correlation functions as a function of time.

The center of mass position and velocity are key observables often used in experiments to reveal insulating behavior. We compute the total center of mass position along the x-direction and the center of mass velocity as a function of time:

$$\begin{aligned} X_{\rm CM}(\tau) &= \frac{1}{N}\sum_i \langle\langle \hat{n}_i\rangle\rangle_\tau [\hat{x}\cdot\mathbf{R}_i], \\ V_{\rm CM}(\tau) &= \frac{d}{d\tau} X_{\rm CM}(\tau). \end{aligned} \tag{4.6}$$

Here N is the number of particles and $\langle\langle ...\rangle\rangle_\tau$ indicates the disorder average of quantum state averages with respect to $|\Psi_{\rm GW}(\tau)\rangle$. We find that disorder averaging with 1000 configurations is sufficient to obtain convergence.

4.3 Static Properties

In this section we review the static properties of the disordered Bose-Hubbard model at zero temperature. The schematic mean field phase diagram [7] reproduced by the Gutzwiller ansatz [120] is depicted in Fig. 4.2. Here we see that the Mott insulator is separated from the superfluid by an intermediate Bose-glass. The Mott insulator occurs at integer filling and is incompressible. It has zero condensate fraction. The Bose-glass is compressible but has non-zero local condensate fraction due to superfluid puddles embedded in an insulating background. The superfluid is characterized by a non-zero stiffness [121] and compressibility.

The trapping potential lowers the chemical potential in moving from the center to the edge of the trap. The trap can (at a mean field level) be thought of as sweeping the chemical potential vertically through the phase diagram. The vertical arrows in Fig. 4.2 depict the three regimes of the trapped disordered Bose-Hubbard model studied in this chapter. The left, central, and right arrows indicate parameters such that the central region of the trap (the top of the arrow) hosts a disordered Mott insulator, Bose-glass, and disordered superfluid, respectively. Due to the inhomogeneous trapping potential, superfluid and Bose-glass coexist in the edge of the trap in all three regimes.

To characterize the phases in the trap we compute local correlation functions. Figs. 4.3a-c plot the local density as a function of distance from the trap center. The density qualitatively reveals the location on the phase diagram, with $\langle \hat{n} \rangle \approx 1$ indicating the Mott insulator. The local density fluctuations:

$$\langle \Delta n_i^2 \rangle \equiv \langle \hat{n}_i^2 \rangle - \langle \hat{n}_i \rangle^2, \tag{4.7}$$

capture the local compressibility since: $\langle \Delta n_i^2 \rangle \propto \kappa_i k_B T$, where T is temperature and local compressibility is $\kappa_i = \partial \langle \hat{n}_i \rangle / \partial \mu$. Figs. 4.3d-f plot the density fluctuations as a function

of distance from the trap center. The sharp increase of the fluctuations at the edge (in Figs. 4.3e and 4.3f) indicate compressible edge states. We have also used the local superfluid order parameter (in Figs. 4.3g-i) and other correlation functions to identify the location on the phase diagram.

4.4 Center of Mass Dynamics

This section presents our primary results by correlating center of mass dynamics with phases in the center of the trap. We find that even with moderately strong disorder, the superfluid phase oscillates. Strong interaction significantly damps superfluid motion. But when the center of the trap enters the Bose-glass and Mott phases, the center of mass dynamics slows considerably. By computing the density in the lattice we find that the center of the system fails to move. Here the dynamics is dominated by flow along the edges.

4.4.1 Superfluid Dynamics

We start with the center of mass dynamics of the superfluid (see the right vertical arrow in Fig. 4.2). Figs. 4.4a-c show damped oscillations of the superfluid in the presence of disorder. For large interaction strengths the superfluid quickly relaxes to sit at the trap center, Fig. 4.4c. Here the interplay of interactions and disorder dephase the initial state to effectively relax the system to the ground state of the new trap position. This is in contrast to the motion of a non-interacting condensate in a trap where revival occurs at the time scale of inverse trap frequency [122, 123]. Fig. 4.5 plots the local density at three different times to demonstrate the center of mass oscillations of the superfluid.

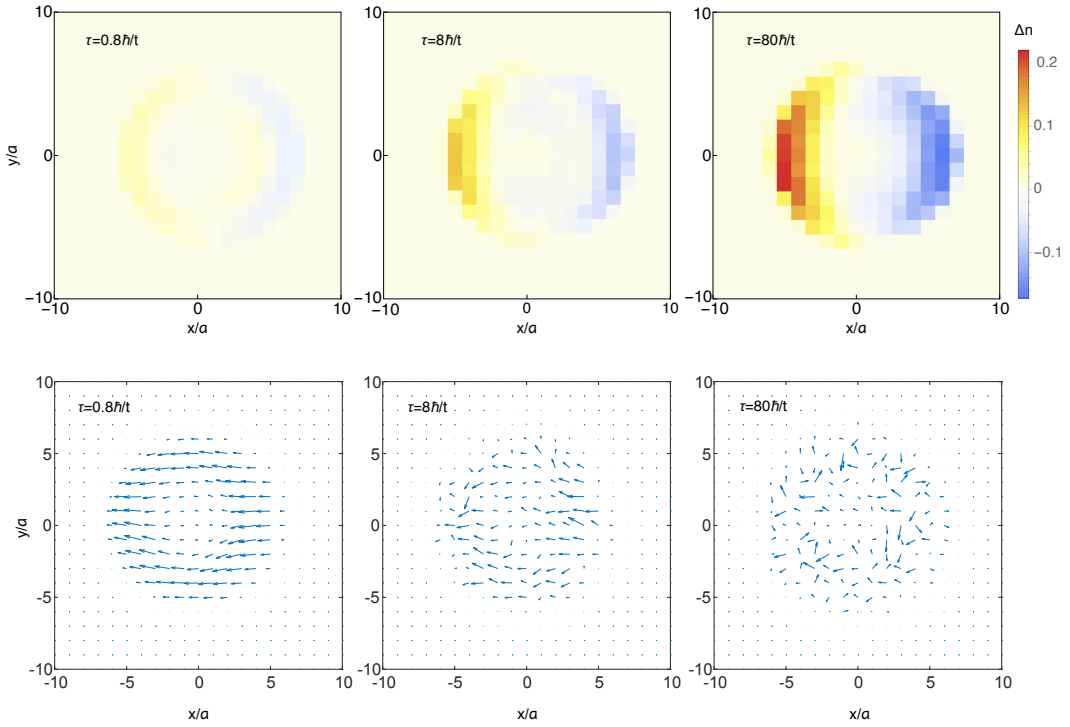

Figure 4.6: Top panel: the same as Fig. 4.5 but for an interaction strength of $U = 26t$ (parameters of Fig. 4.4d) which corresponds to a Bose-glass in the center of the trap (central arrow in Fig. 4.2). Bottom panel: the disorder averaged local current flow with the same parameters in the top panel. At $\tau = 0.8\hbar/t$ we see the first mechanism of transport where at short times the edge state quickly slips around the central insulator, depicted in the left panel of Fig. 4.1. At $\tau = 8\hbar/t$ and $80\hbar/t$ we see a different, two-step mechanism of transport, depicted in the right panel of Fig. 4.1. Here the particles first slowly tunnel out of the central insulator to, in the second step, get pushed quickly along the edges. In the two right snapshots, lateral tunneling events and a shrinking of the central insulator can be seen.

4.4.2 Short-Time Insulator Dynamics

We now turn to the center of mass trap dynamics in regimes where either the Bose-glass or Mott insulator lies in the center of the trap (see the left two vertical arrows in Fig. 4.2). The state propagated in Fig. 4.4d has a Bose-glass in the center while Fig. 4.4f has a Mott insulator. Fig. 4.4e shows an intermediate regime on the border of the Mott/Bose-glass transition. On short time scales, the Bose-glass and Mott states should display insulating

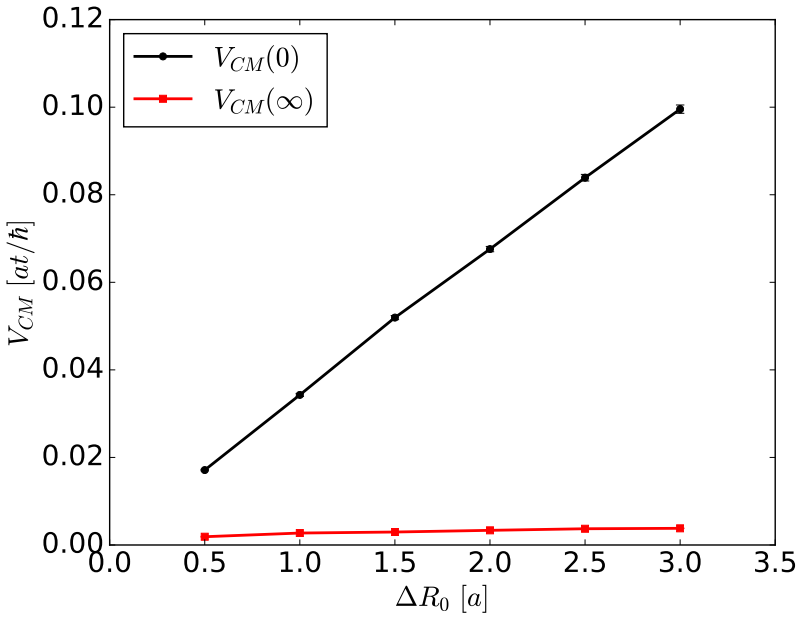

Figure 4.7: The disordered averaged center of mass velocity at short times [Eq. (4.9)] and long times [Eq. (4.10)] plotted as a function of the trap shift for an interaction strength of $U = 26t$. For short times, the center of mass velocity responds linearly to the length of the trap shift. For long times, the center of mass velocity barely change with the trap shift.

behavior because they are both locally gapped.

Figs. 4.4d-f show two distinct regimes: short times ($\tau \lesssim \hbar/t$) and long times ($\tau \gg \hbar/t$). At short times the center of mass quickly slips to a new value. Here the initial slip is most prominent in the Bose-glass regime, Fig. 4.4d. The next section will discuss the long-time dynamics.

To study the motion of the particles with an insulator in the center, we compute

$$I_j^\alpha = -\mathrm{i}\left(\langle b_j\rangle^*\langle b_{j+\hat{e}_\alpha}\rangle - \langle b_{j+\hat{e}_\alpha}\rangle^*\langle b_j\rangle\right), \tag{4.8}$$

which is the local current [124] flowing from the site j to the site $j + \hat{e}_\alpha$. By plotting the local current distribution in the trap, we can see how the particles move at certain times. The left panels of Fig. 4.6 shows the density and local current for $U = 26t$ (the Bose-glass

regime) after a very short time, respectively. Here we see that at short times the density flows in a ring around the edge.

To study the response of the center of mass velocity under an applied field at short times, we compute the initial center of mass velocity

$$V_{\mathrm{CM}}(0) \equiv \lim_{\tau \to 0} \frac{1}{\tau} \int_0^\tau d\tau' V_{\mathrm{CM}}(\tau'). \tag{4.9}$$

In the numerical calculation, we choose $\tau = 0.2\hbar/t$ to compute the initial velocity. Fig. 4.7 shows that the initial center of mass velocity responds linearly to the applied force.

The redistribution of the initial edge density corresponds to motion of the edge superfluid at velocities consistent with the band motion of individual edge particles. The left panel of Fig. 4.1 depicts short-time edge flow. We verify that the times required for edge particles to move a distance on the order of the cloud size are consistent with our simulations. If we consider a one-dimensional approximation to the edge state, the tight-binding energy of a single particle is $-2t\cos(ka)$ where k is the lattice wavevector. The semi-classical equation of motion under a applied field is $\hbar \mathrm{d}k/\mathrm{d}\tau = \Delta R_0 \Omega$. For short times, the velocity of the particle is then $2t\Delta R_0 \Omega \tau/\hbar^2$, which is linear in the applied field. The $U = 26t$ insulator extends 4 lattice sites in the trap with trapping potential $\Omega = 0.02U$. The total time for the edge particle to travel the length of the system under the trap shift $\Delta R_0 = a$ is then $2.77\hbar/t$, consistent with the result from our numerical simulations, $\approx 2.5\hbar/t$.

Our results show that the initial dynamics of trapped insulators reflect the motion of edge states. The edge moves quickly, on time scales consistent with the motion of free particles. For short times, the center of mass velocity responds linearly to an applied potential. We now turn to the long-time regime.

4.4.3 Long-Time Insulator Dynamics

After the initial slip we find a regime of *constant center of mass velocity* at long times, $\tau \gg \hbar/t$ (Figs. 4.4d-f). A naive expectation would be that the constant velocity is established by a slow drift of the center of mass as a whole where the disorder strength sets a scattering rate. We find that the this picture is not correct. Fig. 4.8a shows that the long-time center of mass velocity does not change with the application of a linear potential and is therefore terminal (recall that the trap shift, ΔR_0, effectively applies a linear potential). This behavior contrasts with behavior expected from a Drude-type model of transport where the center of mass as a whole would respond linearly to a weak potential.

To better understand the mechanism behind the terminal velocity at long times we study the density as a function of time. The density in the trap plotted for several different times (the two right panels in Fig. 4.6) reveals a two step process for long-time edge flow (right panel of Fig. 4.1). First, a particle tunnels out of the center to the edge at a rate determined by the competition between the local gap in the center and the trapping potential. In the second stage, the particle quickly moves along the edge to redistribute the center of mass. Repeated tunneling out of the center followed by flow along the edge then results in a center of mass shift. Slow tunneling into the edge allows edge flow at long times and therefore dictates the time scale for center of mass motion.

To verify the two-step picture we construct a simple model to estimate the velocity at long times. Sec. 4.5 uses a two-site model to show that in the absence of disorder the tunneling rate out of the center only depends on the trapping frequency, tunneling, and interaction strength. The velocity in our two-site model is therefore independent of the trap shift. We also find that the velocity expected from our two-site model compares well with our simulations.

The two-step picture and our simple model do suggest that the center of mass velocity should depend on U. Fig. 4.8b shows that the long-time center of mass velocity varies with U. Here stronger U suppresses tunneling out of the bulk because the trap must compensate with high edge energies to confine the system. We have checked that the U dependence of the two-site model is consistent with our simulation.

We now discuss the long-time center of mass velocity as a direct measure of insulating behavior in the trap [125]. We compute:

$$V_{\mathrm{CM}}(\infty) \equiv \lim_{\tau\to\infty} \frac{1}{\tau} \int_{\tau_0}^{\tau} d\tau' V_{\mathrm{CM}}(\tau'), \tag{4.10}$$

where the limit $\tau \to \infty$ is understood to imply a long time average such that the insulating states do not reach the center of the trap. We choose $\tau_0 = 20\hbar/t$ to include only long-times by avoiding integration over the short-time dynamics. We expect that $V_{\mathrm{CM}}(\infty)$ should vanish for both immobile states and for states that oscillate about the trap center because there is no net center of mass velocity for an oscillating state.

Fig. 4.9 plots the long-time center of mass velocity in the trap as a function of U. Varying U allows access to the superfluid, Bose-glass, and Mott phases. We find that $V_{\mathrm{CM}}(\infty)$ is zero in the superfluid phase because the superfluid oscillates in the trap. But at long times the center of mass performs a slow drift in insulating phases to lead to a non-zero $V_{\mathrm{CM}}(\infty)$. The Bose-glass phase shows the largest velocity because the tunneling out of the bulk into the edge is the fastest here. But the large U Mott limit restricts tunneling into the edge to eventually stop center of mass motion.

The long time center of mass velocity responds to disorder and trapping. We have checked that the center of mass velocity in the insulating phases is suppressed by increasing disorder or trapping frequency. Here strong disorder and trapping impact both processes depicted in

the right panel of Fig. 4.1. They suppress tunneling out of the center into the edge while also restricting flow along the edge.

4.5 Two-site Tunneling Time

In this section we model the tunneling out of an insulating state at the trap center and into an edge state using a two-site effective model. Fig. 4.10 shows part of a Mott insulator along one direction in the lattice. The curved line depicts the trapping potential which eventually zeroes the edge density. The trapping potential energy must be on the order of the interaction energy to zero the density.

We consider a two-site tunneling model Hamiltonian,

$$H_2 = -t\left(b_1^\dagger b_2 + b_2^\dagger b_1\right) + V b_2^\dagger b_2, \tag{4.11}$$

where V is the relative energy gap between the two sites. V is a fitting parameter on the order of the Mott gap.

Solving the Schrödinger equation, we obtain the population on site 2,

$$n_2 = \frac{2t^2}{4t^2+V^2}\left\{\cos\left[\sqrt{4t^2+V^2}(\tau/\hbar)\right]-1\right\}. \tag{4.12}$$

The tunneling rate from site 1 to site 2 can then be defined as,

$$\Gamma = \max_\tau \frac{dn_2}{d\tau} = \frac{2t^2}{\hbar\sqrt{4t^2+V^2}}. \tag{4.13}$$

Γ gives correct limits: $\Gamma \to t$ for $V \to 0$ and $\Gamma \to 0$ for $V \to \infty$.

Using Γ as an estimate for the tunneling rate out of the central insulator we can estimate the order of magnitude of the center of mass velocity. Once the particle tunnels out of the center it then travels along the edge a distance l. The center of mass velocity in this approximation becomes:

$$v = \frac{\Gamma l}{N} = \frac{2t^2 l}{N\hbar\sqrt{4t^2 + V^2}}, \tag{4.14}$$

where N is the total particle number in the trap. To compare this estimate with the our simulations we substitute appropriate parameters. The fitting parameter of the gap V is chosen to be the Mott gap U. Fig. 4.11 shows that the results obtained from the two-site model are of the same order of magnitude as simulations.

4.6 Summary

We have studied the zero temperature trap dynamics of states prepared in a disordered Bose-Hubbard model. We have computed the center of mass velocity of a disordered superfluid, a disordered Mott insulator, and a Bose-glass using Gutzwiller mean field theory. While the superfluid exhibits damped oscillations for strong interaction strengths, the other two states are essentially motionless insulators at the trap center.

We find that the center of mass velocity of trapped insulators is dominated by the flow of edge states. We also find two time scales for the trapped insulators. At short time scales the edge superfluid flows around the insulating bulk to move the center of mass. But at longer time scales, tunneling out of the bulk to the edge establishes a slow drift of the center of mass.

Our results can be used to identify insulating states in trapped optical lattices. We find

that, at long times, the edge flow around the Bose-glass can lead to center of mass velocities that are much larger than in the Mott. We have studied parameter regimes that are similar to what has been explored in experiments. In Ref. [37], for example, experiments were done using a speckle disorder potential applied to ^{87}Rb atoms in a cubic optical lattice. Here the Hubbard parameters were: $t/U \sim 0.005 - 0.3$ and the trapping potential keeps the density near 1.4 at the trap center. The speckle disorder leads, most prominently, to an exponentially distributed onsite disorder potential in μ_i [126] which differs from our study. But finite temperature effects should lead to the most important difference between our study and previous experiments. Our results have so far excluded finite temperature effects while experiments [37] have been done in the regime $k_{\mathrm{B}}T \sim 3t$.

As a next step we will include non-zero temperatures in the initial state. We expect that for very low temperatures, $k_{\mathrm{B}}T \ll t$, our $T = 0$ results will be qualitatively similar. But for intermediate temperatures, $t \lesssim k_{\mathrm{B}}T < U$, thermally assisted tunneling out of the central insulators and into the edge will significantly enhance the center of mass velocity. Our results therefore offer a lower bound on the center of mass velocity.

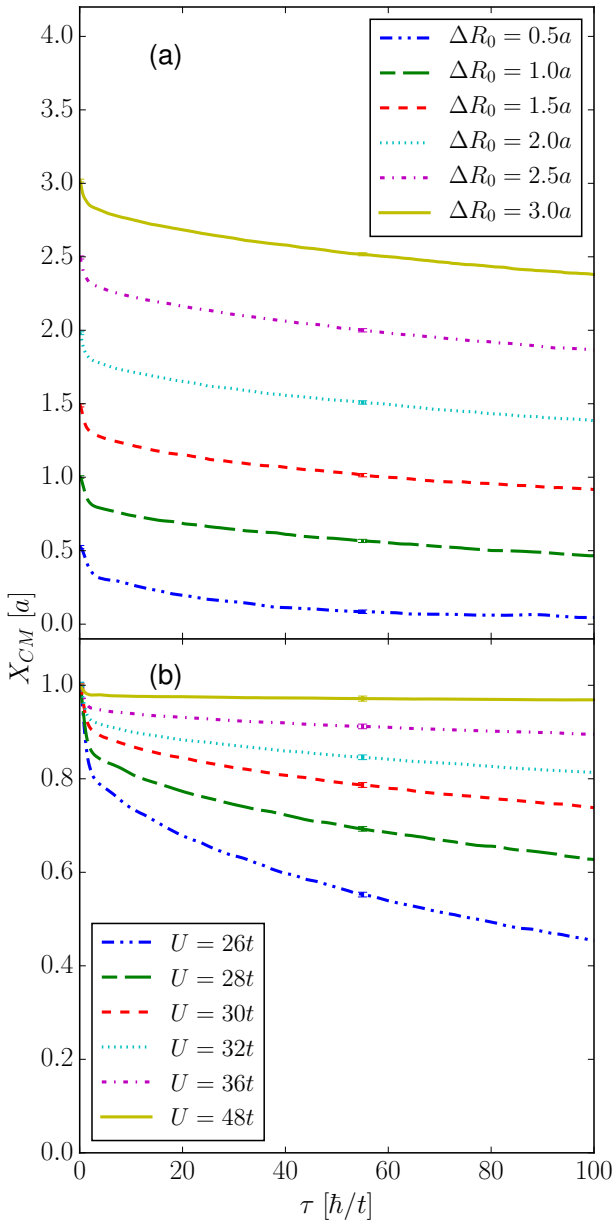

Figure 4.8: The disorder averaged center of mass position plotted as a function of time for: (a) several different trap shifts for $U = 26$ and (b) several different U for $\Delta R_0 = a$. The model parameters are otherwise the same as Fig. 4.3. In panel (a) we see that different trap shifts do not change the long time center of mass velocity (the slope is nearly constant). But in panel (b) we see that the slope depends on U.

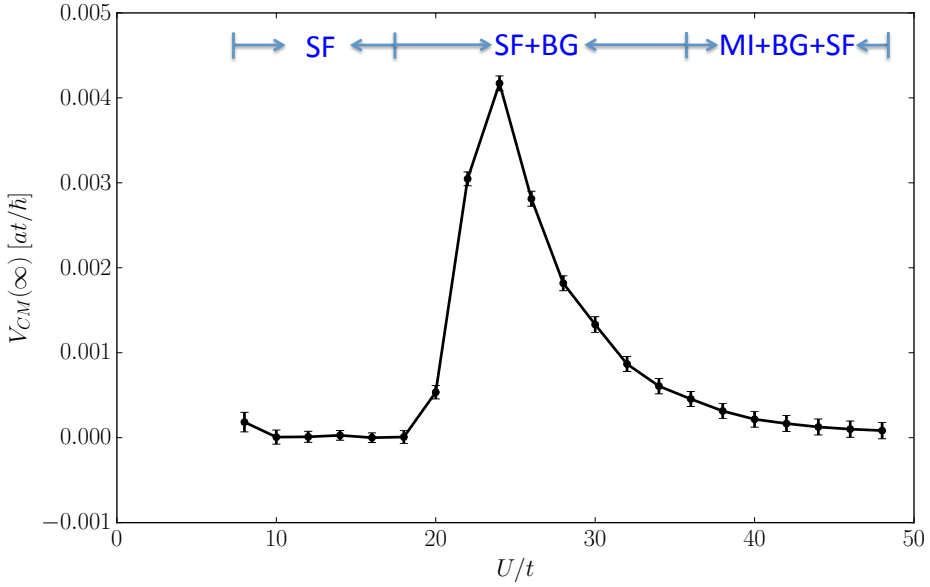

Figure 4.9: The disorder averaged center of mass velocity at long times [Eq. (4.10)] plotted as a function of interaction strength. For weak interactions the entire system is in the superfluid (SF) phase and frequent center of mass oscillations results in a zero net velocity. For intermediate interaction strengths the Bose-glass (BG) lies in the trap center. Here the two-step edge flow mechanism depicted in the right panel of Fig. 4.1 allows a small but finite center of mass velocity. At large interaction strengths the center of the system is in the Mott regime (MI) where tunneling into the edge (and therefore the center of mass velocity) is strongly suppressed.

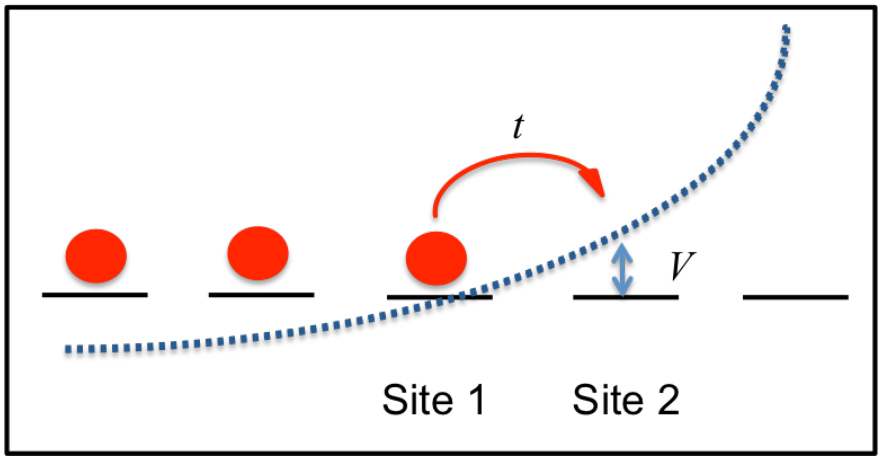

Figure 4.10: Schematic showing sites of a lattice (dashes) along one direction filled up to site 1 with particles. Site 2 is an empty edge site. Tunneling from site 1 to site 2 is controlled with a potential, V, at site 2. The dotted line depicts the parabolic trapping potential which zeroes the edge density.

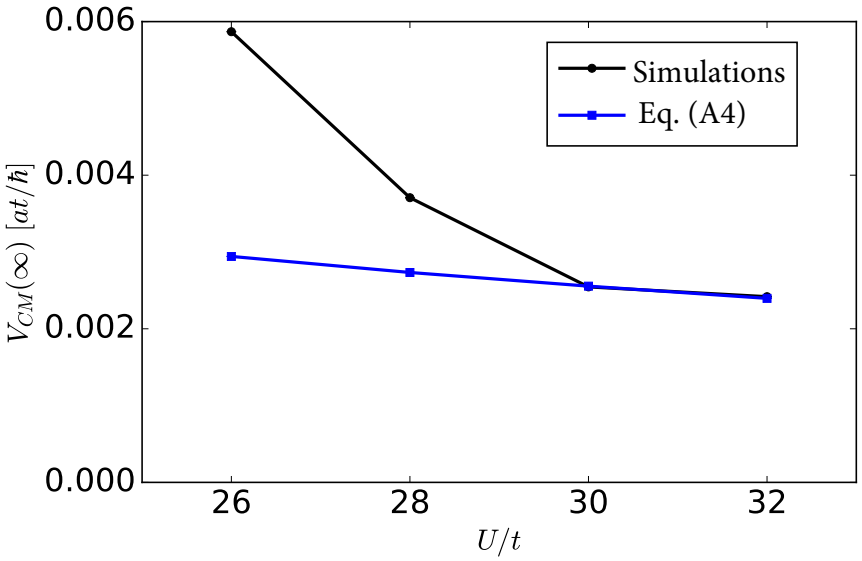

Figure 4.11: The comparison of the center of mass velocity at long times between the estimate of the two-site model and numerical simulations for various interaction strength.

Chapter 5

Equilibration Dynamics of Strongly Interacting Bosons in 2D Lattices with Disorder

The work described in this chapter was published as:

Mi Yan, Hoi-Yin Hui, M. Rigol, and V. W. Scarola, "Equilibration Dynamics of Strongly Interacting Bosons in 2D Lattices with Disorder," *Phys. Rev. Lett.*, **119**, 073002 (2017) [76].

I contributed all the calculations and visualizations in this paper under Professor Vito Scarola's supervision. All authors analyzed and discussed the results and contributed in writing the manuscript.

5.1 Introduction

. Ultracold atoms loaded into optical lattices [127–129] offer ideal platforms to study localization [42, 43]. Examples in the noninteracting limit include fermionic band insulators [44], and, in the presence of (quasi-)disorder, Anderson insulators [29, 30, 45–48]. In clean

systems, localization can also occur because of interactions, producing Mott insulators (MIs) [6, 18, 130–132]. Recent experimental studies have explored the interplay between disorder and interactions [31, 36, 37, 39, 56, 133–138]. In the ground state of bosonic systems, this interplay can generate the Bose-glass (BG) phase [7, 139]. The BG, like the bosonic MI, is characterized by a vanishing superfluid density but, unlike the MI, it is compressible. At extensive energy densities above the ground state, the interplay between disorder and interactions can lead to a remarkable phenomenon known as many-body localization (MBL) [49–51]. In the MBL phase, eigenstate thermalization [52–54] does not occur [55].

Signatures of MBL were recently observed with fermions [137, 138] and bosons in two dimensions (2D) [56]. Our work is motivated by the latter experiment (see Refs. [117, 140] for theoretical studies inspired by the former). In Ref. [56], a MI with one boson per site was prepared in a harmonic trap in a deep optical lattice. All bosons in one half of the system were then removed and the remaining half was allowed to evolve by lowering the lattice depth, with or without disorder. During the dynamics, the parity-projected occupation of the lattice sites was measured using fluorescence imaging, allowing the study of the evolution of the imbalance $\mathcal{I}$ between the initially occupied and unoccupied halves. With no or weak disorder, $\mathcal{I}$ vanished within times accessible experimentally, i.e., it attained the value expected in thermal equilibrium. But beyond a certain disorder strength, $\mathcal{I}$ appeared to saturate to a nonzero value. This saturation was taken as evidence for MBL [56].

Features of the experimental setup in Ref. [56] can lead to a very slow equilibration of $\mathcal{I}$ to the point of making it difficult to distinguish glassy behavior from the MBL phase. First, the initial dynamics in the unoccupied half of the trap is dominated by Anderson physics (because of low site occupations). Second, the initial MI, before the removal of the bosons in one half of the system, is close in energy to the ground state after the lattice depth is lowered but the system remains deep in the MI regime. The latter MI, in turn, is close in

energy to a BG with a site occupancy slightly below one at the same interaction strength (if the disorder is strong enough to generate a BG). Therefore, the dynamics resulting from the gradual decrease of the site occupations in the occupied half of the system, after the removal of the bosons in the other half, can be dominated by excitations of the BG in the remaining half.

To study the impact of glassy physics we use Gutzwiller mean-field theory (GMFT) to model the dynamics of the experiments in Ref. [56]. GMFT provides qualitatively correct phase diagrams for strongly interacting clean [8, 118, 141, 142] and disordered [116, 120, 143–145] (away from the tip of the Mott lobe) systems. It has also been used to study non-equilibrium effects such as the dynamical generation of molecular condensates [89] and MIs [87], dipole oscillations [146], quantum quenches [116, 147, 148], expansion dynamics [88, 149], and transport in the presence of disorder [75, 116]. However, since the Gutzwiller ansatz wavefunction is a product state, it has zero entanglement entropy for any partitioning of the system. GMFT is therefore capable of capturing BG dynamics but it cannot capture thermalization and MBL phases [150], which after taken out of equilibrium, e.g., using a quantum quench, exhibit a linear [151] and logarithmic [152] growth of the entanglement entropy, respectively, with time.

We use GMFT to study the dynamics of initial states under the same (or similar) conditions as the experiment, thus allowing direct comparison. We find that the GMFT dynamics is similar but not quite the same as that in the experiment. In particular, the GMFT state rebalances more slowly, which motivates us to add a phenomenological parameter to our theory to gradually remove slow particles from data analysis because their dynamics are not accurately captured by our theory. A single phenomenological parameter significantly improves the agreement between theory and experiment.

Given the fact that GMFT cannot describe dynamics in a MBL phase, our results raise

concerns as to whether experimental observations are the result of MBL or the result of slow transport due to glassy dynamics. Only the latter is captured by our GMFT treatment.

5.2 Model

We consider bosons in a 2D square lattice subjected to disorder and a parabolic trapping potential, as described by the Bose-Hubbard Hamiltonian,

$$\hat{H} = -J \sum_{\langle \mathbf{ij} \rangle} \hat{b}_{\mathbf{i}}^{\dagger} \hat{b}_{\mathbf{j}} + \frac{U}{2} \sum_{\mathbf{i}} \hat{n}_{\mathbf{i}} \left(\hat{n}_{\mathbf{i}} - 1 \right) + \sum_{\mathbf{i}} \mu_{\mathbf{i}} \hat{n}_{\mathbf{i}}, \tag{5.1}$$

where $\hat{b}_{\mathbf{i}}^{\dagger}$ creates a boson at site $\mathbf{i} \equiv (i_x, i_y)$ and $\hat{n}_{\mathbf{i}} = \hat{b}_{\mathbf{i}}^{\dagger} \hat{b}_{\mathbf{i}}$ is the site occupation operator. J parametrizes the tunneling between nearest neighbors and U is the on-site repulsive interaction. The chemical potential (μ), harmonic trap (of strength Ω), and disorder potential ($\epsilon_{\mathbf{i}}$) are in $\mu_{\mathbf{i}} = -\mu + \Omega \left| \mathbf{i} - \mathbf{r}_0 \right|^2 + \epsilon_{\mathbf{i}}$, with $\mathbf{r}_0 = (0, 0)$. We focus on a lattice with 31×31 sites in which, for the Hamiltonian parameters used here, the sites at the edges are always empty. We consider two types of disorder, with uniform and Gaussian distributions, whose strengths are denoted by Δ_u and Δ_g, respectively. We set $k_B = \hbar = 1$.

5.3 Methods

—We study the dynamics of zero and nonzero temperature initial states. The density matrix within GMFT is

$$\hat{\rho}(t) = \prod_{\mathbf{i}} \hat{\rho}_{\mathbf{i}}(t) = \prod_{\mathbf{i}} \left[\sum_{m,n=0}^{\infty} \alpha_{mn}^{(\mathbf{i})}(t) \left| m \right\rangle_{\mathbf{ii}} \left\langle n \right| \right], \tag{5.2}$$

where $|n\rangle_{\mathbf{i}}$ is the state with n bosons at site $\mathbf{i}$, and t denotes time. This ansatz decouples Eq. ((5.1)) into single-site Hamiltonians $\hat{H}_{\mathbf{i}}^{\mathrm{MF}} = -J(\phi_{\mathbf{i}}^{*}\hat{b}_{\mathbf{i}} + \phi_{\mathbf{i}}\hat{b}_{\mathbf{i}}^{\dagger}) + (U/2)\sum_{\mathbf{i}} \hat{n}_{\mathbf{i}}(\hat{n}_{\mathbf{i}} - 1) + \mu_{\mathbf{i}}\hat{n}_{\mathbf{i}}$, where $\phi_{\mathbf{i}} = \sum_{\mathbf{j}\in \mathrm{nn}_{\mathbf{i}}} \mathrm{Tr}(\hat{\rho}_{\mathbf{j}}\hat{b}_{\mathbf{j}})$ sums over neighbor sites to $\mathbf{i}$. Substituting Eq. ((5.2)) into the von Neumann equation, $i\partial_t\hat{\rho} = [\hat{H}, \hat{\rho}]$, leads to the equation of motion for $\alpha_{mn}^{(\mathbf{i})}$:

$$\begin{aligned} i\partial_t \alpha_{m,n}^{(\mathbf{i})} = &- J\phi_{\mathbf{i}}^{*}\left[\sqrt{m+1}\alpha_{m+1,n}^{(\mathbf{i})} - \sqrt{n}\alpha_{m,n-1}^{(\mathbf{i})}\right] \\ &- J\phi_{\mathbf{i}}\left[\sqrt{m}\alpha_{m-1,n}^{(\mathbf{i})} - \sqrt{n+1}\alpha_{m,n+1}^{(\mathbf{i})}\right] \\ &+ \frac{U}{2}\left[m\left(m-1\right) - n\left(n-1\right)\right]\alpha_{m,n}^{(\mathbf{i})} \\ &+ \mu_{\mathbf{i}}\left(m-n\right)\alpha_{m,n}^{(\mathbf{i})}, \end{aligned} \tag{5.3}$$

which yields the time evolution of the site occupations: $n_{\mathbf{i}}(t) = \mathrm{Tr}(\hat{\rho}_{\mathbf{i}}\hat{n}_{\mathbf{i}})$.

Following Ref. [56], we quantify the degree of localization using the imbalance,

$$\mathcal{I}(t) = \frac{N_L(t) - N_R(t)}{N_L(t) + N_R(t)}, \tag{5.4}$$

where $N_L(t) = \sum_{-l_x \le i_x < i_0, |i_y| \le l_y} n_{i_x,i_y}(t)$ and $N_R(t) = \sum_{i_0 \le i_x \le l_x, |i_y| \le l_y} n_{i_x,i_y}(t)$, with an $l_x \times l_y$ central region of interest. l_y is taken to be 2 to define a window five lattice sites wide in the y direction. We first set l_x to $l_W = 9$, as in experiment. In Ref. [56], the lattice center does not always coincide with the center of the harmonic potential, and this causes an imperfect preparation of the initial state domain wall. To account for this, the line separating the left and right sides of the system is defined using $i_0 = 0$ or $i_0 = 1$. The imbalance is obtained by averaging the two cases.

We also compute the inverse decay length $\lambda(t)$ [56]. To calculate $\lambda(t)$ we first compute the

average, $\bar{n}_{i_x}(t) = (2l_y+1)^{-1}\sum_{|i_y|\leq l_y} n_{i_x,i_y}(t)$. λ is then obtained by fitting

$$\bar{n}_{i_x}(t)/\bar{n}^0_{i_x} \sim e^{-\lambda(t)\, i_x}, \tag{5.5}$$

where $\bar{n}^0_{i_x}$ is the zero disorder steady-state density and i_x denotes a least squares fit from $i_x = 0$ to l_x.

For $\hat{\rho}(t=0)$, we take the ground state or a thermal state of the initial Hamiltonian, such that $\hat{\rho}_{\mathbf{i}} = Z_{\mathbf{i}}^{-1} e^{-\beta \hat{H}^{\mathrm{MF}}_{\mathbf{i}}}$ (where $\beta = 1/T$ is the inverse temperature and $Z_{\mathbf{i}}$ is the partition function). Our calculations in the presence of disorder are done for an ensemble of disorder realizations. Disorder averaging over around 100 disorder realizations is sufficient for convergence.

Within GMFT, dynamics occur only when there are nonvanishing values of the order parameter $\phi_{\mathbf{i}}$ [see Eq. ((5.3))]. As a result, a pure MI state would exhibit no dynamics within GMFT. We find that, as in Refs. [75, 149], the small region with a non-vanishing order parameter generated by the harmonic trap at the edge of MI domains is sufficient to drive dynamics. Remarkably, we will see that the ensuing dynamics measured by imbalance is slower but similar to that in the experiments [56] at long times. We will then show that decreasing l_x to phenomenologically remove particles in the MI state significantly improves agreement with experiment.

5.4 Quenched Dynamics

In the experiment [56] the dynamics took place after lowering the lattice depth and introducing a disorder potential to a MI created in a deep lattice and to which all atoms in one half of the system were removed. From now on, we use the hopping parameter after the quench $J = U/24.4$ as our energy unit. To create the initial state, we used the experimental param-

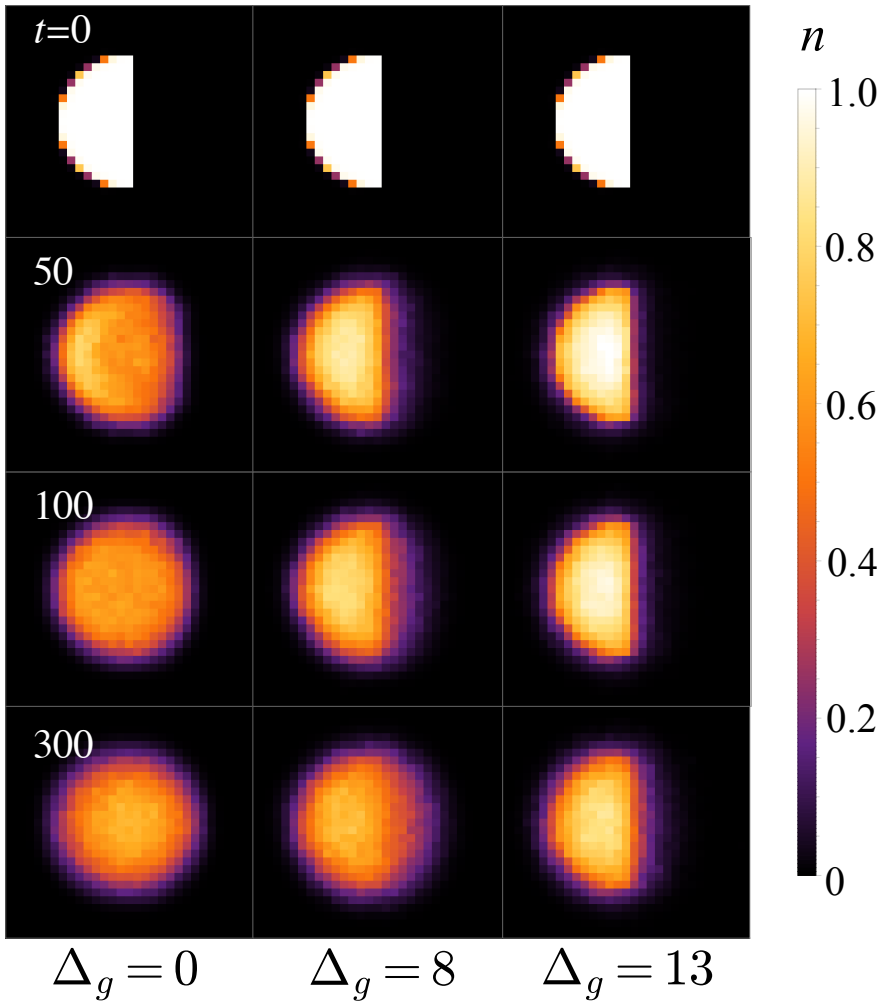

Figure 5.1: The site occupations for quenched dynamics at zero temperature. Columns (rows) depict results for different disorder strengths (different times). At time $t = 0$ all bosons in the right half of the system are removed and the remainder evolves for $t > 0$. The $t = 0$ state is the ground state for a very small hopping and no disorder. For $t > 0$, Gaussian disorder of strength Δ_g is introduced and the hopping is increased. The state evolves for $t \geq 0$ with no parameter changes.

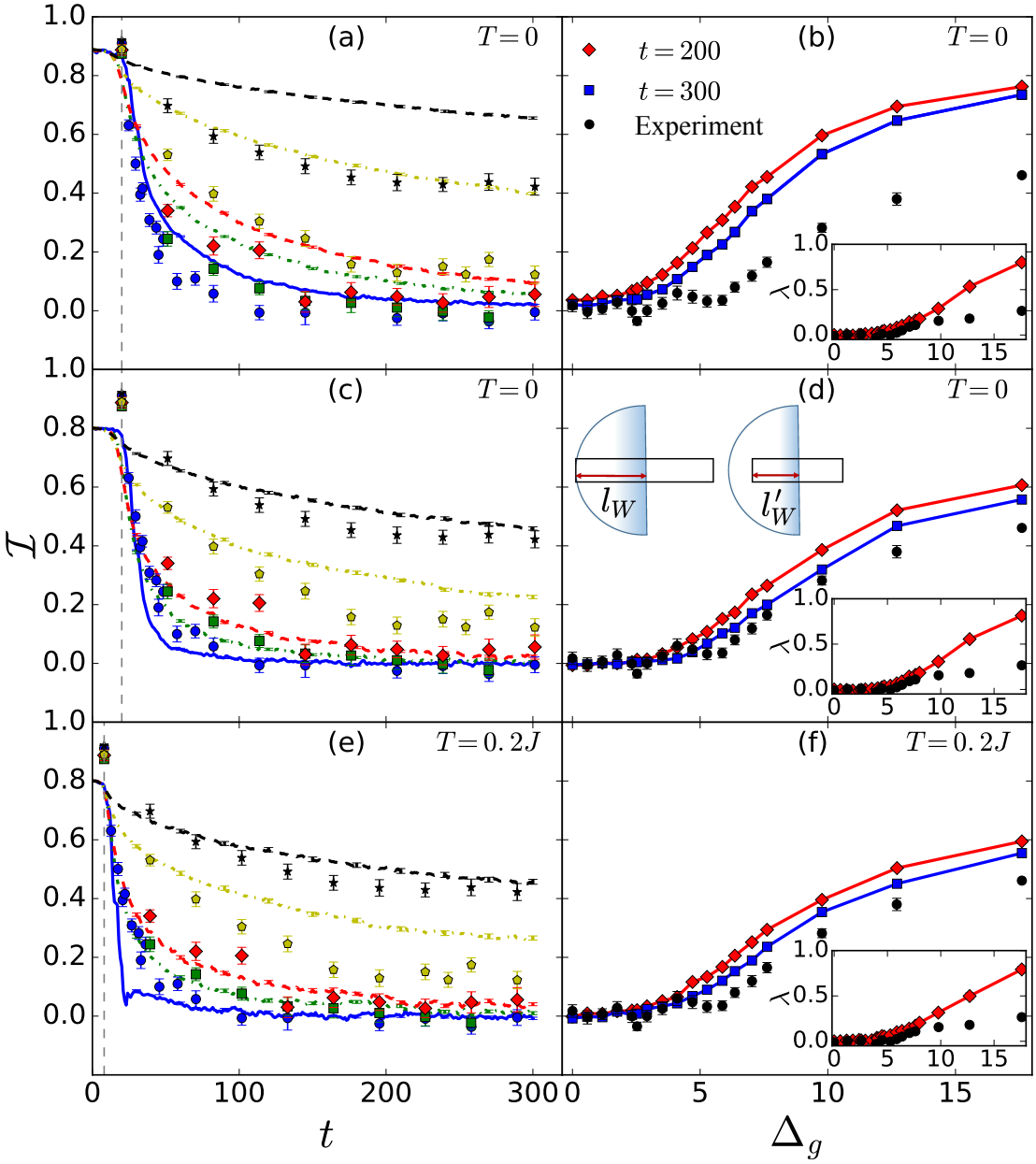

Figure 5.2: (a): Time evolution of the imbalance $\mathcal{I}$ for various disorder strengths at initial temperature $T = 0$. Lines show simulation results while points with error bars show experimental data [56]. The vertical dashed line marks a time $t^* = 20$ below which $\mathcal{I}$ barely changes within GMFT. The experimental results are shifted to start at t^*. From bottom to top the lines and symbols correspond to $\Delta_g = 0, 3, 4, 8$, and 13. (b): Corresponding $\mathcal{I}$ for the same parameters but at times $t = 200$ and 300 against disorder strength. The experimental result after an evolution time of 187 are also plotted. The inset shows the inverse decay length [Eq. (5.5)] from our calculation at $t = 200$ and for the experiment after an evolution time $t = 187$. (c) and (d): The same as (a) and (b) but with an analysis window resized from $l_W = 9$ [as in (a) and (b) following Ref. [56]] to $l'_W = 5$, as shown in the schematic. (e) and (f): The same as (c) and (d) but at non-zero temperature. Here t^* reduces to 8.

eters [56]: $J_I = 0.244$, $U = 24.4$, $\Omega = 0.145$, and $\mu = 10.6$. After free energy minimization, particles on the right half of the system are manually removed [by setting $\alpha_{m,n}^{(i_x>0)} = \delta_{m,0}\delta_{n,0}$ in Eq. (5.2)], leaving behind a particle number comparable with the experiment, $N_b \approx 123$. In accordance with the experimental protocol [56], to generate disorder (at the evolution stage) we square a two-dimensional array of uniformly distributed random numbers followed by a convolution with a Gaussian profile of standard deviation 0.5. The disorder strength Δ_g is defined as the full width at half maximum of the resulting disorder profile.

The first column in Fig. 5.1 depicts the evolution of the site occupations in the absence of disorder. Here the particles expand to reach a steady state with no imbalance. When disorder of strength $\Delta_g = 8$ is introduced, the motion slows considerably and an imbalance remains at the latest time shown. For very strong disorder ($\Delta_g = 13$), the particles remain almost entirely in the initially occupied region.

To quantitatively understand the dynamics, we plot the imbalance against time in Fig. 5.2(a). For $t < t^*$, the imbalance barely changes. This is an artifact of GMFT for the initial state, which is mostly a MI domain. Beyond t^*, $\mathcal{I}$ vanishes rapidly in the clean limit and for weak disorder. But, as the disorder strength increases, it takes longer for $\mathcal{I}$ to reach the expected $\mathcal{I} = 0$ steady state value. In Fig. 5.2(a), we also plot the experimental results taking t^* to be the starting time for the experiments. The GMFT and experimental results exhibit good agreement for weak disorder strength, but the latter exhibit faster relaxation as the disorder strength is increased.

In Fig. 5.2(b), we plot the imbalance alongside experimental results [56], as a function of the disorder strength. In our theoretical results, the upturn in $\mathcal{I}$ versus Δ_g moves toward stronger disorder strengths as t increases. A similar trend was seen in experiments for $t \lesssim 200$, but the experimental results appeared to saturate for $200 \lesssim t \lesssim 300$. For any given selected time, the upturn in $\mathcal{I}$ versus Δ_g occurs at a smaller value of Δ_g in GMFT when compared to the

experiments, which is expected given the slower dynamics of the former seen in Fig. 5.2(a).

λ offers another way to quantify the degree of localization by parameterizing the extent to which disorder suppresses the relaxation of site occupations. The inset in Fig. 5.2(b) shows λ versus Δ_g for $t = 200$ and the experimental results for $t = 187$. The behavior of λ (inset) is similar to that of $\mathcal{I}$ (main panel).

There are also differences between GMFT and experiments. For example, at weak disorder strengths, the experimental data of Fig. 5.2(b) exhibits oscillations not captured by GMFT. These oscillations in turn impact the comparison of the nature of upturns of $\mathcal{I}$ or λ near $\Delta_g = 5.5$, as they make it look sharper in the experimental results.

A key observable in identifying localization is the time derivative of the imbalance, $\dot{\mathcal{I}}$, at long times, as used in observations of Anderson localization with ultracold atoms [29, 30, 45–48]. The vanishing of $\dot{\mathcal{I}}$ at long times (and in large system sizes) is a necessary condition for localization. The slope of $\mathcal{I}$ versus t obtained for the four latest experimental times reported is $-1.017(\pm 1.028) \times 10^{-4}$ for the largest disorder strength. Here we see that the experimental error is too large to definitively show a vanishing of the slope since the results are also consistent with just a small slope. Within GMFT, we find a small non-zero slope: $-4.433(\pm 0.053) \times 10^{-4}$, for the largest disorder strength. The small non-zero slope shows that a slow rebalancing (as expected in the glassy state captured within GMFT) is consistent with experiment.

5.5 Phenomenological Parameter

To improve comparison with experiment we introduce a phenomenological parameter that excludes particles which move too slowly within GMFT. GMFT underestimates the speed

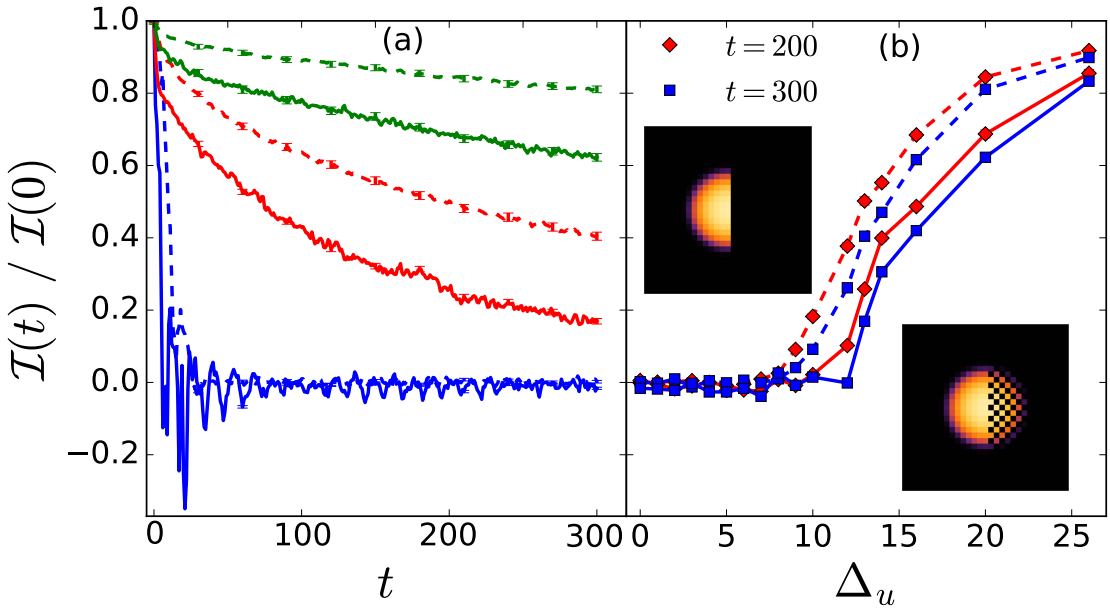

Figure 5.3: The solid (dashed) lines plot the normalized imbalance where the right half of the trap was initialized to a checkerboard (empty) pattern as shown in the insets. (a) The normalized imbalance against time for various disorder strengths. The pairs of (solid/-dashed) lines correspond to uniform disorder $\Delta_u = 0, 13$ and 20 from bottom to top. (b) The normalized imbalance at times $t = 200$ and 300 against disorder strength. The other parameters are $U = 24.4$, $\Omega = 0.145$, and $\mu = 4$.

of the MI dynamics under an applied field. The motion of the entire trapped system is therefore slower in GMFT at long times.

To account for the slow Mott particles we introduce a phenomenological parameter to our GMFT analysis. The inset of Fig. 5.2(d) shows a schematic of a resizing of the window used to compute the imbalance. The rectangles in the schematics indicate a decrease in l_x in Eq. (5.4), from l_W to l'_W. Our phenomenological parameter, l_x, therefore increases the relative rate of rebalancing because slow moving Mott particles near the left edge of the system are excluded from the data analysis. Decreasing μ also removes these particles. We find that tuning either μ or l_x allows us to fit $\mathcal{I}$ versus t to experimental values with the same accuracy. We choose l_x as our phenomenological parameter and vary it to obtain a best fit for the largest disorder, $\Delta_g = 13$.

Figures 5.2(c) and 5.2(d) plot the same as panels (a) and (b) but with the new window size, l'_W. Here there is much better agreement with experiment because the relative fraction of mobile to localized particles in our GMFT is closer to the experiment. Panels (e) and (f) include nonzero temperature. In varying T we find little change for $T < J$. $T = 0.2J$ was chosen as a best fit for the largest disorder. In Fig. 5.2(e) we see that t^* diminishes and the imbalance tends to level off quicker at long times, with a slight increase in the slope to $-4.816(\pm 0.160) \times 10^{-4}$.

The comparisons between theory and experiment in Fig. 5.2 show that by adjusting a single phenomenological parameter we can bring GMFT into better agreement with experiments. We therefore conclude that the long-time relaxation found in experiments can be interpreted within GMFT as glassy dynamics consistent with the out of equilibrium properties of a BG and its excitations.

5.6 Checkerboard Case

The initial expansion of bosons in the empty half of the trap in the presence of disorder is expected to be dominated by Anderson physics, due to the low site occupations. In order to test how enhancing interactions by increasing site occupations affects the expansion, we have devised an "improved" initial state generated by emptying sites in one half of the system according to a checkerboard pattern. The dynamics then proceeds by allowing the remaining bosons to evolve without any change in the Hamiltonian parameters (no parameter quenching). Before emptying sites, the system was in the ground state.

Fig. 5.3 plots the normalized imbalance for the checkerboard pattern. The pattern speeds up the decay of $\mathcal{I}(t)/\mathcal{I}(0)$ by enhancing the effect of interactions during the dynamics. It would be interesting to find out how changes in the pattern used for the initial state change the results in the experiments [56].

5.7 Non-quenched Dynamics for Uniformly Distributed Disorder

To understand the robustness of our findings within GMFT, we have also studied initial states at finite temperatures, different quench protocols, and dynamics in the presence of a uniform disorder distribution. The results show that the latter two changes do not have much impact on the imbalance dynamics at long times. GMFT shows that the imbalance dynamics of a BG or MI quenched into a disorder profile respond in nearly the same way.

We test whether the quench protocol impacts the dynamics qualitatively. We consider a non-quenched parameter set and study the dynamics of the imbalance. We allow the ground

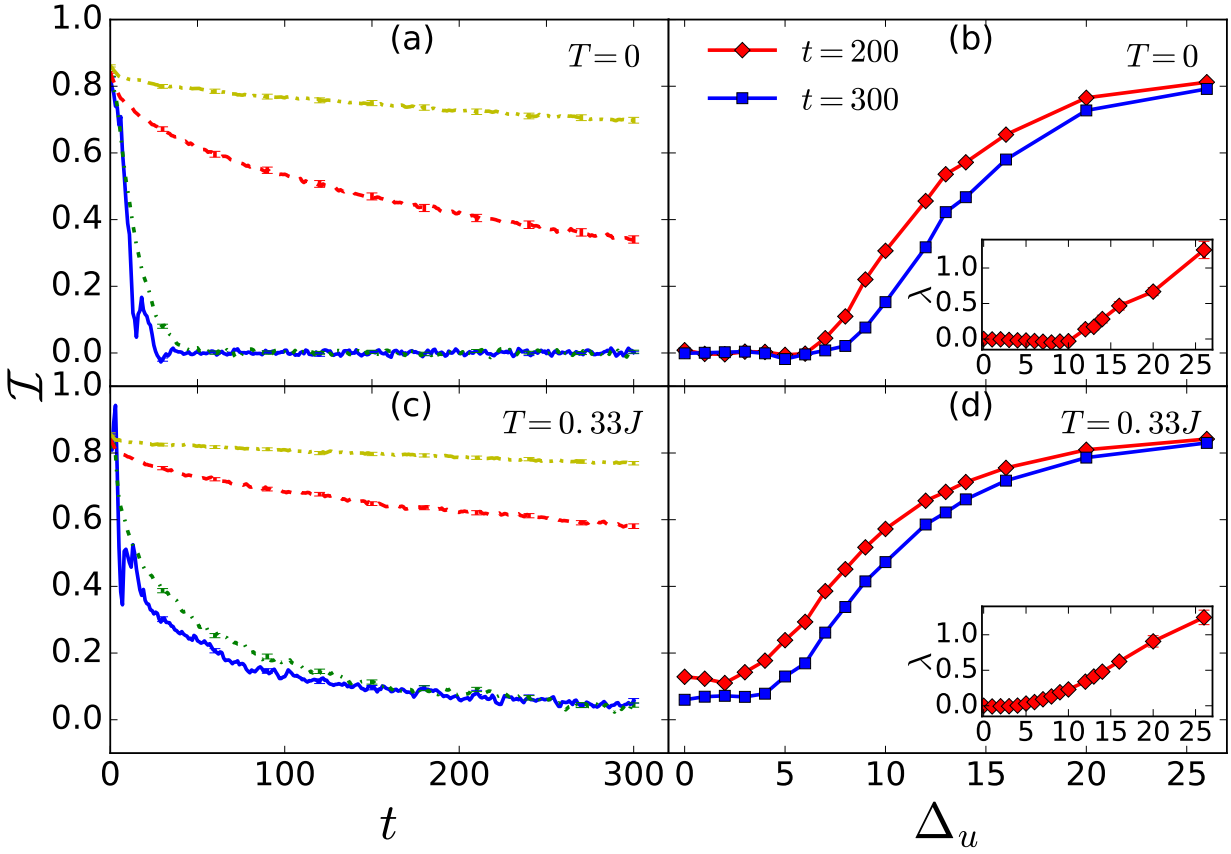

Figure 5.4: Time evolution of the imbalance $\mathcal{I}$ for various uniformly distributed disorder strengths when the initial temperature is $T = 0$ (a) and $T = 0.33$ (c). (b) and (d): Corresponding $\mathcal{I}$ for the same parameters but at times $t = 200$ and 300 against disorder strength. The initial state is the ground state of Eq. (5.1) of the main text for $U = 24.4$, $\Omega = 0.145$, and $\mu = 4$ in the presence of uniformly distributed disorder with strength Δ_u. In panels (a) and (c), the lines correspond to $\Delta_u = 0, 4, 13$ and 20 from bottom to top.

state to settle into the disorder profile before time evolving the system. The initial state is not a Mott insulator but rather a SF (or a BG for large disorder disorder). Here we consider the dynamics after removing all bosons in one half of the system but without quenching any Hamiltonian parameters. For this protocol, the initial state is selected to be the ground state for the same values of J, Ω, and U as in the experiment after the quench, but we trap a smaller number of bosons (the site occupations in the center of the trap are still very close to those in the Mott insulating state). Different from the quenched dynamics, here we take the disorder to be distributed uniformly in the interval $[-\Delta_u/2, \Delta_u/2]$, to show that the qualitative results do not depend on the details of the disorder profile.

Fig. 5.4(a) shows the time evolution of $\mathcal{I}$. Comparing Fig. 5.2(a) of the main text and Fig. 5.4(a) here one can see that the behavior of the non-quenched and quenched cases is qualitatively similar. Quantitative differences are, on the other hand, apparent. In the non-quenched dynamics there is no t^* such that $\mathcal{I}$ does not change appreciably for $t < t^*$. This is because the order parameter in the non-Mott regime is sizable. In addition, $\mathcal{I}$ decays more quickly in the non-quenched than in the quenched case. This is expected for weak disorder strengths, for which the initial state is SF, but it is also the case in the BG regime present for strong disorder. The results for $\mathcal{I}$ against Δ_u [Fig. 5.4(b)] and for λ against Δ_u [inset in Fig. 5.4(b)] are also qualitatively similar to the corresponding graphs in Fig. 2 of the main text. The onset of the localized regime increases as t increases. Figs. 5.4(c) and 5.4(d) show that the dynamics of the system slows down with the introduction of a nonzero temperature in the initial state. This is understandable as nonzero temperatures reduce the magnitude of the order parameter in the SF and BG phases [145]. Overall, we find no qualitative change in comparing the quenched and non-quenched cases.

5.8 Summary

Motivated by Ref. [56], we have studied the dynamics of bosons in 2D lattices with disorder by GMFT. We showed that theory becomes closer to experiment by including temperature and a single phenomenological parameter. We also showed that the features observed in the experiments are robust for various initial states: quenched MI, disordered superfluid, and BG. Since GMFT misses the entanglement present in MBL phases, evidence for MBL must lie in the differences between GMFT and experiments. We find that at the present stage with only the data from Ref. [56], it is difficult to tell if there is a qualitative or quantitative difference between GMFT and experiments. Further experiments, particularly at longer times, will be needed to unambiguously show that MBL is occurring. Avoiding macroscopic mass transport, as done in Ref. [138], will help rule out slow dynamics due to Anderson and BG physics.

Chapter 6

Phase Transitions of Spin-Orbit Coupled Bose-Hubbard Model in Optical Lattices

The work described in this chapter was published as:

Mi Yan, Yinyin Qian, Hoi-Yin Hui, Ming Gong, Chuanwei Zhang, and V. W. Scarola, "Spin-orbit-driven transitions between Mott insulators and finite-momentum superfluids of bosons in optical lattices," *Phys. Rev. A*, **96**, 053619 (2017) [77].

This work also appears in my collaborator Yinyin Qian's thesis [153] at The University of Texas at Dallas. Yinyin Qian is my coauthor on the paper, Ref. [77]. He used our paper [77] in his thesis [153] as well.

Yinyin Qian did the initial calculations. I performed completely new calculations to correct the initial wrong results and generated all the updated graphs in this paper with input from Professor Vito Scarola and Professor Chuanwei Zhang. All authors analyzed and discussed the results and contributed in writing the manuscript.

6.1 Introduction

The Rashba effect in solids derives from the motion of an electron in a strong electric field. As the electron moves in the presence of a potential gradient, ∇V, it experiences an effective magnetic field in its frame of reference. The Rashba energy:

$$(\vec{\nabla} V \times \vec{p}) \cdot \vec{\sigma}, \tag{6.1}$$

captures the energetics of electron spin reorientation due to the effective magnetic field, where $\vec{p}$ is the particle momentum and $\vec{\sigma}$ are the Pauli matrices. The Rashba spin-orbit coupling (SOC) energy is well known to be particularly strong at metallic surfaces [154, 155] (e.g., on Ag(111) or Au(111)) because here we find extremely strong potential gradients. As a result, studies of the impact of Rashba SOC on two-dimensional (2D) conductors have a long history. But the impact of Rashba SOC on the surface states of Mott insulators has come under more careful scrutiny recently because of possible connections to topological insulators [95, 96].

Mott insulators localize as a result of strong interaction and would therefore appear to exclude the possibility of SOC effects, but one can argue that this is not always the case. Small momentum in Eq. (6.1) (the case for localized states) does not necessarily imply low Rashba energies. In an extreme limit, Mott insulating surfaces can, in principle, experience very large potential gradients that can compensate the small momentum, i.e., $\langle p \rangle \to 0$ with $\langle \vec{\nabla} V \times \vec{p} \rangle \sim E_F$, where E_F is the Fermi energy. If, in this limit, the energetics of Rashba SOC compete with the Mott gap, one could observe a transition between a Mott insulator and a conducting state driven entirely by Rashba SOC in spite of the small average momentum of particles in Mott insulators. Unfortunately, the limit where Rashba SOC competes with the Mott gap is rare in solids because it would typically be precluded by other effects, such

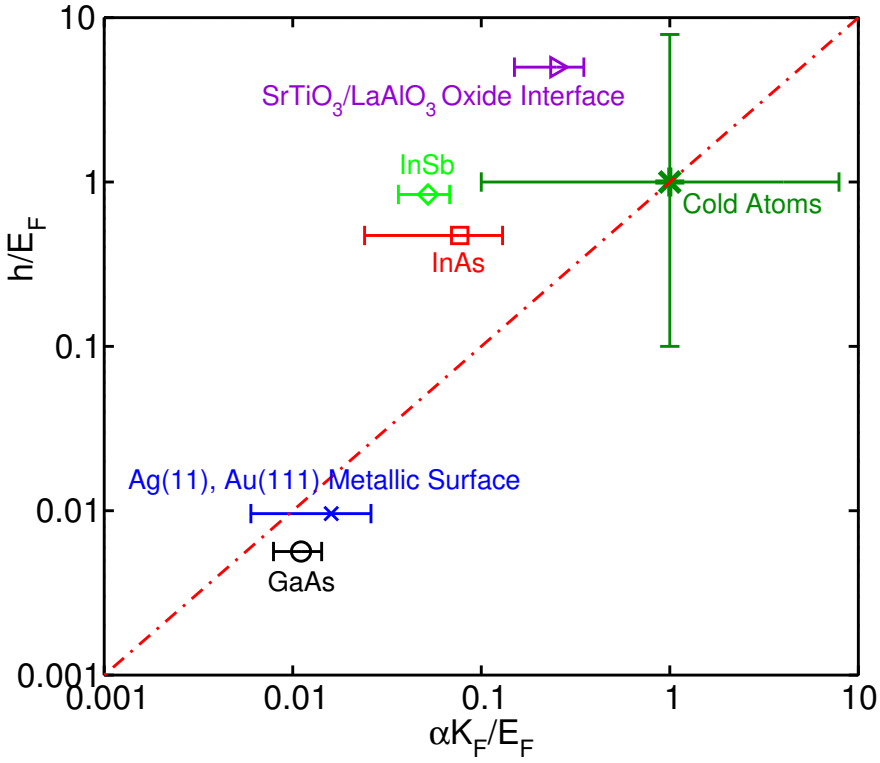

Figure 6.1: Comparison of SOC strengths in solids and cold atoms. h, α, and E_F denote the Zeeman energy, SOC coefficient, and Fermi energy, respectively. For GaAs, the effective mass is $m^* = 0.067m_0$[156], where m_0 is the electron mass, the Rashba SOC strength is $\alpha = (0.04 - 0.06) \times 10^{-11}$ eV·m[157], and the g-factor is $g^* = -0.45$[158]. For InAs the parameters are: $m^* = 0.026m_0$[156], $\alpha = (0.28 - 1.4) \times 10^{-11}$ eV·m[159], and $g^* = -15.1$. For InSb the parameters are: $m^* = 0.0135$[156], $\alpha K_F = (1.0 - 1.2) \times 10^{-11}$ eV·m[160], and $g^* = -51$. And for the metallic surfaces: $m^* \sim 0.255m_0$[154, 155], where the g-factor is assumed to be $g^* = 2$. The parameters for these four different examples are plotted at an external magnetic field of 5 Tesla. A high carrier density, $n = 10^{11}$ cm^{-2}, is used for the semiconductors. For $SrTiO_3/LaAlO_3$ oxide interfaces, the data are taken from Ref. [161] Additional feasible parameter regimes are plotted as horizontal and vertical bars.

as charge transfer between bands. But this limit can be explored in another context: using synthetic SOC in optical lattices.

Recent experimental progress [57–63] demonstrates engineering of synthetic SOC for ultracold atomic gases [42]. These experiments show that Raman beams can be used to dress atoms with a spin-dependent momentum. Rashba (and/or Dresselhaus) SOCs governing these dressed states [64, 65] are tunable to extremes not possible in solids, see Fig. 6.1. Recent work shows, for example, that synthetic SOC can generate flat bands [66–69], exotic superfluidity [70, 71], and intriguing vortex structures [65, 72–74].

Recent theory work has also explored the impact of SOC on the spin structure of Mott insulators in optical lattices [162–166]. Here super-exchange coupling between sites was shown to combine with Rashba SOC to lead to rich spin structures within the Mott state [162–166]. But in these studies parameters were chosen to explore the impact of Rashba SOC on the spin physics of Mott insulators while leaving the charge structure intact.

In this work we explore Rashba SOC that is strong enough to cause the breakdown of charge ordering in Mott insulators. This extreme limit is of direct relevance to optical lattice experiments with synthetic SOC. We study, in particular, a 2D lattice model of two-component interacting bosons in the presence of tunable Rashba coupling. We find that strong Rashba SOC can cause the breakdown of the Mott insulating state and drive a direct transition between the Mott insulator and a superfluid state, even in the *absence* of single particle tunneling between sites of the lattice [165]. This limit is the lattice version of the limit discussed above, $\langle p \rangle \to 0$ with $\langle \vec{\nabla} V \times \vec{p} \rangle \sim E_F$, where vanishing kinetics leaves Rashba SOC to generate its own conducting state. For the case of lattice bosons studied here, we find that Rashba SOC generates finite momentum superfluids. We show that these superfluids are characterized by staggered phase patterns. We also find distinct superfluid states with striped phase patterns that are separated by transitions on finite lattices with

periodic boundaries. We predict that finite momentum superfluids should be observable in time-of-flight (TOF) measurements of the momentum distribution.

The chapter is organized as follows: In Sec. 6.2 we construct a Bose-Hubbard model of two-component atoms in the presence of Rashba SOC. We also discuss two complimentary mean field approaches that allow us to compute the phase diagram, transition properties, and the momentum distribution. In Sec. 6.3 we present results on finite lattice sizes. We use Gutzwiller mean field theory to show that Rashba SOC causes the Bosonic Mott insulator to give way to finite momentum superfluids. We also explore inter-superfluid transitions. We find that transitions separate distinct phase patterns of finite momentum superfluids. We demonstrate in Sec. 6.4 that these different finite momentum phases can indeed be observed in experiments with a trapping potential. In Sec. 6.5 we present analytic arguments that transitions depend critically on boundary effects, akin to effects found in Fulde-Ferrell-Larkin-Ovchinnikov (FFLO) superconductors [167–177]. We show that analytic mean field calculations in the infinite system size limit do not show these transitions. We summarize in Sec. 6.6.

6.2 Model and Methods

We consider a 2D square optical lattice containing bosonic atoms with two hyperfine levels. States with two hyperfine levels act as a pseudo-spin 1/2 state. We also assume the presence of Raman beams that couple the atomic momentum to the spin to generate synthetic SOC [57, 59–61, 63]. The interaction between alkali atoms is governed by a short-range (s-wave) repulsion. For a deep optical lattice, the problem can be accurately described in the single-band, tight-binding limit [8] where the s-wave interaction becomes an on-site Hubbard interaction and the SOC is discretized.

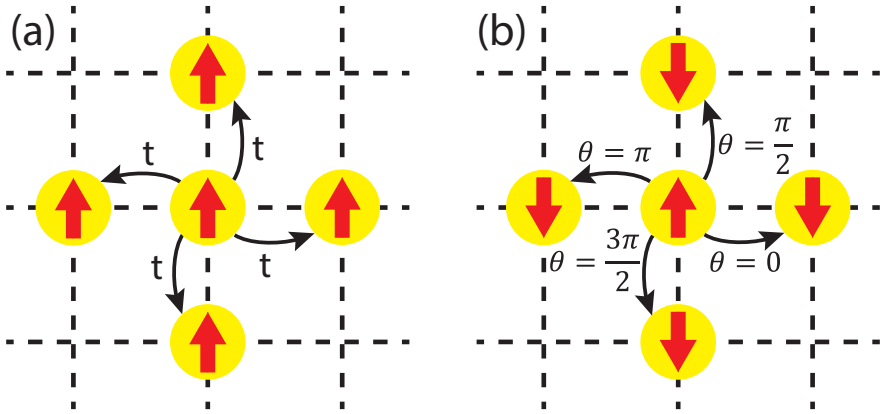

Figure 6.2: Schematic of spin independent tunneling (a) and spin-dependent tunneling induced by SOC (b). In the later case, the tunneling takes place between two neighboring sites accompanied by both spin flipping and phase variations. The phase variation during tunneling is responsible for the creation of the finite momentum superfluids.

To study this system we construct a Hubbard model of two-component bosons in the presence of Rashba SOC on a square lattice. We allow the on-site Hubbard interaction to have a spin-dependent interaction:

$$\begin{aligned} H &= -t\sum_{\langle ij\rangle}\Psi_i^\dagger\Psi_j + \frac{U}{2}\sum_{i\sigma} n_{i\sigma}(n_{i\sigma}-1) \\ &+ U_{\uparrow\downarrow}\sum_i n_{i\uparrow}n_{i\downarrow} - \mu\sum_{i\sigma} n_{i\sigma} \\ &+ i\lambda\sum_{\langle ij\rangle}\Psi_i^\dagger\vec{e}_z\cdot(\vec{\sigma}\times\vec{d}_{ij})\Psi_j + H.c., \end{aligned} \tag{6.2}$$

where, $\Psi_i = (b_{i\uparrow}, b_{i\downarrow})^T$ is a two-component bosonic annihilation operator at the site i, $n_{i\sigma} = b_{i\sigma}^\dagger b_{i\sigma}$, t is the spin-independent nearest neighbor tunneling, U ($U_{\uparrow\downarrow}$) is the on-site interaction between bosons of the same (different) spin σ, and μ is the chemical potential. In the last term λ is the Rashba SOC strength, $\vec{d}_{ij}$ is the unit vector between the neighboring sites i and j, and $\vec{e}_z$ is the unit vector along the z direction. In the following we use $U = 1$ to set the energy scale.

The tunneling and Rashba terms induce two *different* types of superfluidity. To see this we

plot the spin-independent tunneling and spin-dependent tunneling in Fig. 6.2. The left panel shows that the spin-independent tunneling favors phase uniformity since t is real. But in the right panel we see that SOC has two effects: It induces tunneling between neighboring sites with two different spin states and it imposes phase variation. The phase variation depends strongly on the direction of the neighboring sites. SOC therefore favors highly anisotropic superfluid states. Without SOC the system has at least an $U(1) \otimes U(1)$ symmetry, which means that the total number of each species are conserved; however, SOC introduces spin flips between two neighboring sites, thus the system only respects $U(1)$ symmetry and, as a result, the phase difference between the neighboring sites can not be gauged out. The competition between spin-independent tunneling and spin-dependent tunneling tunes the transition between these different superfluids.

In the weakly interacting limit the model exhibits three different superfluid phases: In the regime when spin-independent tunneling dominates ($t \gg \lambda$), the uniform superfluid is preferred and the total momentum of the superfluid is zero; In the opposite regime, a staggered superfluid phase is preferred; and in the intermediate regime, $t \sim \lambda$, the strong competition between the two tunnelings gives rise to superfluids with phase patterns that depend strongly on boundary effects.

Strong interactions add competing Mott insulating phases and complicates estimates of the phase diagram. To study the competition between all ground states we use two complimentary mean field approaches. We apply the Gutzwiller mean field method to finite system sizes (relevant to experiments) and compare with an otherwise equivalent mean field method applied to infinite system sizes.

We now discuss the Gutzwiller mean field method [8, 178]. The method assumes a product ground state of the form: $|G\rangle = \prod_{i,\sigma} \left(\sum_n f_n^{(i,\sigma)} |n\rangle_{i,\sigma} \right)$. This form for the wavefunction has been extensively applied to bosons in optical lattices [8], even in the presence of complex

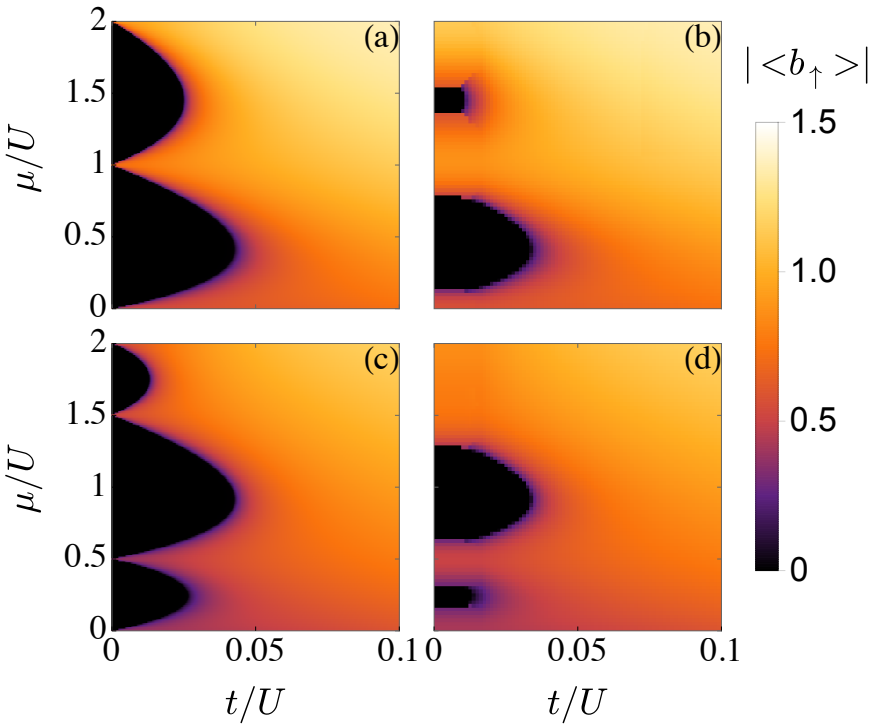

Figure 6.3: Phase diagrams of Eq. (6.2) obtained from Gutzwiller variational simulations for an 8×8 lattice with periodic boundary condition at (a) $U_{\uparrow\downarrow} = 0, \lambda = 0$, (b) $U_{\uparrow\downarrow} = 0, \lambda = 0.04U$, (c) $U_{\uparrow\downarrow} = 0.5U, \lambda = 0$, and (d) $U_{\uparrow\downarrow} = 0.5U, \lambda = 0.04U$. The phase diagrams are determined by the amplitude of the spin-up superfluid order parameter. The spin-down superfluid order parameter produces similar results.

hopping amplitudes [115]. It generally gives quantitatively reliable results in 2D and 3D, (for comparisons, see, e.g., Ref. [87]), and is a particularly excellent approximation when computing local correlation functions (see, e.g., Ref. [179]). The variational parameters f are obtained by minimizing the total energy:

$$E = \frac{\langle G|H|G\rangle}{\langle G|G\rangle}. \tag{6.3}$$

We minimize the total ground state energy with the conjugate gradient algorithm [85, 86]. The ground state energy is reached when the energy variation is less than $10^{-5}U$, which is sufficient to distinguish the energy difference between different phases.

We supplement the finite system size Gutzwiller method with an equivalent mean field limit applied to infinite system sizes. We assume $\langle b_{i\sigma} \rangle = \psi e^{i\theta_{i\sigma}}$, where ψ is a real number. This assumption is equivalent to the assumed form for $|G\rangle$ but works best on infinite system sizes. The total energy then becomes:

$$E_\psi = (U + U_{\uparrow\downarrow})\psi^4 - (U + 2\mu + tA + \lambda B)\psi^2, \tag{6.4}$$

where the coefficients are:

$$A \equiv N^{-1} \sum_{\langle ij \rangle} \left[e^{i(\theta_{j\uparrow} - \theta_{i\uparrow})} + e^{i(\theta_{j\downarrow} - \theta_{i\downarrow})} + H.c. \right], \tag{6.5}$$

and:

$$B \equiv N^{-1} \sum_{\langle ij \rangle} \left[Z_{ij}^* e^{i(\theta_{j\downarrow} - \theta_{i\uparrow})} - Z_{ij} e^{i(\theta_{j\uparrow} - \theta_{i\downarrow})} + H.c. \right], \tag{6.6}$$

with $Z_{ij} \equiv d_{ij}^x + i d_{ij}^y$ and N is the number of sites. An important point here is that the total energy depends not only on the magnitude of the order parameter ψ, but also on the phase difference between neighboring sites. We see that the minimal energy E_ψ corresponds to a maximal value of A and B when U, $U_{\uparrow\downarrow}$, λ, and t assume positive values (the case studied in this chapter). Here A depends only on the phase difference between the same spin states, while B depends strongly on the phase difference between spin up and spin down states in the neighboring sites. The competition between A and B governs competition between superfluids with distinct phase patterns. When $\lambda = 0$, A takes its maximum value when all of the sites have the same phase, which corresponds to the uniform superfluid phase.

6.3 Quantum Phases in Finite Lattices with Periodic Boundaries

We now discuss results that demonstrate the competition between various Mott and superfluid phases in the presence of SOC. We first present our results on small system sizes with periodic boundaries. These system sizes are consistent with small states formed in the center of traps in experiments.

Fig. 6.3 shows the phase diagram for four different limits of the model, Eq. (6.2). Fig. 6.3a plots the Bose-Hubbard phase diagram [7] that results from setting the SOC term and the inter-spin interaction term to zero in Eq. (6.2), i.e., $\lambda = U_{\uparrow\downarrow} = 0$. The absence of inter-spin interactions allows two identical copies of the Mott insulator. The lower and upper Mott lobes in Fig. 6.3a correspond to $\langle n_{i\uparrow}\rangle = \langle n_{i\downarrow}\rangle = 1$ and $\langle n_{i\uparrow}\rangle = \langle n_{i\downarrow}\rangle = 2$, respectively.

Fig. 6.3c shows the result of adding inter-spin repulsion, $U_{\uparrow\downarrow} > 0$, but with no SOC, $\lambda = 0$. Here we see that that the original low energy Mott lobe is pushed up. The appearance of the small Mott lobes (above and below the larger Mott lobe) correspond to the formation of Mott insulators with Ising-type spin ordering. To see this, we rewrite the interaction terms in H using sum and difference operators, $n_{i\pm} \equiv n_{i\uparrow} \pm n_{i\downarrow}$. The large Mott lobe in Fig. 6.3c then corresponds to $\langle n_{i+}\rangle = 2, \langle n_{i-}\rangle = 0$. The upper and lower small Mott lobes exhibit degeneracies (for $t = 0$) and correspond to $\langle n_{i+}\rangle = 3, \langle n_{i-}\rangle = \pm 1$ and $\langle n_{i+}\rangle = 1, \langle n_{i-}\rangle = \pm 1$, respectively. Here we exclude super exchange effects, $\mathcal{O}(t^2/U)$, discussed in other work [162–164, 166].

We now discuss the phase diagram that results from adding SOC. Figs. 6.3b and 6.3d plot the phase diagrams that result from adding SOC to the states depicted in Figs. 6.3a and 6.3c, respectively. In both figures we see that the Mott insulators at higher μ vanish. Increasing

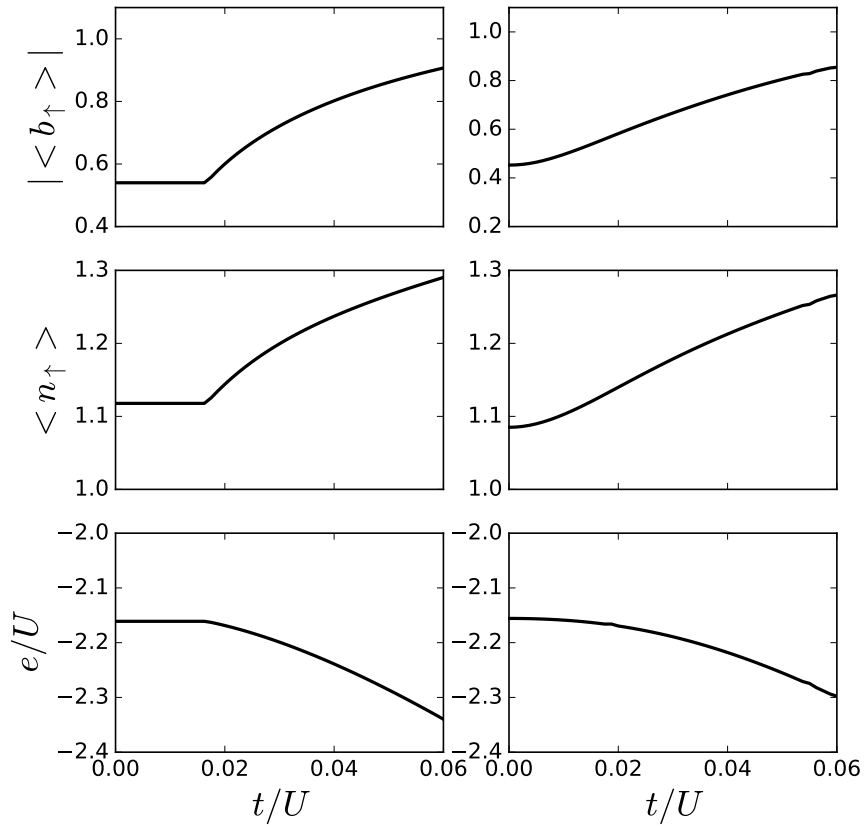

Figure 6.4: Plot of the amplitude of spin-up superfluid order parameter $|\langle b_\uparrow \rangle|$, the filling factor $\langle n_\uparrow \rangle$ and the energy density e as a function of the spin-independent tunneling at $U_{\uparrow\downarrow} = 0.5U$, $\lambda = 0.04U$ and $\mu = 1.33U$ for periodic (left panel) and open (right panel) boundary conditions.

μ causes a direct transition from a Mott insulator to a SOC-generated superfluid. At $t = 0$, SOC *alone* drives the formation of a superfluid. We find that the Mott insulators that normally persist at $t = 0$ for all μ are actually supplanted by SOC-generated superfluids. The $t = 0$ superfluids found on this part of the phase diagram derive kinetics purely from the spin-dependent tunneling in SOC. We therefore find that even in the limit of vanishing kinetics, the Rashba effect drives the Mott insulator into a conducting state (in this case, a superfluid state). We have also checked the phase diagrams of 4×4 and 6×6 lattices, and find no qualitvative difference with an 8×8 lattice shown in Fig. 6.3. Below we show that the precise nature of the resulting superfluid depends on the relative strengths of λ and t,

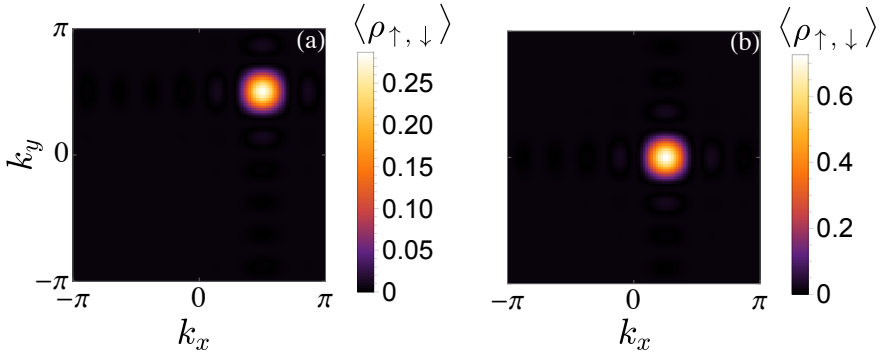

Figure 6.5: (Color online) Spin-dependent momentum distribution, Eq. (6.7), for different superfluids at $U_{\uparrow\downarrow} = 0.5U$, $\lambda = 0.04U$, $\mu = 1.33U$, (a) $t = 0.005U$, and (b) $t = 0.05U$.

as well as boundary effects.

Fig. 6.4 shows the transitions of different superfluid phase patterns. The left column shows the order parameters for the 8×8 lattice with periodic boundary conditions. Here SOC dominates and the nonzero order parameters are unchanged for $t \leq 0.019U$. For $t > 0.019U$, the order parameter gradually increases with t, which indicates a transition between different superfluids at $t \sim 0.019U$. For the open boundary condition case shown in the right column, there is no such transition since the phase can vary smoothly over the lattice.

The superfluids with different phase patterns have different momenta. To see this we compute the spin-dependent momentum distribution at wavevector k:

$$\langle \rho_{\uparrow,\downarrow}(\vec{k}) \rangle = N^{-2} \sum_{i,j} \langle b^{\dagger}_{i\uparrow} b_{j\downarrow} \rangle e^{i\vec{k}\cdot(\vec{R}_i - \vec{R}_j)}, \tag{6.7}$$

where the lattice spacing is chosen as the unit of distance and $\vec{R}_j$ is the location of the lattice site j.

We take random initial guess states and minimize the total energy to compute the ground

state $|G\rangle$, with which the spin-dependent momentum distribution is computed as

$$\frac{\langle G|\rho_{\uparrow,\downarrow}(\vec{k})|G\rangle}{\langle G|G\rangle}. \tag{6.8}$$

We get four degenerate ground states with different momentum distributions, where the D_4 symmetry of the lattice system is spontaneously broken. Similar results have been discovered in the continuum model of spin-1/2 Bose- Einstein condensate with Rashaba SOC [180–182], where the ground state is a single plane-wave state with finite momentum, and the direction of plane wave is spontaneously determined when the inter-spin interaction is smaller than the intra-spin interaction.

The two different states in Fig. 6.5 have qualitatively distinct momentum distributions. We have also verified that in these two phases, the magnitude of the order parameter is uniform over the whole lattice, indicating that only the phase pattern changes during the transition. Note that the peak in the momentum distribution for the first two phases depends strongly on the ratio between λ and t. In the non-interacting limit, the ground state energy of the system with SOC is

$$E = -2t(\cos k_x + \cos k_y) - 2\lambda\sqrt{\sin^2 k_x + \sin^2 k_y}. \tag{6.9}$$

The energy minima are located at

$$\mathbf{k} = \big(\pm\arctan(\lambda/\sqrt{2}t), \pm\arctan(\lambda/\sqrt{2}t)\big). \tag{6.10}$$

On a finite 8×8 lattice, $\mathbf{k}$ can only take discrete values. In Particular, for $\lambda/t = 0.8$, the energy minima are located at $(0, \pi/4)$, $(0, -\pi/4)$, $(\pi/4, 0)$ and $(-\pi/4, 0)$. In the presence of interactions, D_4 symmetry is spontaneously broken and the system chooses one of the

minima in Fig. 5(b). Similarly, for $\lambda/t = 8$, the the energy minima are $\mathbf{k} = (\pm\pi/2, \pm\pi/2)$, which is consistant with Fig. 5(a). It is therefore possible to directly infer their ratio from the position of the peaks. We also note that the results presented in Fig. 6.5 relate directly to the time-of-flight imaging that can measure momentum distribution of distinct hyperfine states.

6.4 Quantum Phases in a Trapping Potential

We now consider the effects of realistic confinement on the superfluid transitions. The finite momentum superfluids considered here are akin to the FFLO phase discussed in the context of trapped atomic Fermi gases. The FFLO state depends strongly on lattice geometry. Finite size effects are normally not considered to be relevant in solids because system sizes are typically much larger than correlation lengths. But cold atomic gases can be put into regimes where the system size is on the order of superfluid correlation lengths.

Small magneto-optical trapping potentials can be created in cold atom systems. We add a spatially varying chemical potential term to Eq. (6.2) to model confinement:

$$\sum_i V(\vec{R}_i)(n_{i,\uparrow} + n_{i,\downarrow}). \tag{6.11}$$

The trapping potentials are well approximated by a parabolic potential. We consider:

$$V(\vec{R}_i) = 0.008U \left[\left(R_i^x - \frac{L_x - 1}{2} \right)^2 + \left(R_i^y - \frac{L_y - 1}{2} \right)^2 \right], \tag{6.12}$$

where $R_i^x (R_i^y)$ is the $x(y)$ coordinate of site i and L_x (L_y) is the lattice size along the x (y) direction. The trap coefficient is chosen to ensure that the trapped atom density vanishes before the edge of the lattice is reached. Within the mean-feild theory, we can compute the

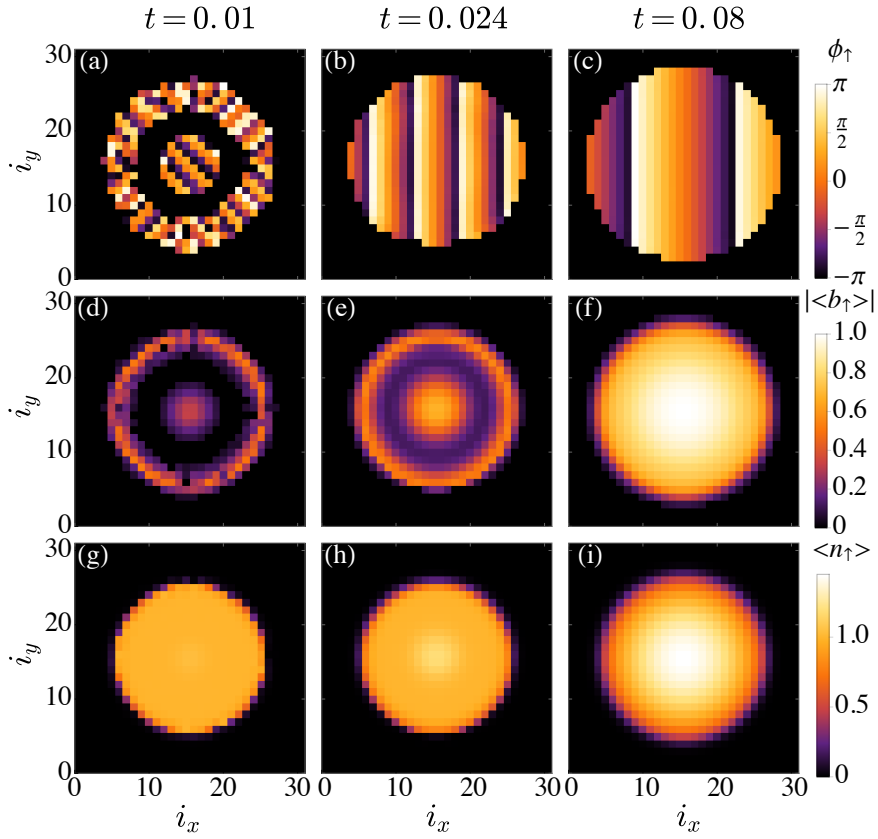

Figure 6.6: Correlation functions of finite momentum superfluids on a 32×32 lattice with a confining potential [Eq. (6.12)] for $\mu = 0.8U$, $U_{\uparrow\downarrow} = 0$ and $\lambda = 0.04U$. The left column shows results for $t = 0.01U$, the middle column for $t = 0.024U$ and the right column for $t = 0.08U$. The top three panels plot the phase $\phi_\uparrow$ of the spin up superfluid order parameter. The middle three panels plot the magnitude and the bottom three panels plot the density. The phase patterns in the top two panels reveal a sudden change in superfluid order.

local superluid order parameter in the trap $\langle b_{i,\sigma}\rangle = \sum_n \sqrt{n} f_{n-1}^{(i,\sigma)*} f_n^{(i,\sigma)}$. The local density is obtainted as $\langle n_{i,\sigma}\rangle = \sum_n n |f_n^{(i,\sigma)}|^2$.

We now show that the phase change, discussed in periodic systems above, also manifests in trapped systems. Fig. 6.6 shows a typical example obtained from solving Eq. (6.2) in the presence of parabolic trapping using the Gutzwiller ansatz with 10^4 random initial guess states. Since Mott insulator is a incoherent sate with random phases, phases of uparrow superfluid order parameter with $|\langle b_\uparrow\rangle| \leq 0.05$ are plotted with dark grey color in the top

panel of Fig. 6.6. As the hopping parameter increases, the phase reorients in the trap from non-uniform pattern to uniform due to the SOC effect. The effects predicted here are observable in measurements sensitive to the phase of the superfluid order parameter (e.g., the momentum distribution function). This calculation shows that realistic trapping potentials lead to finite sized systems that harbor the transitions found in periodic systems discussed above.

6.5 Quantum Phases in Infinite Lattices

So far our study has been limited to finite-sized lattices. Here boundary effects put a strong constraint on the superfluid phase patterns that can be realized. But we can use Eq. (6.4) to study infinite lattices. We find a general solution for the lowest-energy state, $\theta_{i\uparrow} = \alpha(R_i^y - R_i^x)$ and $\theta_{i\downarrow} = \frac{\pi}{4} + \alpha(R_i^y - R_i^x)$, where $\alpha = \arctan(\lambda\sqrt{2}/2t)$. The corresponding energy for just the kinetic terms is:

$$E_k = -(tA + \lambda B)\psi^2. \tag{6.13}$$

The competing superfluids arise from the competition between A and B coefficients.

Before studying the infinite system case we first test that Eq. (6.13) gives the same results as the Gutzwiller mean field theory. We find that this is the case by comparing results obtained from maximizing $tA + \lambda B$ in Eq. (6.13) on a finite lattice with the Gutzwiller mean field theory. We find precisely the same phase patterns given in Fig. 6.5. This confirms that the Gutzwiller mean field theory is equivalent to Eq. (6.13) on finite lattices.

We now study infinite lattice sizes. In the infinite system size limit we find:

$$E_k \to -4\sqrt{2}\lambda \sin(\alpha) - 8t\cos(\alpha). \tag{6.14}$$

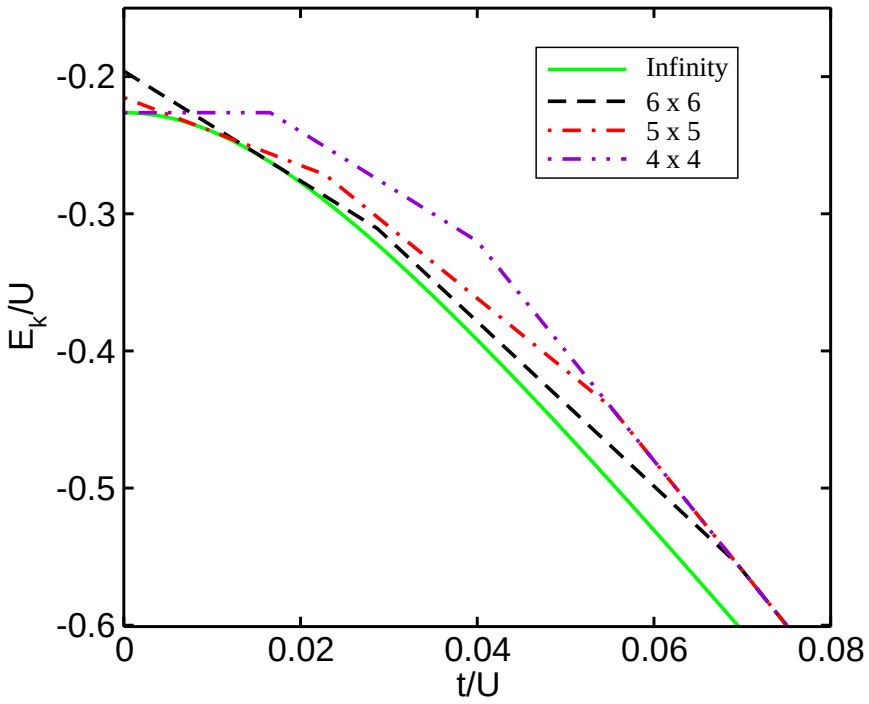

Figure 6.7: Plot of the kinetic energy terms, Eq. (6.13), as a function of the spin-independent tunneling at $\lambda = 0.04U$, for a 4×4, 5×5, 6×6 lattice and an infinite-size lattice.

This implies that the energy will change smoothly as the period of the finite momentum superfluids changes dramatically. Fig. 6.7 shows that the energy computed on the infinite system size is in fact smooth. We therefore conclude that infinite lattice sizes will eliminate transitions observed in finite sized systems. A similar result was found in studies of FFLO superfluids where periodic boundaries also constrain the FFLO momentum to select certain values [183, 184]. But we note that realistic experiments are actually trapped finite sized systems with $N \sim 10^2 - 10^5$. We therefore conclude that transitions between distinct superfluids found here should be observable in the small system limit defined by the trap center.

6.6 Summary

We have studied the interplay of strong interaction and Rashba SOC in a model motivated by optical lattice experiments: a 2D Hubbard model of two-component bosons. We used mean field theory to map out the phase diagram and study transitions. We find that strong Rashba SOC can completely destroy the Mott insulator state, even in the absence of spin-independent tunneling in the lattice. The Rashba SOC leads to superfluids with complex phase patterns and finite momentum. We identified transitions between superfluids with two different staggered phase patterns, that can be identified in the spin-dependent momentum distribution. The spin-dependent momentum could be accessed in time-of-flight measurements on optical lattices. We expect these transitions to occur in finite sized systems but the phase patterns and precise momenta depend strongly on the boundaries. We checked that these transitions in phase patterns become smooth in infinite system sizes.

Our work relates to the nature of Mott insulator states in solids. Our study of a 2D lattice finds that it is in principle possible for strong Rashba SOC to convert a Mott insulator into a conducting state even in the limit of vanishing kinetics ($t \to 0$ with $\lambda \sim 1$ in the lattice model or $\langle p \rangle \to 0$ with $\langle \vec{\nabla} V \times \vec{p} \rangle \sim E_F$ in the continuum). This limit could have bearing on the nature of 3D Mott insulator surface states that experience very weak kinetics but strong electric fields.

Chapter 7

Conclusions and Outlook

We now summarize our main findings in this thesis and discuss possible future research directions and open problems.

In Chapter 1, we provided the background of quantum simulations with cold atomic gases in optical lattices and the motivations of the research in this thesis.

In Chapter 2, we reviewed the theories and experiments of ultracold atoms in optical lattices. We applied the tight-binding approximation to derive the Bose-Hubbard model in the lowest band which describes the cold atoms in the optical lattice.

In Chapter 3, we discussed the phase diagrams of the Bose-Hubbard model in the presence and absence of disorder at zero temperature. The details of static and dynamic Gutzwiller approaches were presented to study the dynamics of cold atoms in optical lattices. The Bose glass in the Bose-Hubbard model with disorder and corresponding experiments in disordered optical lattices were discussed. We reviewed the experimental realization of spin-orbit coupling with cold atoms.

In Chapter 4, we studied the zero-temperature dynamics of states prepared in a disordered Bose-Hubbard model with a harmonic trap. We computed the COM velocity of a disordered superfluid, a disordered Mott insulator, and a Bose-glass with the time-dependent Gutzwiller method. While the disordered superfluid exhibits damped oscillations, the other two states are essentially motionless insulators near the trap center for strong interaction strengths.

We found that the COM velocity of trapped insulators is dominated by the flow of edge states. We also discussed two time scales for the trapped insulators. The edge superfluid flows around the insulating bulk to move the center of mass at short time scales. But for longer time scales, tunneling out of the bulk to the edge establishes a slow drift of the center of mass. Our results provide a lower bound on the COM velocity expected at non-zero temperature.

In Chapter 5, we have applied GMFT to study the dynamics of bosons in 2D lattices with disorder for a recent experiment in Ref. [56]. We found that GMFT qualitatively describes the experimental findings at zero temperature. We showed that theory becomes quantitatively closer to experiment by including a single phenomenological parameter and finite temperature. We also demonstrated that the features observed in the experiments are robust for various initial states: quenched MI, disordered superfluid, and Bose glass. We found that at the present stage with only the data from Ref. [56], it is difficult to distinguish if there is a qualitative or quantitative difference between GMFT and experiments. We concluded that evidence for MBL must lie in the differences between GMFT and experiments, since GMFT neglects the entanglement present in MBL phases.

In Chapter 6, we used GMFT to study the phase diagram and transitions of 2D Bose-Hubbard model with spin-orbit coupling. We found that strong spin-orbit coupling alone can wash out Mott insulators. The spin-orbit coupling leads to superfluid states with finite momentum and staggered phase patterns. We computed the spin-dependent momentum distribution to identify transitions between superfluid states with two different staggered phase patterns. TOF measurements in optical lattice experiments could allow access to the spin-dependent momentum distribution.

We now discuss some possible future research directions. While the superfluid–Bose glass quantum phase transition at non-zero temperature has been identified by quantum quenching

of disorder in an optical lattice in the weakly interacting regime [41], very few experimental or theoretical works have been done on the Mott insulator-Bose glass transition at non-zero temperature in the strongly interacting regime. In the future we can explore the Mott insulator-Bose glass transition by computing the core compressibility [90, 185] with GMFT and quantum Monte Carlo method, then make direct comparisons with experiments. This study will provide a deeper insight into the nature of Mott insulator-Bose glass transition at finite temperature.

In addition, the theoretical work in Chatper 5 underestimates the dynamics of the Mott regime by neglecting quantum fluctuations in the mean-field theory. We can add the higher order correlations in the equation of motions and investigate the domain wall expansion dynamics in Ref. [56] which may give us more accurate understanding about MBL in experiments. Also, further experiments, particularly at longer time scales, will be required to unambiguously show evidence of MBL. Avoiding macroscopic mass transport, as done in Ref. [138], might help rule out slow dynamics due to Anderson localization and Bose glass physics.

Bibliography

[1] M. H. Anderson, J. R. Ensher, M. R. Matthews, C. E. Wieman, and E. A. Cornell. Observation of Bose-Einstein Condensation in a Dilute Atomic Vapor. *Science*, 269(5221):198–201, July 1995.

[2] K. B. Davis, M. O. Mewes, M. R. Andrews, N. J. van Druten, D. S. Durfee, D. M. Kurn, and W. Ketterle. Bose-Einstein Condensation in a Gas of Sodium Atoms. *Physical Review Letters*, 75(22):3969–3973, November 1995.

[3] Max F. Riedel, Pascal Böhi, Yun Li, Theodor W. Hänsch, Alice Sinatra, and Philipp Treutlein. Atom-chip-based generation of entanglement for quantum metrology. *Nature*, 464(7292):1170–1173, April 2010.

[4] C. Gross, T. Zibold, E. Nicklas, J. Estève, and M. K. Oberthaler. Nonlinear atom interferometer surpasses classical precision limit. *Nature*, 464(7292):1165–1169, April 2010.

[5] S. Gupta, K. Dieckmann, Z. Hadzibabic, and D. E. Pritchard. Contrast Interferometry using Bose-Einstein Condensates to Measure h/m and α. *Physical Review Letters*, 89(14):140401, September 2002.

[6] M. Greiner, O. Mandel, T. Esslinger, T.W. Hansch, and I. Bloch. Quantum phase transition from a superfluid to a Mott insulator in a gas of ultracold atoms. *Nature*, 415(6867):39, JAN 3 2002.

[7] Matthew P. A. Fisher, Peter B. Weichman, G. Grinstein, and Daniel S. Fisher. Boson

localization and the superfluid-insulator transition. *Phys. Rev. B*, 40:546–570, Jul 1989.

[8] D. Jaksch, C. Bruder, J. I. Cirac, C. W. Gardiner, and P. Zoller. Cold bosonic atoms in optical lattices. *Phys. Rev. Lett.*, 81:3108–3111, Oct 1998.

[9] Cheng Chin, Rudolf Grimm, Paul Julienne, and Eite Tiesinga. Feshbach resonances in ultracold gases. *Reviews of Modern Physics*, 82(2):1225–1286, April 2010.

[10] Jean Dalibard, Fabrice Gerbier, Gediminas Juzeliūnas, and Patrik Öhberg. Colloquium: Artificial gauge potentials for neutral atoms. *Reviews of Modern Physics*, 83(4):1523–1543, November 2011.

[11] Renate Landig, Lorenz Hruby, Nishant Dogra, Manuele Landini, Rafael Mottl, Tobias Donner, and Tilman Esslinger. Quantum phases from competing short- and long-range interactions in an optical lattice. *Nature*, 532(7600):476–479, April 2016.

[12] S. Baier, M. J. Mark, D. Petter, K. Aikawa, L. Chomaz, Z. Cai, M. Baranov, P. Zoller, and F. Ferlaino. Extended Bose-Hubbard models with ultracold magnetic atoms. *Science*, 352(6282):201–205, April 2016.

[13] Bo Yan, Steven A. Moses, Bryce Gadway, Jacob P. Covey, Kaden R. A. Hazzard, Ana Maria Rey, Deborah S. Jin, and Jun Ye. Observation of dipolar spin-exchange interactions with lattice-confined polar molecules. *Nature*, 501(7468):521–525, September 2013.

[14] G. Birkl, M. Gatzke, I. H. Deutsch, S. L. Rolston, and W. D. Phillips. Bragg scattering from atoms in optical lattices. *Phys. Rev. Lett.*, 75(15):2823, Oct 1995.

[15] Matthias Weidemüller, Andreas Hemmerich, Axel Görlitz, Tilman Esslinger, and

Theodor W. Hänsch. Bragg diffraction in an atomic lattice bound by light. *Phys. Rev. Lett.*, 75:4583–4586, Dec 1995.

[16] Ehud Altman, Eugene Demler, and Mikhail D. Lukin. Probing many-body states of ultracold atoms via noise correlations. *Phys. Rev. A*, 70:013603, Jul 2004.

[17] Simon Foelling, S.lling, Fabrice Gerbier, Artur Widera, Olaf Mandel, Tatjana Gericke, and Immanuel Bloch. Spatial quantum noise interferometry in expanding ultracold atom clouds. *Nature*, 434(7032):481, Mar 2005.

[18] I. B. Spielman, W. D. Phillips, and J. V. Porto. Mott-insulator transition in a two-dimensional atomic Bose gas. *Phys. Rev. Lett.*, 98(8):080404, FEB 23 2007.

[19] P. T. Raum and V. W. Scarola. Thermometry for Laughlin States of Ultracold Atoms. *Physical Review Letters*, 118(11):115302, March 2017.

[20] Yin-Chen He, Fabian Grusdt, Adam Kaufman, Markus Greiner, and Ashvin Vishwanath. Realizing and adiabatically preparing bosonic integer and fractional quantum Hall states in optical lattices. *Physical Review B*, 96(20):201103, November 2017.

[21] V. W. Scarola and S. Das Sarma. Quantum Phases of the Extended Bose-Hubbard Hamiltonian: Possibility of a Supersolid State of Cold Atoms in Optical Lattices. *Physical Review Letters*, 95(3):033003, July 2005.

[22] Jun-Ru Li, Jeongwon Lee, Wujie Huang, Sean Burchesky, Boris Shteynas, Furkan Çağrı Top, Alan O. Jamison, and Wolfgang Ketterle. A stripe phase with supersolid properties in spin–orbit-coupled Bose–Einstein condensates. *Nature*, 543(7643):91–94, March 2017.

[23] J. E. Lye, L. Fallani, M. Modugno, D. S. Wiersma, C. Fort, and M. Inguscio. Bose-Einstein condensate in a random potential. *Phys. Rev. Lett.*, 95:070401, 2005.

[24] D. Clément, A. F. Varón, M. Hugbart, J. A. Retter, P. Bouyer, L. Sanchez-Palencia, D. M. Gangardt, G. V. Shlyapnikov, and A. Aspect. Suppression of transport of an interacting elongated Bose-Einstein condensate in a random potential. *Phys. Rev. Lett.*, 95:170409, 2005.

[25] C. Fort, L. Fallani, V. Guarrera, J. E. Lye, M. Modugno, D. S. Wiersma, and M. Inguscio. Effect of optical disorder and single defects on the expansion of a bose-einstein condensate in a one-dimensional waveguide. *Phys. Rev. Lett.*, 95:170410, Oct 2005.

[26] J. E. Lye, L. Fallani, C. Fort, V. Guarrera, M. Modugno, D. S. Wiersma, and M. Inguscio. Effect of interactions on the localization of a bose-einstein condensate in a quasiperiodic lattice. *Phys. Rev. A*, 75:061603, Jun 2007.

[27] L. Fallani, J. E. Lye, V. Guarrera, C. Fort, and M. Inguscio. Ultracold atoms in a disordered crystal of light: Towards a Bose glass. *Phys. Rev. Lett.*, 98:130404, 2007.

[28] J. Billy, V. Josse, Z. Zuo, A. Bernard, B. Hambrecht, P. Lugan, D. Clément, L. Sanchez-Palencia, P. Bouyer, and A. Aspect. Direct observation of Anderson localization of matter-waves in a controlled disorder. *Nature*, 453:891, 2008.

[29] G. Roati, C. D'Errico, L. Fallani, M. Fattori, C. Fort, M. Zaccanti, G. Modugno, M. Modugno, and M. Inguscio. Anderson localization of matter waves in a Bose-Einstein condensate. *Nature*, 453:895, 2008.

[30] Julien Chabé, Gabriel Lemarié, Benoît Grémaud, Dominique Delande, Pascal Szriftgiser, and Jean Claude Garreau. Experimental observation of the Anderson metal-insulator transition with atomic matter waves. *Phys. Rev. Lett.*, 101:255702, Dec 2008.

[31] Y. P. Chen, J. Hitchcock, D. Dries, M. Junker, C. Welford, and R. G. Hulet. Phase

coherence and superfluid-insulator transition in a disordered Bose-Einstein condensate. *Phys. Rev. A*, 77(1):033632, JUL 2008.

[32] D. Clément, P. Bouyer, A. Aspect, and L. Sanchez-Palencia. Density modulations in an elongated Bose-Einstein condensate released from a disordered potential. *Phys. Rev. A*, 77:033631, Mar 2008.

[33] A. Aspect and M. Inguscio. Anderson localization of ultracold atoms. *Phys. Today*, 62:30, 2009.

[34] Leonardo Fallani, Chiara Fort, and Massimo Inguscio. Bose-Einstein Condensates in Disordered Potentials. In *Advances in Atomic, Molecular, and Optical Physics*, volume 56 of *Advances In Atomic, Molecular, and Optical Physics*, pages 119 – 160. Academic Press, 2008.

[35] L. Sanchez-Palencia and M. Lewenstein. Disordered quantum gases under control. *Nat. Phys.*, 6(2):22, FEB 2010.

[36] M. White, M. Pasienski, D. McKay, S. Q. Zhou, D. Ceperley, and B. DeMarco. Strongly interacting bosons in a disordered optical lattice. *Phys. Rev. Lett.*, 102:055301, 2009.

[37] M. Pasienski, D. McKay, M. White, and B. DeMarco. A disordered insulator in an optical lattice. *Nat. Phys.*, 6:677, 2010.

[38] M. Robert-de Saint-Vincent, J.-P. Brantut, B. Allard, T. Plisson, L. Pezzé, L. Sanchez-Palencia, A. Aspect, T. Bourdel, and P. Bouyer. Anisotropic 2d diffusive expansion of ultracold atoms in a disordered potential. *Phys. Rev. Lett.*, 104:220602, Jun 2010.

[39] L. Tanzi, E. Lucioni, S. Chaudhuri, L. Gori, A. Kumar, C. D'Errico, M. Inguscio, and G. Modugno. Transport of a Bose gas in 1D disordered lattices at the fluid-insulator transition. *Phys. Rev. Lett.*, 111(11):115301, Sep 2013.

[40] Giovanni Modugno. Anderson localization in Bose-Einstein condensates. *Reports on Progress in Physics*, 73(10):102401, 2010.

[41] Carolyn Meldgin, Ushnish Ray, Philip Russ, David Chen, David M. Ceperley, and Brian DeMarco. Probing the Bose glass–superfluid transition using quantum quenches of disorder. *Nature Physics*, 12(7):646–649, July 2016.

[42] I. Bloch, J. Dalibard, and W. Zwerger. Many-body physics with ultracold gases. *Rev. Mod. Phys.*, 80:885, 2008.

[43] M. A. Cazalilla, R. Citro, T. Giamarchi, E. Orignac, and M. Rigol. One dimensional bosons: From condensed matter systems to ultracold gases. *Rev. Mod. Phys.*, 83:1405–1466, Dec 2011.

[44] M. Köhl, H. Moritz, T. Stöferle, K. Günter, and T. Esslinger. Fermionic atoms in a three dimensional optical lattice: Observing Fermi surfaces, dynamics, and interactions. *Phys. Rev. Lett.*, 94:080403, Mar 2005.

[45] J. Billy, V. Josse, Z. Zuo, A. Bernard, B. Hambrecht, P. Lugan, D. Clément, L. Sanchez-Palencia, P. Bouyer, and A. Aspect. Direct observation of Anderson localization of matter waves in a controlled disorder. *Nature*, 453(7197):891, 2008.

[46] G. Lemarié, J. Chabé, P. Szriftgiser, J.C. Garreau, B. Grémaud, and D. Delande. Observation of the Anderson metal-insulator transition with atomic matter waves: Theory and experiment. *Phys. Rev. A*, 80(4):043626, Oct 2009.

[47] S. S. Kondov, W. R. McGehee, J. J. Zirbel, and B. DeMarco. Three-dimensional Anderson localization of ultracold matter. *Science*, 334:66, October 2011.

[48] F. Jendrzejewski, A. Bernard, K. Mulller, P. Cheinet, V. Josse, M. Piraud, L. Pezze,

L. Sanchez-Palencia, A. Aspect, and P. Bouyer. Three-dimensional localization of ultracold atoms in an optical disordered potential. *Nat. Phys.*, 8(5):398, Mar 2012.

[49] D. M. Basko, I. L. Aleiner, and B. L. Altshuler. Metal-insulator transition in a weakly interacting many-electron system with localized single-particle states. *Ann. Phys.*, 321:1126, 2006.

[50] V. Oganesyan and D.A. Huse. Localization of interacting fermions at high temperature. *Phys. Rev. B*, 75(15):155111, April 2007.

[51] Arijeet Pal and David A. Huse. Many-body localization phase transition. *Phys. Rev. B*, 82(17):174411, Nov 2010.

[52] J. M. Deutsch. Quantum statistical mechanics in a closed system. *Phys. Rev. A*, 43(4):2046, Feb 1991.

[53] M. Srednicki. Chaos and quantum thermalization. *Phys. Rev. E*, 50(2):888, Aug 1994.

[54] M. Rigol, V. Dunjko, and M. Olshanii. Thermalization and its mechanism for generic isolated quantum systems. *Nature*, 452(7189):854, Apr 2008.

[55] R. Nandkishore and D. A. Huse. Many-body localization and thermalization in quantum statistical mechanics. *Annu. Rev. Condens. Matter Phys.*, 6(1):15?Äì38, Mar 2015.

[56] J.-Y. Choi, S. Hild, J. Zeiher, P. Schaub, A. Rubio-Abadal, T. Yefsah, V. Khemani, D. A. Huse, I. Bloch, and C. Gross. Exploring the many-body localization transition in two dimensions. *Science*, 352(6293):1547–1552, April 2016.

[57] Y.-J. Lin, K. Jiménez-García, and I. B. Spielman. Spin-orbit-coupled Bose-Einstein condensates. *Nature*, 471:83, 2011.

[58] Pengjun Wang, Zeng-Qiang Yu, Zhengkun Fu, Jiao Miao, Lianghui Huang, Shijie Chai, Hui Zhai, and Jing Zhang. Spin-Orbit Coupled Degenerate Fermi Gases. *Physical Review Letters*, 109(9):095301, August 2012.

[59] Lawrence W. Cheuk, Ariel T. Sommer, Zoran Hadzibabic, Tarik Yefsah, Waseem S. Bakr, and Martin W. Zwierlein. Spin-injection spectroscopy of a spin-orbit coupled Fermi gas. *Phys. Rev. Lett.*, 109:095302, Aug 2012.

[60] Jin-Yi Zhang, Si-Cong Ji, Zhu Chen, Long Zhang, Zhi-Dong Du, Bo Yan, Ge-Sheng Pan, Bo Zhao, You-Jin Deng, Hui Zhai, Shuai Chen, and Jian-Wei Pan. Collective Dipole Oscillations of a Spin-Orbit Coupled Bose-Einstein Condensate. *Physical Review Letters*, 109(11):115301, September 2012.

[61] Zhengkun Fu, Lianghui Huang, Zengming Meng, Pengjun Wang, Xia-Ji Liu, Han Pu, Hui Hu, and Jing Zhang. Radio-frequency spectroscopy of a strongly interacting spin-orbit-coupled Fermi gas. *Phys. Rev. A*, 87:053619, May 2013.

[62] Chunlei Qu, Chris Hamner, Ming Gong, Chuanwei Zhang, and Peter Engels. Observation of *Zitterbewegung* in a spin-orbit-coupled Bose-Einstein condensate. *Phys. Rev. A*, 88:021604, Aug 2013.

[63] R. A. Williams, M. C. Beeler, L. J. LeBlanc, K. Jiménez-García, and I. B. Spielman. Raman-induced interactions in a single-component Fermi gas near an s-wave Feshbach resonance. *Phys. Rev. Lett.*, 111:095301, Aug 2013.

[64] V. Galitski and I. B. Spielman. Spin-orbit coupling in quantum gases. *Nature*, 494:49, February 2013.

[65] Jay D. Sau, Rajdeep Sensarma, Stephen Powell, I. B. Spielman, and S. Das Sarma. Chi-

ral Rashba spin textures in ultracold Fermi gases. *Physical Review B*, 83(14):140510, April 2011.

[66] Fei Lin, Chuanwei Zhang, and V. W. Scarola. Emergent Kinetics and Fractionalized Charge in 1d Spin-Orbit Coupled Flatband Optical Lattices. *Physical Review Letters*, 112(11):110404, March 2014.

[67] Yongping Zhang and Chuanwei Zhang. Bose-Einstein condensates in spin-orbit-coupled optical lattices: Flat bands and superfluidity. *Phys. Rev. A*, 87:023611, Feb 2013.

[68] Hoi-Yin Hui, Yongping Zhang, Chuanwei Zhang, and V. W. Scarola. Superfluidity in the absence of kinetics in spin-orbit-coupled optical lattices. *Physical Review A*, 95(3):033603, March 2017.

[69] Mengsu Chen and V. W. Scarola. Stability of emergent kinetics in optical lattices with artificial spin-orbit coupling. *Physical Review A*, 94(4):043601, October 2016.

[70] Hui Hu, B. Ramachandhran, Han Pu, and Xia-Ji Liu. Spin-Orbit Coupled Weakly Interacting Bose-Einstein Condensates in Harmonic Traps. *Physical Review Letters*, 108(1):010402, January 2012.

[71] B. Ramachandhran, Hui Hu, and Han Pu. Emergence of topological and strongly correlated ground states in trapped Rashba spin-orbit-coupled Bose gases. *Physical Review A*, 87(3):033627, March 2013.

[72] B. Ramachandhran, Bogdan Opanchuk, Xia-Ji Liu, Han Pu, Peter D. Drummond, and Hui Hu. Half-quantum vortex state in a spin-orbit-coupled Bose-Einstein condensate. *Phys. Rev. A*, 85:023606, Feb 2012.

[73] Wu Cong-Jun, Ian Mondragon-Shem, and Zhou Xiang-Fa. Unconventional Bose—

Einstein Condensations from Spin-Orbit Coupling. *Chinese Physics Letters*, 28(9):097102, 2011.

[74] Xiangfa Zhou, Yi Li, Zi Cai, and Congjun Wu. Unconventional states of bosons with the synthetic spin–orbit coupling. *Journal of Physics B: Atomic, Molecular and Optical Physics*, 46(13):134001, 2013.

[75] Mi Yan, Hoi-Yin Hui, and V. W. Scarola. Dynamics of disordered states in the Bose-Hubbard model with confinement. *Physical Review A*, 95(5):053624, May 2017.

[76] Mi Yan, Hoi-Yin Hui, Marcos Rigol, and V. W. Scarola. Equilibration Dynamics of Strongly Interacting Bosons in 2d Lattices with Disorder. *Physical Review Letters*, 119(7):073002, August 2017.

[77] Mi Yan, Yinyin Qian, Hoi-Yin Hui, Ming Gong, Chuanwei Zhang, and V. W. Scarola. Spin-orbit-driven transitions between Mott insulators and finite-momentum superfluids of bosons in optical lattices. *Physical Review A*, 96(5):053619, November 2017.

[78] I Bloch. Ultracold quantum gases in optical lattices. *Nat. Phys.*, 1:23, 2005.

[79] C. Becker, P. Soltan-Panahi, J. Kronjäger, S. Dörscher, K. Bongs, and K. Sengstock. Ultracold quantum gases in triangular optical lattices. *New Journal of Physics*, 12(6):065025, 2010.

[80] L. Santos, M. A. Baranov, J. I. Cirac, H.-U. Everts, H. Fehrmann, and M. Lewenstein. Atomic Quantum Gases in Kagom\'e Lattices. *Physical Review Letters*, 93(3):030601, July 2004.

[81] J. Ruostekoski. Optical Kagome Lattice for Ultracold Atoms with Nearest Neighbor Interactions. *Physical Review Letters*, 103(8):080406, August 2009.

[82] P. Soltan-Panahi, J. Struck, P. Hauke, A. Bick, W. Plenkers, G. Meineke, C. Becker, P. Windpassinger, M. Lewenstein, and K. Sengstock. Multi-component quantum gases in spin-dependent hexagonal lattices. *Nature Physics*, 7(5):434–440, May 2011.

[83] Parvis Soltan-Panahi, Dirk-Sören Lühmann, Julian Struck, Patrick Windpassinger, and Klaus Sengstock. Quantum phase transition to unconventional multi-orbital superfluidity in optical lattices. *Nature Physics*, 8(1):71–75, January 2012.

[84] R. Roth and K. Burnett. Superfluidity and interference pattern of ultracold bosons in optical lattices. *Physical Review A*, 67(3):031602, March 2003.

[85] P. Debye. Näherungsformeln für die Zylinderfunktionen für große Werte des Arguments und unbeschränkt veränderliche Werte des Index. *Mathematische Annalen*, 67(4):535–558, December 1909.

[86] P. Deift and X. Zhou. A Steepest Descent Method for Oscillatory Riemann–Hilbert Problems. Asymptotics for the MKdV Equation. *Annals of Mathematics*, 137(2):295–368, 1993.

[87] J Zakrzewski. Mean field dynamics of superfluid-insulator phase transition in a gas of ultra cold atoms. *Phys. Rev. A*, 71:043601, SEP 2005.

[88] I. Hen and M. Rigol. Analytical and numerical study of trapped strongly correlated bosons in two- and three-dimensional lattices. *Phys. Rev. A*, 82:043634, Oct 2010.

[89] D. Jaksch, V. Venturi, J. I. Cirac, C. J. Williams, and P. Zoller. Creation of a molecular condensate by dynamically melting a mott insulator. *Phys. Rev. Lett.*, 89(4):040402, Jul 2002.

[90] Y. Khorramzadeh, Fei Lin, and V. W. Scarola. Boson core compressibility. *Physical Review A*, 85(4):043610, April 2012.

[91] T. Giamarchi and H. J. Schulz. Localization and Interaction in One-Dimensional Quantum Fluids. *EPL (Europhysics Letters)*, 3(12):1287, 1987.

[92] T. Giamarchi and H. J. Schulz. Anderson localization and interactions in one-dimensional metals. *Physical Review B*, 37(1):325–340, January 1988.

[93] V. Gurarie, L. Pollet, N. V. Prokof'ev, B. V. Svistunov, and M. Troyer. Phase diagram of the disordered Bose-Hubbard model. *Phys. Rev. B*, 80:214519, 2009.

[94] Erich J. Mueller. Viewpoint: Spin-Orbit Coupling Comes in From the Cold. *Physics*, 5, August 2012.

[95] M. Z. Hasan and C. L. Kane. Colloquium: Topological insulators. *Reviews of Modern Physics*, 82(4):3045–3067, November 2010.

[96] Xiao-Liang Qi and Shou-Cheng Zhang. Topological insulators and superconductors. *Reviews of Modern Physics*, 83(4):1057–1110, October 2011.

[97] Joseph Maciejko, Taylor L. Hughes, and Shou-Cheng Zhang. The Quantum Spin Hall Effect. *Annual Review of Condensed Matter Physics*, 2(1):31–53, February 2011.

[98] Gang Chen, Rodrigo Pereira, and Leon Balents. Exotic phases induced by strong spin-orbit coupling in ordered double perovskites. *Physical Review B*, 82(17):174440, November 2010.

[99] G. Jackeli and G. Khaliullin. Mott Insulators in the Strong Spin-Orbit Coupling Limit: From Heisenberg to a Quantum Compass and Kitaev Models. *Physical Review Letters*, 102(1):017205, January 2009.

[100] Victor Galitski and Ian B. Spielman. Spin–orbit coupling in quantum gases. *Nature*, 494(7435):49–54, February 2013.

[101] Maciej Lewenstein, Anna Sanpera, Veronica Ahufinger, Bogdan Damski, Aditi Sen(De), and Ujjwal Sen. Ultracold atomic gases in optical lattices: mimicking condensed matter physics and beyond. *Adv. Phys.*, 56(2):243, 2007.

[102] R. A. Hart, P. M. Duarte, T. Yang, X. Liu, T. Paiva, E. Khatami, R. T. Scalettar, N. Trivedi, D. A. Huse, and R. G. Hulet. Observation of antiferromagnetic correlations in the Hubbard model with ultracold atoms. *Nature*, 519(7542):211, Feb 2015.

[103] T. A. Corcovilos, S. K. Baur, J. M. Hitchcock, E. J. Mueller, and R. G. Hulet. Detecting antiferromagnetism of atoms in an optical lattice via optical Bragg scattering. *Phys. Rev. A*, 81(1):013415, Jan 2010.

[104] S. Fuchs, E. Gull, L. Pollet, E. Burovski, E. Kozik, T. Pruschke, and M. Troyer. Thermodynamics of the 3D Hubbard model on approaching the Neel transition. *Phys. Rev. Lett.*, 106(3):030401, Jan 2011.

[105] E. Kozik, E. Burovski, V. W. Scarola, and M. Troyer. Néel temperature and thermodynamics of the half-filled three-dimensional Hubbard model by diagrammatic determinant Monte Carlo. *Phys. Rev. B*, 87:205102, May 2013.

[106] F. S. Cataliotti, S. Burger, C. Fort, P. Maddaloni, F. Minardi, A. Trombettoni, A. Smerzi, and M. Inguscio. Josephson junction arrays with Bose-Einstein condensates. *Science*, 293(5531):843–846, 2001.

[107] M. Cristiani, Oliver Morsch, N. Malossi, M. Jona-Lasinio, M. Anderlini, E. Courtade, and E. Arimondo. Instabilities of a Bose-Einstein condensate in a periodic potential: an experimental investigation. *Optics Express*, 12(1):4, 2004.

[108] L. Fallani, L. De Sarlo, J. E. Lye, M. Modugno, R. Saers, C. Fort, and M. Inguscio.

Observation of dynamical instability for a Bose-Einstein condensate in a moving 1D optical lattice. *Phys. Rev. Lett.*, 93(14):140406, Sep 2004.

[109] C. D. Fertig, K. M. O'Hara, J. H. Huckans, S. L. Rolston, W. D. Phillips, and J. V. Porto. Strongly inhibited transport of a degenerate 1d bose gas in a lattice. *Phys. Rev. Lett.*, 94:120403, Apr 2005.

[110] L. De Sarlo, L. Fallani, J. E. Lye, M. Modugno, R. Saers, C. Fort, and M. Inguscio. Unstable regimes for a Bose-Einstein condensate in an optical lattice. *Phys. Rev. A*, 72(1):013603, Jul 2005.

[111] K. Henderson, H. Kelkar, B. Gutiérrez-Medina, T. C. Li, and M. G. Raizen. Experimental study of the role of atomic interactions on quantum transport. *Phys. Rev. Lett.*, 96:150401, Apr 2006.

[112] Jongchul Mun, Patrick Medley, Gretchen K. Campbell, Luis G. Marcassa, David E. Pritchard, and Wolfgang Ketterle. Phase diagram for a Bose-Einstein condensate moving in an optical lattice. *Phys. Rev. Lett.*, 99(15):150604, Oct 2007.

[113] D. McKay, M. White, M. Pasienski, and B. Demarco. Phase-slip-induced dissipation in an atomic Bose-Hubbard system. *Nature*, 453:76, May 2008.

[114] D. C. McKay and B. DeMarco. Cooling in strongly correlated optical lattices: prospects and challenges. *Rep. Prog. Phys.*, 74(5):054401, May 2011.

[115] V. W. Scarola and S. Das Sarma. Edge transport in 2D cold atom optical lattices. *Phys. Rev. Lett.*, 98:210403, 2007.

[116] Chien-Hung Lin, Rajdeep Sensarma, K. Sengupta, and S. Das Sarma. Quantum dynamics of disordered bosons in an optical lattice. *Phys. Rev. B*, 86:214207, Dec 2012.

[117] V. W. Scarola and B. DeMarco. Dynamics of hubbard-band quasiparticles in disordered optical lattices. *Phys. Rev. A*, 92(5):053628, Nov 2015.

[118] Daniel S. Rokhsar and B. G. Kotliar. Gutzwiller projection for bosons. *Phys. Rev. B*, 44:10328–10332, Nov 1991.

[119] Mark Jreissaty, Juan Carrasquilla, F. Alexander Wolf, and Marcos Rigol. Expansion of Bose-Hubbard Mott insulators in optical lattices. *Phys. Rev. A*, 84:043610, Oct 2011.

[120] Pierfrancesco Buonsante, Francesco Massel, Vittorio Penna, and Alessandro Vezzani. Gutzwiller approach to the Bose-Hubbard model with random local impurities. *Phys. Rev. A*, 79(1):013623, JAN 2009.

[121] Michael E. Fisher, Michael N. Barber, and David Jasnow. Helicity modulus, superfluidity, and scaling in isotropic systems. *Phys. Rev. A*, 8:1111, Aug 1973.

[122] Ana Maria Rey, Guido Pupillo, Charles W. Clark, and Carl J. Williams. Ultracold atoms confined in an optical lattice plus parabolic potential: A closed-form approach. *Phys. Rev. A*, 72:033616, Sep 2005.

[123] M. Rigol, V. Rousseau, R. T. Scalettar, and R. R. P. Singh. Collective oscillations of strongly correlated one-dimensional bosons on a lattice. *Phys. Rev. Lett.*, 95(11):110402, Sep 2005.

[124] C. J. Pethick and H. Smith. *Bose-Einstein Condensation in Dilute Gases*. Cambridge University Press, New York, 2008.

[125] V. W. Scarola and S. Das Sarma. Cold-atom optical lattices as quantum analog simulators for aperiodic one-dimensional localization without disorder. *Phys. Rev. A*, 73:041609, Apr 2006.

[126] S. Q. Zhou and D. M. Ceperley. Construction of localized wave functions for a disordered optical lattice and analysis of the resulting Hubbard model parameters. *Phys. Rev. A*, 81:013402, Jan 2010.

[127] P. Verkerk, B. Lounis, C. Salomon, C. Cohen-Tannoudji, J.-Y. Courtois, and G. Grynberg. Dynamics and spatial order of cold cesium atoms in a periodic optical potential. *Phys. Rev. Lett.*, 68(26):3861, 1992.

[128] P. S. Jessen, C. Gerz, P. D. Lett, W. D. Phillips, S. L. Rolston, R. J. C. Spreeuw, and C. I. Westbrook. Observation of quantized motion of Rb atoms in an optical field. *Phys. Rev. Lett.*, 69(1):49, 1992.

[129] A. Hemmerich and T. W. Hansch. Two-dimesional atomic crystal bound by light. *Phys. Rev. Lett.*, 70(4):410, 1993.

[130] T. Stöferle, H. Moritz, C. Schori, M. Köhl, and T. Esslinger. Transition from a strongly interacting 1d superfluid to a Mott insulator. *Phys. Rev. Lett.*, 92:130403, Mar 2004.

[131] R. Jordens, N. Strohmaier, K. Guenther, H. Moritz, and T. Esslinger. A Mott insulator of fermionic atoms in an optical lattice. *Nature*, 455:204, 2008.

[132] U. Schneider, L. Hackermueller, S. Will, Th. Best, I. Bloch, T. A. Costi, R. W. Helmes, D. Rasch, and A. Rosch. Metallic and insulating phases of repulsively interacting fermions in a 3D optical lattice. *Science*, 322:1520, 2008.

[133] B. Gadway, D. Pertot, J. Reeves, M. Vogt, and D. Schneble. Glassy behavior in a binary atomic mixture. *Phys. Rev. Lett.*, 107(14):145306, 2011.

[134] M.C. Beeler, M.E.W. Reed, T. Hong, and S.L. Rolston. Disorder-driven loss of phase coherence in a quasi-2D cold atom system. *New J. Phys.*, 14(7):073024, Jul 2012.

[135] J.-P. Brantut, J. Meineke, D. Stadler, S. Krinner, and T. Esslinger. Conduction of ultracold fermions through a mesoscopic channel. *Science*, 337(6098):1069, Aug 2012.

[136] S. Krinner, D. Stadler, J. Meineke, J.P. Brantut, and T. Esslinger. Superfluidity with disorder in a thin film of quantum gas. *Phys. Rev. Lett.*, 110(10):100601, Mar 2013.

[137] S. S. Kondov, W. R. McGehee, W. Xu, and B. DeMarco. Disorder-induced localization in a strongly correlated atomic Hubbard gas. *Phys. Rev. Lett.*, 114(8):083002, Feb 2015.

[138] M. Schreiber, S. S. Hodgman, P. Bordia, H. P. Luschen, M. H. Fischer, R. Vosk, E. Altman, U. Schneider, and I. Bloch. Observation of many-body localization of interacting fermions in a quasi-random optical lattice. January 2015.

[139] R. T. Scalettar, G. G. Batrouni, and G. T. Zimanyi. Localization in interacting, disordered, bose systems. *Phys. Rev. Lett.*, 66:3144, Jun 1991.

[140] R. Mondaini and M. Rigol. Many-body localization and thermalization in disordered hubbard chains. *Phys. Rev. A*, 92:041601, Oct 2015.

[141] I. Hen and M. Rigol. Superfluid to Mott insulator transition of hardcore bosons in a superlattice. *Phys. Rev. B*, 80:134508, Oct 2009.

[142] I. Hen, M. Iskin, and M. Rigol. Phase diagram of the hard-core Bose-Hubbard model on a checkerboard superlattice. *Phys. Rev. B*, 81:064503, Feb 2010.

[143] K. Sheshadri, H. R. Krishnamurthy, R. Pandit, and T. V. Ramakrishnan. Percolation-enhanced localization in the disordered bosonic Hubbard model. *Phys. Rev. Lett.*, 75:4075, November 1995.

[144] B Damski, J Zakrzewski, L Santos, P Zoller, and M Lewenstein. Atomic Bose and Anderson glasses in optical lattices. *Phys. Rev. Lett.*, 91(8):080403, AUG 22 2003.

[145] P. Buonsante, V. Penna, A. Vezzani, and P. B. Blakie. Mean-field phase diagram of cold lattice bosons in disordered potentials. *Phys. Rev. A*, 76:011602, Jul 2007.

[146] Michiel Snoek and Walter Hofstetter. Two-dimensional dynamics of ultracold atoms in optical lattices. *Phys. Rev. A*, 76:051603, Nov 2007.

[147] F. A. Wolf, I. Hen, and M. Rigol. Collapse and revival oscillations as a probe for the tunneling amplitude in an ultracold Bose gas. *Phys. Rev. A*, 82:043601, Oct 2010.

[148] M. Snoek. Rigorous mean-field dynamics of lattice bosons: Quenches from the Mott insulator. *Europhys. Lett.*, 95(3):30006, 2011.

[149] M. Jreissaty, J. Carrasquilla, F. A. Wolf, and M. Rigol. Expansion of Bose-Hubbard Mott insulators in optical lattices. *Phys. Rev. A*, 84:043610, Oct 2011.

[150] Bela Bauer and Chetan Nayak. Area laws in a many-body localized state and its implications for topological order. *J. Stat. Mech: Theory Exp.*, 2013(09):P09005, Sep 2013.

[151] H. Kim and D. A. Huse. Ballistic spreading of entanglement in a diffusive nonintegrable system. *Phys. Rev. Lett.*, 111:127205, Sep 2013.

[152] Jens H. Bardarson, Frank Pollmann, and Joel E. Moore. Unbounded growth of entanglement in models of many-body localization. *Phys. Rev. Lett.*, 109(1):017202, Jul 2012.

[153] Yinyin Qian. *Quantum transport and phase diagram of ultracold bosonic atoms in optical lattices*. Ph.D., The University of Texas at Dallas, United States – Texas, 2013.

[154] G. Nicolay, F. Reinert, S. Hüfner, and P. Blaha. Spin-orbit splitting of the L-gap surface state on Au(111) and Ag(111). *Physical Review B*, 65(3):033407, December 2001.

[155] G. Bihlmayer, S. Blügel, and E. V. Chulkov. Enhanced rashba spin-orbit splitting in Bi/Ag(111) and Pb/Ag(111) surface alloys from first principles. *Physical Review B*, 75(19):195414, May 2007.

[156] I. Vurgaftman, J. R. Meyer, and L. R. Ram-Mohan. Band parameters for III–V compound semiconductors and their alloys. *Journal of Applied Physics*, 89(11):5815–5875, June 2001.

[157] J. B. Miller, D. M. Zumbühl, C. M. Marcus, Y. B. Lyanda-Geller, D. Goldhaber-Gordon, K. Campman, and A. C. Gossard. Gate-Controlled Spin-Orbit Quantum Interference Effects in Lateral Transport. *Physical Review Letters*, 90(7):076807, February 2003.

[158] M. Oestreich and W. W. Rühle. Temperature Dependence of the Electron Landé g Factor in GaAs. *Physical Review Letters*, 74(12):2315–2318, March 1995.

[159] G. L. Chen, J. Han, T. T. Huang, S. Datta, and D. B. Janes. Observation of the interfacial-field-induced weak antilocalization in InAs quantum structures. *Physical Review B*, 47(7):4084–4087, February 1993.

[160] S. K. Greene, J. Singleton, P. Sobkowicz, T. D. Golding, M. Pepper, J. A. A. J. Perenboom, and J. Dinan. Subband occupancies and zero-field spin splitting in InSb-CdTe heterojunctions: magnetotransport experiments and self-consistent calculations. *Semiconductor Science and Technology*, 7(11):1377, 1992.

[161] Karen Michaeli, Andrew C. Potter, and Patrick A. Lee. Superconducting and ferromagnetic phases in $SrTiO_3/LaAlO_3$ Oxide Interface Structures: Possibility of Finite Momentum Pairing. *Physical Review Letters*, 108(11):117003, March 2012.

[162] J. Radić, A. Di Ciolo, K. Sun, and V. Galitski. Exotic Quantum Spin Models in

Spin-Orbit-Coupled Mott Insulators. *Physical Review Letters*, 109(8):085303, August 2012.

[163] William S. Cole, Shizhong Zhang, Arun Paramekanti, and Nandini Trivedi. Bose-Hubbard Models with Synthetic Spin-Orbit Coupling: Mott Insulators, Spin Textures, and Superfluidity. *Physical Review Letters*, 109(8):085302, August 2012.

[164] Zi Cai, Xiangfa Zhou, and Congjun Wu. Magnetic phases of bosons with synthetic spin-orbit coupling in optical lattices. *Physical Review A*, 85(6):061605, June 2012.

[165] Saptarshi Mandal, Kush Saha, and K. Sengupta. Superfluid-insulator transition of two-species bosons with spin-orbit coupling. *Physical Review B*, 86(15):155101, October 2012.

[166] Ming Gong, Yinyin Qian, Mi Yan, V. W. Scarola, and Chuanwei Zhang. Dzyaloshinskii-Moriya Interaction and Spiral Order in Spin-orbit Coupled Optical Lattices. *Scientific Reports*, 5:10050, May 2015.

[167] Peter Fulde and Richard A. Ferrell. Superconductivity in a Strong Spin-Exchange Field. *Physical Review*, 135(3A):A550–A563, August 1964.

[168] Zi Cai, Yupeng Wang, and Congjun Wu. Stable Fulde-Ferrell-Larkin-Ovchinnikov pairing states in two-dimensional and three-dimensional optical lattices. *Physical Review A*, 83(6):063621, June 2011.

[169] Roberto Casalbuoni and Giuseppe Nardulli. Inhomogeneous superconductivity in condensed matter and QCD. *Reviews of Modern Physics*, 76(1):263–320, February 2004.

[170] Takeshi Mizushima, Masanori Ichioka, and Kazushige Machida. Fulde–Ferrell–Larkin–Ovchinnikov states in a superfluid Fermi gas. *Journal of Physics and Chemistry of Solids*, 66(8):1359–1361, August 2005.

[171] Hui Hu, Xia-Ji Liu, and Peter D. Drummond. Phase Diagram of a Strongly Interacting Polarized Fermi Gas in One Dimension. *Physical Review Letters*, 98(7):070403, February 2007.

[172] T. K. Koponen, T. Paananen, J.-P. Martikainen, M. R. Bakhtiari, and P. Törmä. FFLO state in 1-, 2- and 3-dimensional optical lattices combined with a non-uniform background potential. *New Journal of Physics*, 10(4):045014, 2008.

[173] A. E. Feiguin and F. Heidrich-Meisner. Pairing states of a polarized Fermi gas trapped in a one-dimensional optical lattice. *Physical Review B*, 76(22):220508, December 2007.

[174] T. Paananen. Superfluid density of the ultra-cold Fermi gas in optical lattices. *Journal of Physics B: Atomic, Molecular and Optical Physics*, 42(16):165304, 2009.

[175] Meera M. Parish, Stefan K. Baur, Erich J. Mueller, and David A. Huse. Quasi-One-Dimensional Polarized Fermi Superfluids. *Physical Review Letters*, 99(25):250403, December 2007.

[176] J. Tempere, M. Wouters, and J. T. Devreese. Imbalanced Fermi superfluid in a one-dimensional optical potential. *Physical Review B*, 75(18):184526, May 2007.

[177] Yen Lee Loh and Nandini Trivedi. Detecting the Elusive Larkin-Ovchinnikov Modulated Superfluid Phases for Imbalanced Fermi Gases in Optical Lattices. *Physical Review Letters*, 104(16):165302, April 2010.

[178] Daniel S. Rokhsar and B. G. Kotliar. Gutzwiller projection for bosons. *Physical Review B*, 44(18):10328–10332, November 1991.

[179] A. E. Niederle and H. Rieger. Superfluid clusters, percolation and phase transitions in the disordered, two-dimensional Bose–Hubbard model. *New Journal of Physics*, 15(7):075029, 2013.

[180] Chunji Wang, Chao Gao, Chao-Ming Jian, and Hui Zhai. Spin-Orbit Coupled Spinor Bose-Einstein Condensates. *Physical Review Letters*, 105(16):160403, October 2010.

[181] Tin-Lun Ho and Shizhong Zhang. Bose-Einstein Condensates with Spin-Orbit Interaction. *Physical Review Letters*, 107(15):150403, October 2011.

[182] Yun Li, Lev P. Pitaevskii, and Sandro Stringari. Quantum Tricriticality and Phase Transitions in Spin-Orbit Coupled Bose-Einstein Condensates. *Physical Review Letters*, 108(22):225301, May 2012.

[183] A. V. Samokhvalov, A. S. Mel'nikov, and A. I. Buzdin. Fulde-Ferrell-Larkin-Ovchinnikov states and quantum oscillations in mesoscopic superconductors and superfluid ultracold Fermi gases. *Physical Review B*, 82(17):174514, November 2010.

[184] Jeroen P. A. Devreese, Michiel Wouters, and Jacques Tempere. Controlling the pair momentum of the Fulde-Ferrell-Larkin-Ovchinnikov state in a three-dimensional Fermi gas through a one-dimensional periodic potential. *Physical Review A*, 84(4):043623, October 2011.

[185] V. W. Scarola, L. Pollet, J. Oitmaa, and M. Troyer. Discerning Incompressible and Compressible Phases of Cold Atoms in Optical Lattices. *Physical Review Letters*, 102(13):135302, March 2009.